Research
A SCIENCE PARTNER JOURNAL

REVIEW ARTICLE

Recent Advances in Cation-Engineered A_3BX_6 Metal Halide Perovskite for Enhanced Radiative Transition

Xin Zhou[1†], Hang Yin[1,2,3*†], Qinhua Wei[1], Da Chen[1], Dongfeng Xue[4], Tönu Pullerits[2], Junsheng Chen[3*], and Laishun Qin[1*]

[1]College of Materials and Chemistry, China Jiliang University, Hangzhou 310018, China. [2]Chemical Physics and NanoLund, Lund University, Lund 22100, Sweden. [3]Nano-Science Center and Department of Chemistry, University of Copenhagen, Copenhagen 2100, Denmark. [4]Shenzhen Institute for Advanced Study, University of Electronic Science and Technology of China, Shenzhen 518110, China.

*Address correspondence to: yinhang@cjlu.edu.cn (H.Y.); junsheng.chen@chem.ku.dk (J.C.); qinlaishun@cjlu.edu.cn (L.Q.)
†These authors contributed equally to this work.

Citation: Zhou X, Yin H, Wei Q, Chen D, Xue D, Pullerits T, Chen J, Qin L. Recent Advances in Cation-Engineered A_3BX_6 Metal Halide Perovskite for Enhanced Radiative Transition. *Research* 2026;9:Article 1281. https://doi.org/10.34133/research.1281

Submitted 20 January 2026
Revised 14 April 2026
Accepted 14 April 2026
Published 18 May 2026

Copyright © 2026 Xin Zhou et al. Exclusive licensee Science and Technology Review Publishing House. No claim to original U.S. Government Works. Distributed under a Creative Commons Attribution License (CC BY 4.0).

A_3BX_6 perovskites, a family of vacancy-ordered structures, exhibit diverse luminescence behaviors upon photon, electron, and high-energy excitation, primarily originating from intrinsic self-trapped excitons or dopant-induced electronic transitions. Upon B-site cation engineering, ns^2 cations tune intrinsic luminescence, whereas transition-metal and rare-earth dopants activate characteristic d–d, d–f, and f–f transitions, enriching A_3BX_6 optical diversity. The tunable crystal structure and electronic configuration endow A_3BX_6 perovskites with exceptional versatility for photoluminescence, electroluminescence, and scintillation applications. This review systematically elucidates how B-site chemistry modulates the structure–property–application relationships in this material family. P-block B-site A_3BX_6 perovskites exhibit high photoluminescence efficiency, broadband emission, and strong ultraviolet absorption, enabling applications in high-sensitivity photodetectors (1.23×10^{12} Jones), information encryption, and white light-emitting diodes. In comparison, rare-earth-based A_3BX_6 perovskites enable high-efficiency electroluminescent devices, featuring deep-blue light-emitting diode with an external quantum efficiency of 7.9%. Moreover, they exhibit superior scintillation performance, including high x-ray light yield (88,800 ph/MeV), low x-ray detection limit (63 nGy/s), and notable γ-ray response under ^{137}Cs excitation (47,000 ph/MeV; 4.0% energy resolution). These insights highlight the pivotal role of B-site cation engineering in tailoring luminescence mechanisms and enabling multifunctional A_3BX_6 perovskites for photonic and radiation applications.

Introduction

Radiative transitions, as the core mechanism of energy release in quantum theory, not only elucidate light–matter interactions but also enable breakthroughs in optoelectronic conversion, high-energy scintillation imaging, and quantum light sources, bridging photophysical mechanisms and practical applications [1]. Both scintillation and luminescence possess cross-domain similarities in photophysical mechanisms, particularly in excitation modalities, radiative decay pathways, fluorescent spectral range (ultraviolet [UV] or visible), energy conversion and migration process, and charge carrier dynamics [2,3]. More recently, metal halide perovskites (MHPs) have emerged as potential luminescent scintillators, leveraging their superior photoelectric properties for applications spanning photoluminescence (PL), electroluminescence (EL), and radioluminescence (RL) [4–7]. For example, the applied research for $CsPbX_3$ centered on the properties of PL and EL prior to 2015, while a breakthrough emerged in 2018 with its RL application in x-ray and γ-ray detection as efficient scintillators [8,9]. Following these breakthroughs, it has been increasingly recognized that high-energy scintillation performance is highly sensitive to compositional tunability, where cation substitution directly influences crystal structure, electronic configuration, and defect landscape, thereby modulating light yield (L.Y.), energy resolution (E.R.), and time response [10]. Thus, the spotlight has gradually connected application demonstrations with cation-engineered strategies, which is crucial for tailoring the electronic structure, regulating radiative transitions, and ultimately improving the scintillation performance of MHPs.

To mitigate the toxicity of Pb^{2+}, as well as the radiation sensitivity and poor stability of $CsPbX_3$ [11], lead-free A_3BX_6 MHPs (strictly speaking, A_3BX_6 compounds are perovskite-derived structures [12]; however, they are discussed here within the framework of MHPs) are priorities for potential applications (Fig. S1) in anticounterfeiting, light-emitting diodes (LEDs) [13,14], photodetectors [15], and x-ray or γ-ray detection [16,17], due to their tunable electronic structure [16,18], highly tolerant

crystallographic lattices [19,20], low phonon energies [21,22], and functional luminescence [19,23]. Recent advancements in A_3BX_6 systems have expanded the elemental scope across the periodic table, encompassing A-site cations (in blue), B-site cations (in green), halide anions (in yellow), and dopant ions (in espresso), as systematically summarized in Fig. 1. Importantly, the selection of B-site cations governs the electronic and structural characteristics, serving as a pivotal determinant for tuning luminescent behavior and functional performance through strategic doping engineering. According to the periodic table (Fig. 1), chemically accessible B-site cations in A_3BX_6 systems are classified; the B-site host engineering can be grouped into 3 categories: P-block elements, rare-earth (RE) elements with empty f orbitals (RE^{3+}: Sc^{3+}, Y^{3+}, and La^{3+}. It should be noted that La^{3+} has empty 4f orbitals, whereas Sc^{3+} and Y^{3+} lack f orbitals. For consistency, both cases are collectively classified as "empty-f" systems in this work.), and trivalent lanthanides (Ln^{3+}, which are divided into light REs and heavy REs) with f orbitals. Accordingly, this review highlights the B-site cation-centered categorization of A_3BX_6 MHPs and explores their functional applications.

The Luminescence Mechanism of Host and Dopant Engineering

Intrinsic luminescence

Substituting Pb^{2+} with lead-free cations to form A_3BX_6 reduces the Goldschmidt tolerance factor, driving a structural transition from a 3-dimensional ABX_3 to a zero-dimensional (0D) A_3BX_6. This dimensional change results in distinct electronic structures and offers opportunities for tuning structure–property relationships, particularly via symmetry control and orbital interactions. The crystal structure of A_3BX_6 with the $C2/c$ space group features alternating octahedra with 2 distinct tilt angles, due to the different 2 independent site occupations of A cation [24]. The low charge symmetry in 0D A_3BX_6 MHPs favors the charge localization in both the ground and excited states, further affecting the formation of self-trapped excitons (STEs) and second-order Jahn–Teller distortion [25]. In general, this distortion in A_3BX_6 is derived from lone-pair electrons of ns^2 cations, where the antibonding orbitals formed between B-site cation and X-site anion can hybridize with the unoccupied p orbitals of the cations.

Unlike $CsPbX_3$ perovskites, where intrinsic luminescence primarily arises from band-edge exciton recombination (Fig. 2A) [26], A_3BX_6 MHPs crucially exhibit intrinsic STE emission leading to large Stokes shifts and broad emission spectra [27]. According to the self-trapping criterion, which is expressed as Eq. (1) [25]:

$$E_{st} = \frac{W}{2} \tag{1}$$

where W represents the bandgap width and E_{st} is the self-trapping energy, which can be calculated using Eq. (2) [25]:

$$E_{st} = E_{free} - E_{trap} \tag{2}$$

where E_{free} represents the free exciton energy and E_{trap} represents the STE state energy. Compared with 3D ABX_3, the 0D A_3BX_6 structure exhibits more pronounced local lattice distortion and stronger lattice relaxation, which lowers the energy of the E_{trap}. As a result, E_{st} increases and more readily satisfies Eq. (1), thereby facilitating the formation of STEs. In addition, the emission energy can also be described by Eq. (3) [28]:

$$E_{PL} = W - E_b - E_{st} - E_d \tag{3}$$

where E_b represents the exciton binding energy and E_d represents the lattice distortion energy. Compared with $APbX_3$, A_3BX_6 exhibits larger E_{st} and E_d, which results in $E_{PL} < E_g$. Consequently, this leads to a larger Stokes shift and effectively suppresses self-absorption.

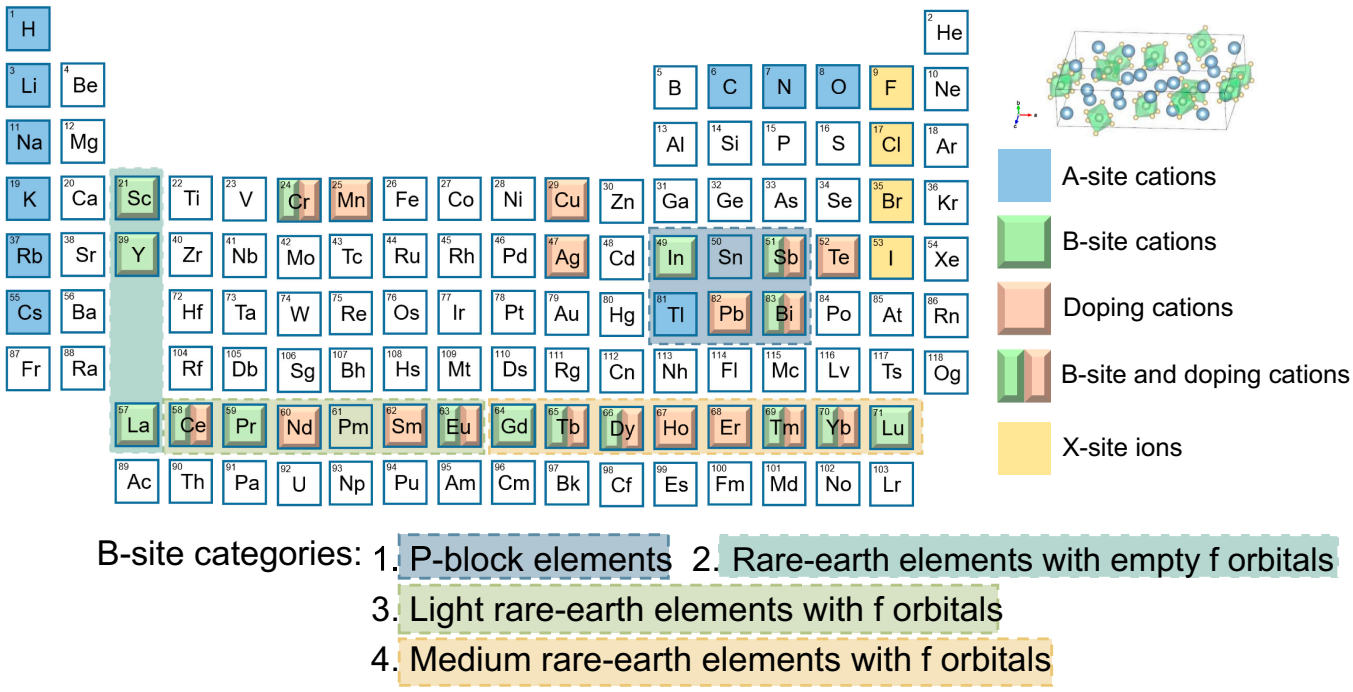


Fig. 1. A-site cations, B-site cations, and X-site halogen anions of A_3BX_6 metal halide perovskites (MHPs) are illustrated in the periodic table. (C, H, O, and N form organic groups occupying the A-site). The blue–gray dashed box denotes P-block elements; the teal–gray dashed box represents rare-earth elements with empty f orbitals; the light-olive dashed box indicates light rare-earth elements with f orbitals; and the sand-yellow dashed box corresponds to heavy rare-earth elements with f orbitals.

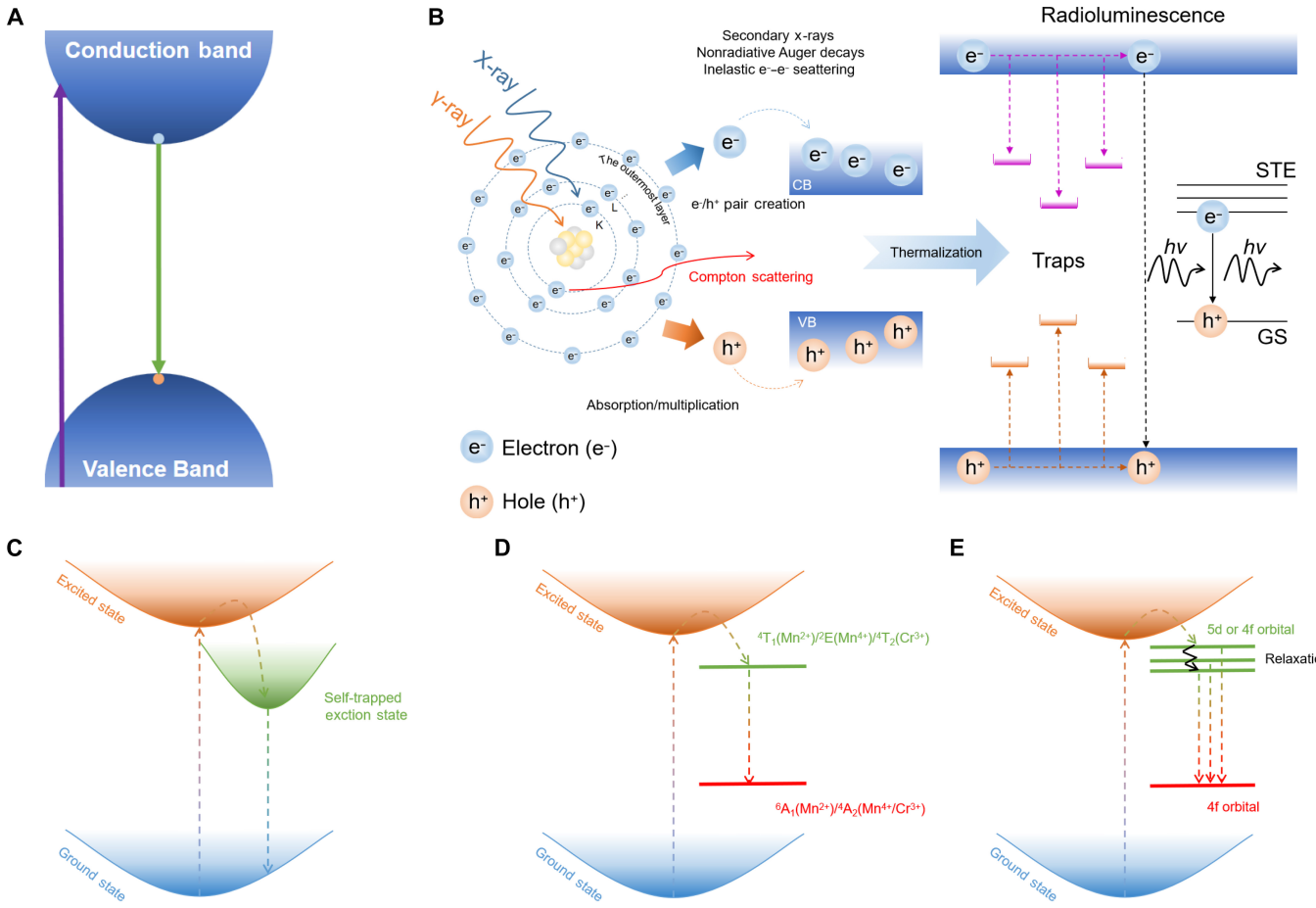


Fig. 2. (A) The band-edge luminescence mechanism diagram of $CsPbBr_3$. (B) The luminescence process triggered by different excitation sources. GS, ground state. (C) The luminescence mechanism of self-trapped exciton (STE) (including intrinsic STE and STE caused by doping). (D) The luminescence mechanism of transition-metal-doped luminescent ions (Mn^{2+}, Mn^{4+}, and Cr^{3+}). (E) The d–f/f–f transition mechanism of rare earth.

Under high-energy excitation such as x-rays and γ-rays, energy deposition occurs through multiple processes (Fig. 2B) including the photoelectric effect, Compton scattering, and subsequent electron–hole pair generation [29]. Different types of high-energy radiation interact with materials through distinct mechanisms, resulting in different energy deposition characteristics. X-rays in the kiloelectronvolt range primarily deposit energy via the photoelectric effect, whereas higher-energy γ-rays mainly undergo Compton scattering, often accompanied by photoelectric absorption or pair production, leading to more spatially distributed energy deposition and differences in carrier dynamics and scintillation behavior. High-energy radiation generates ions and core-excited electrons, giving rise to a cascade of secondary electrons. It is particularly noteworthy that the lower-energy segment of these secondary electrons is most efficient at producing the low-lying excited states responsible for luminescence [30]. As a result, the scintillation superiority of A_3BX_6 MHPs is characterized by low self-absorption, high photon output efficiency, and broad spectral response compatible with photomultiplier tube or silicon photomultiplier [31,32]. However, the isolated octahedra in 0D A_3BX_6 MHPs are susceptible to point defects or heterogeneous interactions, causing energy disorder that suppresses emission [33,34]. Hence, the STE emission could be improved by dopant-related luminescence.

Dopant-related luminescence

To enhance the photoelectric properties of A_3BX_6 MHPs, B-site dopant engineering has emerged as an effective strategy for band structure modulation, which can be divided into 4 categories (Fig. 2C to E):

1. ns^2 cations as B-site dopant. Incorporation of ns^2 cations into the A_3BX_6 host induces the modified lattice distortion, via size mismatch (ionic radius disparities causing local strain), lone-pair effects (asymmetric coordination distorting $[BX_6]^{3-}$ octahedron), and charge redistribution (polarizable ns^2 electrons altering electron density and bond lengths), thereby promoting STE formation and efficient broadband emission [35]. Most ns^2 cations used as dopant in A_3BX_6 are summarized in Fig. 1, highlighting P-block elements (e.g., In, Sb, and Bi) into yellow dashed borders and Ln with empty f orbitals (e.g., Sc, Y, and La) into green dashed borders.
2. Transition-metal cations as B-site dopant. Incorporated transition-metal cations in A_3BX_6 can be summarized in dual luminescence regimes: One is as B-site luminescent center ions (e.g., atomic-like ionic d–d transitions) with sharp emission lines, and the other is STE emission (Fig. 2C). Herein, Mn^{2+} ($3d^5$), Mn^{4+} ($3d^3$), and Cr^{3+} ($3d^3$) exhibit distinct d–d transitions governed by their

crystal-field environments [36–38]. The Mn^{2+} typically dominates an orange–red broadband emission (550 to 650 nm) originating from $^4T_1 \rightarrow {}^6A_1$ transition (Fig. 2D), which is enhanced by electron–phonon coupling in weak octahedral fields. In contrast, Mn^{4+} ($^2E \rightarrow {}^4A_2$) and Cr^{3+} ($^4T_2 \rightarrow {}^4A_2$) emit narrow deep-red (630 to 650 nm) and tunable red to near-infrared (NIR) luminescence (650 to 800 nm), respectively, owing to spin-orbit or vibronic coupling within rigid and intermediate octahedral sites [39–41]. In addition, the incorporation of Ag^+, Cu^+, and Pt^{4+} can enhance the lattice distortion to facilitate the formation of STEs, further improving the efficiencies of PL and RL [42–45].

3. Ln^{3+} with f orbitals as B-site dopant. The incorporation of Ln^{3+} into the A_3BX_6 lattice (A_3BX_6:Ln^{3+}) is facilitated by their ionic charge compatibility with the host B-site cation, enabling isovalent substitution without introducing extrinsic charge defects [46]. In addition, the superiority of A_3BX_6:Ln^{3+} arises from the unique shielding effect of the $5s^25p^6$ subshell in Ln^{3+}, which confines f–f or d–f transitions within the large bandgap of the host matrix, thereby enabling tunable luminescence pathways via energy-level modulation [47]. This strategy not only preserves the intrinsic electrostatic balance in A_3BX_6 but also modulates the luminescence dynamics based on the localized 4f electrons of Ln^{3+}. As illustrated in Fig. 2E, such intrabandgap engineering with different Ln^{3+} as B-site luminescent center enables characteristic f–f transitions (e.g., Tb^{3+}) [48] or d–f charge–transfer transitions (e.g., Ce^{3+}) [49]. The energy transfer (ET) efficiency between these pathways can be optimized by controlling the Ln^{3+} doping concentration and local coordination environment. Specifically, ET or defect-state coupling activates dual-mode emission in A_3BX_6:Ln^{3+}, coexisting with broadband STE emission [50]. By tailoring the B-site dopant composition and concentration, the dual-mode emission can be further tuned to match the spectral sensitivity of photodetectors (e.g., photomultiplier tube or silicon photomultiplier), further improving the scintillation performance, such as L.Y., E.R., and time response. The distinct combination of tunable luminescence, structural stability, and radiation responsiveness positions A_3BX_6 MHPs as highly versatile materials for optoelectronic and scintillation applications. Recent work focusing on B-site scalable synthesis, dopant–host matching, and interface engineering will be essential for advancing their practical implementations.

4. ET processes induced by single or codoping. Upon incorporation of luminescent ions into the A_3BX_6 lattice, their emission can arise not only from direct excitation of dopant-specific energy levels but also from ET from intrinsic emissive states of the host lattice. Such ET processes can be broadly classified into 3 categories: STE to Ln^{3+}, STE to transition metal, and Ln^{3+}–Ln^{3+}. In vacancy-ordered A_3BX_6 MHPs featuring isolated $[BX_6]^{3-}$ octahedra, ET between intrinsic emission and dopant activators can be consistently rationalized within a Förster–Dexter framework [51,52]. The key criterion for distinguishing Förster resonance ET (FRET) from Dexter ET lies in their characteristic transfer distances. FRET originates from long-range Coulombic dipole–dipole interactions and can operate over distances of approximately 1 to 10 nm without requiring wavefunction overlap, whereas Dexter ET is a short-range electron exchange process that relies on direct orbital overlap and therefore becomes effective only at subnanometer distances (<1 nm) [53]. In A_3BX_6 systems, the isolated arrangement of $[BX_6]^{3-}$ octahedra leads to increased effective donor–acceptor separations compared to more strongly connected structures. As a result, STE–Ln^{3+} and Ln^{3+}–Ln^{3+} ET are predominantly governed by FRET, which is predominantly mediated by dipole–quadrupole and quadrupole–quadrupole interactions, while dipole–dipole coupling is typically much weaker. In contrast, STE–transition metal ET is more likely dominated by Dexter exchange interactions because transition-metal d–d excited states are spin- and parity-forbidden, efficient sensitization typically requires short-range exchange coupling at subnanometer distances, as evidenced in 0D isolated octahedra halides, where ET occurs exclusively via Dexter interactions between adjacent donor–acceptor pairs [54]. Thus, the isolated $[BX_6]^{3-}$ octahedral geometry in A_3BX_6 directly governs the effective donor–acceptor separation and, consequently, the energy transfer efficiency.

In addition to the forward energy transfer pathways, thermal back-transfer represents a ubiquitous quenching channel in A_3BX_6 systems [55]. When the excited-state energy levels of dopant activators are energetically close to those of the intrinsic emissive states (e.g., STEs or defect-related states), reverse ET from the dopant back to the host lattice can be thermally activated [56]. This process is typically governed by an Arrhenius-type behavior and becomes increasingly significant at elevated temperatures or under sustained excitation, leading to reduced emission intensity, shortened lifetimes, and compromised operational stability [56]. Owing to the strong localization of excitons and the discrete energy landscape imposed by isolated $[BX_6]^{3-}$ octahedra, A_3BX_6 materials are particularly susceptible to such thermally assisted back-transfer processes, which may coexist with nonradiative relaxation and defect trapping to collectively limit luminescence efficiency [57]. Consequently, suppressing thermal back-transfer through energy-level engineering and structural optimization is crucial for achieving high-efficiency and stable emission in A_3BX_6-based optoelectronic and scintillation applications.

Concentration quenching effect

In doped A_3BX_6 systems, the emission intensity typically increases with dopant concentration at low levels and decreases rapidly after reaching the critical quenching concentration (q_c). Compared with 3D ABX_3 and double-perovskite $A_2B(I)B(III)X_6$ systems, A_3BX_6 generally exhibits a higher q_c, typically around ~5 to 15 mol% for Ln^{3+} or transition-metal dopants, indicating a stronger tolerance toward heavy doping [32,58,59], which is higher than ABX_3 and $A_2B(I)B(III)X_6$ [60,61]. Time-resolved PL measurements further elucidate the underlying dynamics. When the dopant concentration is below q_c, the emission lifetime remains nearly unchanged, indicating that radiative recombination dominates the emission process. In contrast, once the dopant concentration exceeds q_c, the average lifetime decreases markedly, suggesting the emergence of dopant-related nonradiative energy-loss pathways [62]. The concentration-quenching behavior in A_3BX_6 can be analyzed in terms of possible quenching mechanisms. Exchange interactions are generally negligible because of the relatively large separation between dopant ions,

while the limited spectral overlap between emission and absorption bands excludes reabsorption as the dominant mechanism. Therefore, multipolar-interaction-assisted energy migration is considered the primary origin of quenching [63].

This process can be well described by the Yokota–Tanimoto model, which assumes that excitation energy migrates among luminescent centers and is eventually trapped by nonradiative quenching sites, leading to the reduction of emission intensity and lifetime [64]. The isolated $[BX_6]^{3-}$ octahedra in the vacancy-ordered A_3BX_6 framework further suppress long-range energy migration, accounting for the relatively delayed concentration quenching observed in this system [65]. In contrast, the continuously connected octahedral networks in ABX_3 and $A_2B(I)B(III)X_6$ are more favorable for rapid energy migration, making concentration quenching more likely to occur at much lower dopant concentrations [65,66]. It is precisely this synergistic effect of structural isolation and strong exciton localization that enables A_3BX_6 to maintain relatively high radiative efficiency at elevated dopant levels and to exhibit markedly delayed concentration quenching behavior.

The Potential Application of A_3BX_6 MHPs

Stability and application potential

To evaluate the practical potential of A_3BX_6 materials, their stability under various environments, including moisture, high temperature, and high-energy irradiation, has been systematically examined. Under humid conditions, some A_3BX_6 compounds undergo structural phase transitions; however, unlike the typically irreversible transformations observed in ABX_3 perovskites, these transitions are often reversible and can be restored by treatment with polar solvents. The associated changes in PL enable potential applications in moisture sensing, anti-counterfeiting, and information encryption.

Owing to their relatively rigid lattices, A_3BX_6 compounds generally exhibit excellent resistance to thermal quenching. For instance, $Rb_3InCl_6:Sb^{3+}$ maintains stable emission up to 500 K [67], while $Cs_3GdCl_6:Sb^{3+}$ retains 82.4% of its room temperature (RT) emission intensity at 150 °C [22]. This behavior originates from the 0D isolated $[BX_6]^{3-}$ octahedral framework, in which thermal expansion is mainly accommodated by interoctahedral spaces and the relatively soft A-site sublattice, thereby preserving the local coordination environment of the emissive centers. Moreover, relatively high phonon energies and thermal activation barriers (e.g., 33.0-meV phonon energy and 51.3-meV activation energy for Cs_3GdCl_6 [22]) further suppress nonradiative relaxation processes.

In addition, the isolated octahedral framework effectively limits the diffusion of irradiation-induced defects, while the rigid lattice and localized excitonic emission enhance defect tolerance. As a result, A_3BX_6 materials display remarkable radiation stability. For example, $Rb_3InCl_6:Sb^{3+}$ shows nearly unchanged RL intensity up to a cumulative dose of 561.6 Gy [68], whereas $Cs_2NaLuCl_6/Cs_3LuCl_6:Sb^{3+}$ maintains stable RL output even at doses as high as 1,000 Gy [69], highlighting their robustness in high-energy radiation environments.

Applications of photoexcitation and electrical excitation

Building upon the abovementioned optical and electronic advantages, such as reversible phase transitions, tunable luminescence, and B-site elemental diversity, A_3BX_6 MHPs exhibit great potential in a range of PL and EL applications. In addition, the structural isolation of A_3BX_6 enhances exciton binding energy, effectively suppressing exciton dissociation and free carrier generation at RT [70]. Moreover, the flat conduction band (CB) and valence band (VB) for A_3BX_6 MHPs lead to large carrier effective mass, further promoting exciton self-trapping and broadband luminescence efficiency [71–73]. These features render A_3BX_6 MHPs particularly suitable for use as phosphors and active layer in thin-film LED devices.

Under UV excitation, the photogenerated carriers formed in A_3BX_6 MHPs can be driven by an external electric field to convert optical signals into electrical signals, enabling their application in photodetectors. For photodetectors, detectivity is a key performance parameter (Table 1), which is expressed as Eq. (4) [15]:

$$D = \frac{R}{\sqrt{2qI_{\text{dark}}}} \tag{4}$$

where D represents the detectivity, R represents the responsivity, q represents the elementary charge, and I_{dark} represents the dark current per unit area. Currently, the highest sensitivity of detectors based on A_3BX_6 MHPs has reached 1.48×10^{13} Jones [15].

Furthermore, the photogenerated carriers yield an emission wavelength spanning from 300 to 1,000 nm without the application of an external electric field. PL quantum yield (PLQY) is a key parameter for evaluating emissive efficiency, as shown in Eq. (5):

Table 1. The key performance metrics of A_3BX_6 MHPs for photodetectors

Compound	Detectivity (Jones)	Responsivity	Dynamic range (dB)	Rise time	Fall time	Ref.
Cs_3BiBr_6	0.8×10^9	25 mA/W	–	0 ms	60 ms	[123]
Cs_3BiBr_6/Cs_3BiBr_9	8.5×10^{10} (360 nm)	5.6 mA/W (360 nm)	>36.9 (360 nm)	1.4 μs	2.0 μs	[127]
	1.0×10^9 (450 nm)	0.6 mA/W (450 nm)	>34.2 (450 nm)			
Cs_3BiCl_6/GaN	1.23×10^{12}	0.26 A/W	123	28 μs	190 μs	[128]
Cs_3CeBr_6	1.48×10^{13}	2.05 A/W	99.64	93 ms	345 ms	[15]
$Cs_3CeCl_6:Gd^{3+}$	7.938×10^{11}	0.195 A/W	–	0.30 s	0.35 s	[155]

MHPs, metal halide perovskites; Ref., reference.

$$\mathrm{PLQY} = \frac{N_{em}}{N_{abs}} \quad (5)$$

where N_{em} and N_{abs} represent the number of emitted and absorbed photons, respectively. Although visible-emissive A_3BX_6 MHPs can achieve PLQY approaching 100% [74] and even reach 93.2% in nanocrystals (NCs) [50]. The PLQY of NIR-emissive A_3BX_6 can reach 87.4%.

Relatively, the reversible hydration/dehydration between A_3BX_6 and $A_2BX_5{\cdot}H_2O$ has been actively explored for application in NIR emission, information storage, and anticounterfeiting. Moreover, the phase transitions in A_3BX_6 compounds often involve changes in crystal symmetry and optical properties, enabling tunable emission color or intensity. Notably, the NIR-emissive PLQY of A_3BX_6 MHPs after phase transitions has been reported to exceed 75% [75].

In contrast, EL differs in that it generates photons through the injection and recombination of electric-field-driven electron–hole pairs. In EL devices, external quantum efficiency (EQE) is a critical parameter (Table 2), given by Eq. (6) [76]:

$$\mathrm{EQE} = \eta_{out} \cdot \eta_r \cdot \gamma \cdot \mathrm{PLQY} \quad (6)$$

where η_{out} is the light outcoupling efficiency, the η_r is radiative recombination efficiency, and γ is exciton formation efficiency. As the active layers in thin-film LEDs, A_3BX_6 MHPs have demonstrated that a maximum EQE can reach 7.9%, which is the highest efficiency among metal halide deep-blue LEDs so far [13,14].

Application of x-ray excitation

In scintillators, the majority of light emission originates from electronic transitions induced by energetic electron impact, which, in some respects, resembles the electrical excitation processes in LEDs [30]. Consequently, high-performance x-ray detector materials must simultaneously possess a high effective atomic number (Z_{eff}) and mass attenuation coefficient (μ/ρ) to ensure efficient x-ray absorption within limited thicknesses [77]. The total μ/ρ can be described by Eq. (7) [78]:

$$\mu/\rho = \tau/\rho + \sigma/\rho + \kappa/\rho + \sigma_R/\rho \quad (7)$$

where τ/ρ is the contribution of the photoelectric effect, σ/ρ is that of the Compton effect, κ/ρ is that of pair production, and σ_R/ρ is that of Rayleigh scattering.

In the photoelectric effect regime (<100 keV), the mass attenuation coefficient approximately scales as Eq. (8) [79]:

$$\mu/\rho \propto \frac{Z_{eff}^n}{E^3} \quad (8)$$

where n ranges from 3 to 4, indicating a strong dependence on atomic composition and photon energy. A_3BX_6 MHPs inherently possess the high Z_{eff} and μ/ρ due to the presence of heavy elements at both A- and X-sites, as well as their tunable composition through B-site doping.

In addition, 3 key performance metrics for x-ray detectors include L.Y., limit of detection (LoD), and spatial resolution (f) (Table 3). The L.Y. is defined as Eq. (9) [80]:

$$\mathrm{L.Y.} = \frac{\eta \cdot E_{dep}}{W} \quad (9)$$

where η is the energy conversion efficiency, E_{dep} is the energy deposited by x-rays, and W is the average energy required to generate one photon. Recently, the reported A_3BX_6 have demonstrated a value of L.Y. as high as 88,800 ph/MeV under 50-keV x-ray excitation [31], significantly outperforming conventional scintillators, such as NaI:Tl (~41,000 ph/MeV) and CsI:Tl (~60,000 ph/MeV) [81].

A high L.Y. enhances signal output under low x-ray dose, improving the signal-to-noise ratio (SNR) and contributing to superior detection sensitivity. For estimating the practical sensitivity, LoD is defined as Eq. (10) [82]:

$$\mathrm{LoD} = \frac{3 \times \sigma_{bg}}{S} \quad (10)$$

where σ_{bg} is the standard deviation of background noise and S is the slope of the signal response to x-ray dose. As is known,

Table 2. The key performance parameters of A_3BX_6 MHPs for LEDs, including EL peak, Commission Internationale de l'Éclairage (CIE) coordinates, EQE, maximum luminance (L_{max}), and half-lifetime (T_{50})

Device structure	EL peak (nm)	CIE coordinates	EQE (%)	L_{max} (cd/m^2)	T_{50}	Ref.
Al/TPBi/EHC-Cs_3LaCl_6/PEDO/ITO	442	(0.210, 0.171)	0.53	127	–	[150]
ITO/ZnO/$Cs_3La_{0.17}Nd_{0.83}Br_6$/TCTA/$MoO_3$/Al	1,070, 1,350	–	3.49	–	488 min	[144]
ITO/PEDOT/PSS/PVK/Cs_3CeBr_6/SPPO13/LiF/Al	392, 430	(0.158, 0.02)	0.44	–	–	[185]
ITO/ZnO/Al_2O_3/Cs_3CeBr_6/TCTA/TAPC/HAT-CN/Al	391, 421	–	0.46	–	–	[73]
ITO/ZnO:PEI/Al_2O_3/Cs_3CeI_6/MCP/TAPC/ TAPC:HAT-CN/HAT-CN/Al	430, 470	(0.15, 0.04)	3.5	470	45 min	[13]
ITO/ZnO/Al_2O_3/Rb_3CeI_6/MCP/TAPC/HAT-CN/Al	427, 468	(0.15, 0.06)	0.67	98	–	[186]
ITO/ZnO:PEI/Al_2O_3/Cs_3CeI_6/MCP/TAPC/ TAPC:HAT-CN/HAT-CN/Al	435, 480	(0.145, 0.057)	7.9	1,075	72 min	[14]
Al/TPBi/EHC-Cs_3EuCl_6/PEDO/ITO	616	(0.648, 0.338)	5.17	370	440 h	[150]
Al/TPBi/EHC-Cs_3TbCl_6/PEDO/ITO	545	(0.267, 0.418)	1.58	2,373	–	[150]
ITO/ZnO/LiF/Cs_3DyI_6:Er^{3+}/TPPO/TCTA/MoO_3/Ag	1,540	(0.25, 0.35)	2.76	–	345 min	[187]

MHPs, metal halide perovskites; LED, light-emitting diode; EQE, external quantum efficiency; EL, electroluminescence.

Table 3. The key performance metrics of A_3BX_6 MHPs for x-ray imaging

Compound	Sample	RL peak (nm)	Tube voltage (kV)	L.Y. (ph/MeV)	LoD (μGy/s)	Film thickness (μm)	*f* (lp/mm)	MTF	Ref.
$Rb_3InCl_6:Sb^{3+}$	NC	510	30	15,500	5.20×10^3	200	18.5	0.2	[68]
$Cs_3YCl_6:Sb^{3+}$	Powder	550	70	16,000	1.12	500	9	–	[72]
Cs_3CeCl_6	Film	375, 410	35	7,533	18.3	7.4	10.2	0.2	[157]
Cs_3CeBr_6	Film	390, 425	35	28,510	1.1	7.1	26.4	0.2	[157]
Cs_3EuCl_6	Powder	592, 614	50	12,877	643.1×10^{-3}	300	9.17	0.2	[158]
Rb_3TbCl_6	Polycrystal	548	80	88,800	115.38×10^{-3}	260	3.9	0.2	[31]
Cs_3TbCl_6	Polycrystal	548	80	56,800	149.65×10^{-3}	260	3.3	0.2	[31]
$Cs_3TbCl_6:Sb^{3+}$	NC	548	50	20,300	212×10^{-3}	–	9.6	0.2	[16]
Cs_3TbCl_6	Powder	547	70	51,800	63×10^{-3}	1,000	12	–	[83]
$Bzmim_3TbCl_6$	Glass	547	40	4,101	308.30×10^{-3}	1,000	25	–	[172]
$Bzmim_3EuCl_6$	Glass	592, 611	40	1,419	1.56	1,000	–	–	[172]
$BuTPP_3TbCl_6$	Glass	547	50	8,100	0.93	–	26.8	0.2	[173]
Cs_3LuCl_6/ $Cs_2NaLuCl_6:Sb^{3+}$	NC	–	50	–	140×10^{-3}	200	14	0.2	[69]
$Cs_3LuCl_6:Sb^{3+}$	NC	531	50	7,300	0.4	110	11.5	0.2	[167]
$Cs_3LuCl_6:Ce^{3+}$	Powder	380, 420		8,120	57.9×10^{-3}	100	8.38	0.2	[188]
$Cs_3LuCl_6:Tb^{3+}$	Powder	548	50	21,000	–	200	11 (423 K)	0.2	[189]
$Cs_3LuCl_6:Ce^{3+}, Sm^{3+}$	Powder	604	50	7,600	–	200	8 (423 K)	0.2	[189]

MHPs, metal halide perovskites; NC, nanocrystal; RL, radioluminescence; MTF, modulation transfer function; L.Y., light yield.

LoD as low as 63 nGy/s has been reported, highlighting the excellent detection sensitivity of A_3BX_6 scintillators [83].

In general, a combination of high L.Y. and low LoD is highly desirable for low-dose x-ray imaging applications. As for spatial resolution, it is commonly evaluated using the modulation transfer function (MTF), defined as Eq. (11) [84]:

$$\mathrm{MTF}(f) = \frac{M_{\mathrm{output}}(f)}{M_{\mathrm{input}}(f)} \tag{11}$$

where $M_{\mathrm{output}}(f)$ and $M_{\mathrm{input}}(f)$ represent the contrast of the output and input signals, respectively, at a given spatial frequency. All inorganic A_3BX_6 MHPs have demonstrated the spatial frequency of 26.4 lp/mm at an MTF of 0.2. This recorded *f* value of A_3BX_6 MHP demonstrates greater potential than that of current commercial scintillators [68].

The application of γ-ray excitation

Beyond x-ray applications, A_3BX_6 MHPs also demonstrate considerable potential in γ-ray detection. The total μ/ρ for γ-ray photons is described by the same physical formalism as that for x-ray photons. Relative to x-rays with photoelectric effect, Compton scattering and pair production become increasingly dominant at γ-ray energies (>100 keV). Therefore, as candidates of γ-ray scintillators, the modified A_3BX_6 MHPs require not only high ρ and Z_{eff} but also high L.Y., fast response, and superior E.R. (Table 4).

The E.R. is a critical parameter for evaluating a scintillator's ability to discriminate between γ-ray energies, and its value is defined as Eq. (12):

$$\mathrm{E.R.} = \frac{\mathrm{FWHM}}{E_\gamma} \times 100\% \tag{12}$$

where FWHM is the full width at half maximum of the full-energy peak and E_γ is the energy of the incident γ-ray. A smaller E.R. value corresponds to superior detector performance and enables more accurate identification of γ-ray sources [85]. Up to now, the maximum L.Y. of A_3BX_6 scintillators has achieved 47,000 ph/MeV under ^{137}Cs γ-ray excitation with a good E.R. of 4.0% [32]. Compared to commercial scintillators (Table 5), their performance still differs from that of commercial scintillators.

In general, A_3BX_6 MHPs feature flexible B-site composition, tunable luminescence, and good scintillation performance under high-energy excitation. These attributes endow them with great advantages for multifunctional applications in PL/EL devices, as well as x-ray or γ-ray detections, highlighting their potential as a new generation of luminescent scintillators enabled by B-site compositional engineering.

The Categories of Cation-Engineered A_3BX_6 MHPs

By engineering host and dopant cation, the radiative transition mechanisms of A_3BX_6 MHPs can be tailored, enabling diverse carrier dynamics and performance to meet the demands of potential applications in PL, EL, and high-energy photon detection. In this section, we focus on 6 categories of A_3BX_6 MHPs classified on the basis of B-site cation engineering and highlight their corresponding luminescence mechanisms and applications.

Table 4. The key metrics of A_3BX_6 MHPs single crystals (SCs) for γ-ray scintillator

Compound	Crystal size	Density (g/cm^3)	γ-Ray source	L.Y. (ph/MeV)	Decay time (ns)	E.R. (%)	Ref.
Cs_3BiCl_6	–	–	^{137}Cs	800	0.61, 9.4	–	[125]
Cs_3ScCl_6:0.5% Ce^{3+}	Φ ~ 6 × 2 mm	3.32	^{137}Cs	9,200	3.6, 54, 963	10	[135]
Li_3YCl_6:Ce^{3+}	Φ ~ 4 mm	2.45	^{137}Cs	6,185	250, 2,300	–	[146]
Cs_3LaCl_6:20% Ce^{3+}	1 × 2 × 2 mm^3	3.27	^{137}Cs	2,000	56, 380	–	[34]
Cs_3LaCl_6:40% Ce^{3+}	1 × 2 × 2 mm^3	3.27	^{137}Cs	–	54, 314	9	[34]
Cs_3LaBr_6:10% Ce^{3+}	1 × 2 × 2 mm^3	3.99	^{137}Cs	35,000	71, 437	–	[34]
Cs_3LaBr_6:40% Ce^{3+}	1 × 2 × 2 mm^3	3.99	^{137}Cs	–	37, 287	8	[34]
Cs_3LaCl_6:8% Ce^{3+}	3 × 3 × 1 mm^3	3.36	^{137}Cs	16,000	79, 291	8.6	[58]
Cs_3LaBr_6:15% Ce^{3+}	3 × 3 × 1 mm^3	3.82	^{137}Cs	32,500	44, 124	4.9	[58]
Cs_3PrCl_6	3.0 × 3.0 × 1.0 mm	–	^{137}Cs	5,900	1.5, 11.7, 72	–	[163]
Cs_3CeCl_6	>1 cm^3	3.4	^{137}Cs	21,000	50, 300	7.6	[160]
Cs_3CeCl_6	Φ 10 × 30 mm	3.4	^{137}Cs	19,000	50, 300	8.4	[17]
Cs_3GdCl_6:Ce^{3+}	4–10 mm^3	3.56	^{137}Cs	24,500	39, 129	4.5	[32]
Cs_3GdBr_6:Ce^{3+}	4–10 mm^3	4.14	^{137}Cs	47,000	72, 270	4	[32]
$(Gua)_3SbCl_6$	8 × 5 × 3 mm^3	–	^{57}Co	2,000	2,500	–	[121]

MHPs, metal halide perovskites; L.Y., light yield; E.R., energy resolution.

Table 5. The key performance parameters of commercial scintillators [LYSO = $(Lu, Y)_2SiO_5$]

Compound	Crystal size	L.Y. (ph/MeV)	E.R. (%)	Decay time (ns)	Proportionality	Afterglow	Hygroscopicity	Radiation Hardness	Ref.
NaI:Tl^+	Φ150 × 400 mm	38,000	6–7	230	Medium	Noticeable slow component	Hygroscopic	Poor–moderate	[190,191]
$LaBr_3$:Ce^{3+}	89 × 203 mm	61,000	2.7–3.2	16–25	Good	Very low	Highly hygroscopic	Moderate–good	[192,193]
SrI_2:Eu^{2+}	1–2 in	90,000	2.6–3.0	1–1.2 × 10^3	Excellent	Low	Highly hygroscopic	Moderate	[194,195]
LYSO:Ce^{3+}	64 × 220 mm	39,900	8.2	40–42	Moderate	Low	Nonhygroscopic	Excellent	[196,197]

L.Y., light yield; E.R., energy resolution.

A_3InX_6 type MHPs

As one of the P-block cations, In^{3+} has emerged as a promising candidate for B-site host composition in A_3BX_6 (i.e., A_3InX_6) MHPs because In^{3+} exhibits good chemical stability and structural compatibility, a tunable electronic structure, and unique luminescent properties (such as intrinsic luminescence, water-driven luminescence, and pressure-driven luminescence) [23,71,86]. The A-site cations in the majority of A_3InX_6 MHPs are predominantly composed of the inorganic alkali metals, such as Cs^+, K^+, and Rb^+ (Table 6). Notably, a water-driven strategy effectively induces intrinsic luminescence by incorporating H_2O into the lattice, converting A_3InX_6 into $A_2InX_5{\cdot}H_2O$ (Fig. 3A) [21,87,88]. However, such a phase transition may lead to structural instability and disrupt the electronic band structure, ultimately resulting in degraded device performance or even device failure. To manage the structural transformation of A_3InX_6 MHPs, synthesis conditions must be carefully controlled in humid environments with a polar solvent. For instance, using methanol favors the formation of pure A_3InX_6, whereas hydrochloric acid promotes the coexistence of A_3InX_6 and $A_2InX_5{\cdot}H_2O$ (Fig. 3B and C) [89]. Upon hydration, the $[InX_6]^{3-}$ octahedral framework evolves into low-symmetry $[InX_5OH_2]^{2-}$ dramatically modifying carrier recombination and intrinsic luminescence [87]. For example, Cs_3InBr_6, which exhibits STE emission (Fig. 3D) [71,90], transforms to $Cs_2InBr_5{\cdot}H_2O$ with RT phosphorescence (Fig. 3E), allowing reversible water sensing: The dehydrated powder exhibits yellow luminescence when dispersed in tetrahydrofuran, with its emission undergoing a distinct chromatic transition to red upon reaching a water content of 0.025% (v/v) (Fig. 3F) [78]. Under high pressure, the lower-symmetry $[InBr_5OH_2]^{2-}$ octahedra undergo a secondary phase transition that activates mechanoluminescence (Fig. 3G) [23]. Together,

Table 6. The key PL properties of A_3InX_6 (including PL peak, FWHM, Stokes shift, decay time and PLQY)

Compound	Sample	PL peak (nm)	FWHM (nm)	Stokes shift (nm)	Decay time	PLQY at λ_{ex}	Ref.
Cs_3InCl_6	SC	434	88	154	6.85 μs	8% (λ_{ex} = 280 nm)	[59]
Cs_3InBr_6	NC	450	–	75	8.25 ns 55.59 ns	22.3% (λ_{ex} = 375 nm)	[90]
Cs_3InCl_6	NC	397	98	107	–	24% (λ_{ex} = 370 nm)	[71]
$Cs_3In(Cl_{0.5}Br_{0.5})_6$	NC	424	89	113	–	6% (λ_{ex} = 370 nm)	[71]
Cs_3InBr_6	NC	440	80	70	–	46% (λ_{ex} = 370 nm)	[71]
$Cs_3In(Br_{0.5}I_{0.5})_6$	NC	507	87	103	–	2% (λ_{ex} = 370 nm)	[71]
Cs_3InI_6	NC	535	87	75	–	16% (λ_{ex} = 370 nm)	[71]
$Rb_3InCl_6:Sb^{3+}$	SC	497	–	127	288.5 ns 1.82 μs	95% (λ_{ex} = 324 nm)	[87]
$Cs_3InCl_6:Sb^{3+}$	NC	510	–	170	1.98 μs	93.2% (λ_{ex} = 340 nm)	[50]
$Rb_3InCl_6:Sb^{3+}$	NC	510	107	230	1.65 μs	68.01% (λ_{ex} = 320 nm)	[68]
$K_3InCl_6:Sb^{3+}$	SC	505	–	163	4.12 μs (100 K) 4.46 μs (200 K) 4.17 μs (400 K)	–	[97]
$K_3InCl_6:Sb^{3+}$	SC	555	–	213	4.69 μs (100 K) 4.52 μs (400 K)	–	[97]
$Rb_3InCl_6:Sb^{3+}$	SC	521	112	146	12.5 μs	>90% (λ_{ex} = 375 nm)	[67]
$Cs_3InCl_6:Sb^{3+}$	NC	512		172	2.07 μs	52.3% (λ_{ex} = 322 nm)	[21]
$Cs_3InCl_6:Cu^{+}$	SC	398	54	118	13.95 μs	95% (λ_{ex} = 280 nm)	[59]
$Cs_3InCl_6:Sb^{3+}/Mn^{2+}$	NC	530, 620	–	195, 295	1.61 μs	51.38% (λ_{ex} = 325 nm)	[102]

PL, photoluminescence; SC, single crystal; NC, nanocrystal; PLQY, PL quantum yield; FWHM, full width at half maximum.

the water- and pressure-driven effects in A_3InX_6 MHPs endow their intrinsic luminescence with multifunctionality.

Although the intrinsic luminescence for A_3InX_6 MHPs supports good PL applications, their PLQY remains low, primarily due to the parity-forbidden transition [91]. To improve this, as described in the "Dopant-related luminescence" section, researchers have incorporated ns^2-typed dopants into A_3InX_6 hosts. Most efforts have focused on Sb^{3+}, Bi^{3+}, and Te^{4+}, which introduce new electronic states that break the forbidden transition and enhance PL properties [87,92,93]. Upon Sb^{3+} incorporation, $A_3InX_6:Sb^{3+}$ exhibits 3 different absorption bands: the $^1S_0 \rightarrow {}^3P_1$, $^1S_0 \rightarrow {}^3P_2$, and $^1S_0 \rightarrow {}^1P_1$ (Fig. 4A) [94,95]. The emission for $Cs_3InCl_6:Sb^{3+}$ has been ascribed to the STE state based on the excited-state absorption of Sb^{3+} from $^3P_1$ to higher-energy states by femtosecond transient absorption spectra [21]. Although the $^1S_0 \rightarrow {}^3P_1$ and $^1S_0 \rightarrow {}^1P_1$ transitions exhibit distinct excitation energies, the excitons generated by both processes ultimately relax into the same STE state, resulting in emission (Fig. 4B) [96]. According to the similar luminescence mechanism, $K_3InCl_6:Sb^{3+}$ displays dual emission peaks at 505 and 555 nm, with distinct decay lifetimes observed for these 2 emission bands, indicating the existence of 2 STE emission (Fig. 4C) [97]. In addition, Sb^{3+} imparts high resistance to thermal quenching to the material, and the $Rb_3InCl_6:Sb^{3+}$ is applied for high-temperature white LED with exceptional thermal quenching resistance up to 500 K (Fig. 4D) [67].

In contrast to the bright emission observed in $A_3InX_6:Sb^{3+}$ MHPs, $Cs_3InCl_6:Te^{4+}$ remains negligible PL at RT [88]. However, the Te^{4+} doping strategy of water-driven phase transition induces bright-yellow luminescence in $A_2InCl_5{\cdot}H_2O$ ($A = Cs^+$ and Rb^+) [88,92,98,99]. One application is a promising platform for anticounterfeiting with ethanol-sensitive structural transformation between $Cs_2InCl_5{\cdot}H_2O:Te^{4+}$ and $Cs_3InCl_6:Te^{4+}$ (Fig. 4E) [88]. The other application is visual temperature monitoring through the color-changing temperature indicator light in ratio mode, with luminescence color transition from orange–red to white (Fig. 4F) [92]. However, PL vanishes from RT to 480 K due to phase transition to $Rb_3In_2Cl_9$, limiting its applicable temperature range [98]. The Bi^{3+} doping strategy in $Cs_2InCl_5{\cdot}H_2O$ induces a phase transition similar to that observed with Te^{4+} doping, which extends the luminescent temperature window to 300 to 460 K (Fig. 4G and H) [93].

Beyond ns^2-typed dopants act as sensitizers, transition-metal cations and Ln^{3+} are regarded as effective alternatives through ET process [20], the STE–transition metal ET is typically governed by Dexter exchange interaction [100], whereas STE–Ln^{3+} transfer mainly occurs via dipole–dipole interaction [101]. For example, in $Cs_3InCl_6:Sb^{3+},Mn^{2+}$, ET from STEs to Mn^{2+} facilitates simultaneous green STE emission and Mn^{2+}-derived red emission (Fig. 5A). The white LED with $Cs_3InCl_6:Sb^{3+}$, Mn^{2+} achieves higher color rendering index (CRI = 85.5) and correlated color temperature (CCT = 6,452 K) than that of $Cs_3InCl_6:Sb^{3+}$ (Fig. 5B) [102]. Similarly, $Cs_3InCl_6:Sb^{3+},Ln^{3+}$ (Ln^{3+} = Nd^{3+}, Sm^{3+}, Tb^{3+}, Dy^{3+}, Ho^{3+}, Er^{3+}, Tm^{3+}, and Yb^{3+}) leverages ET from STE to Ln^{3+} to achieve NIR luminescence (Fig. 5C).

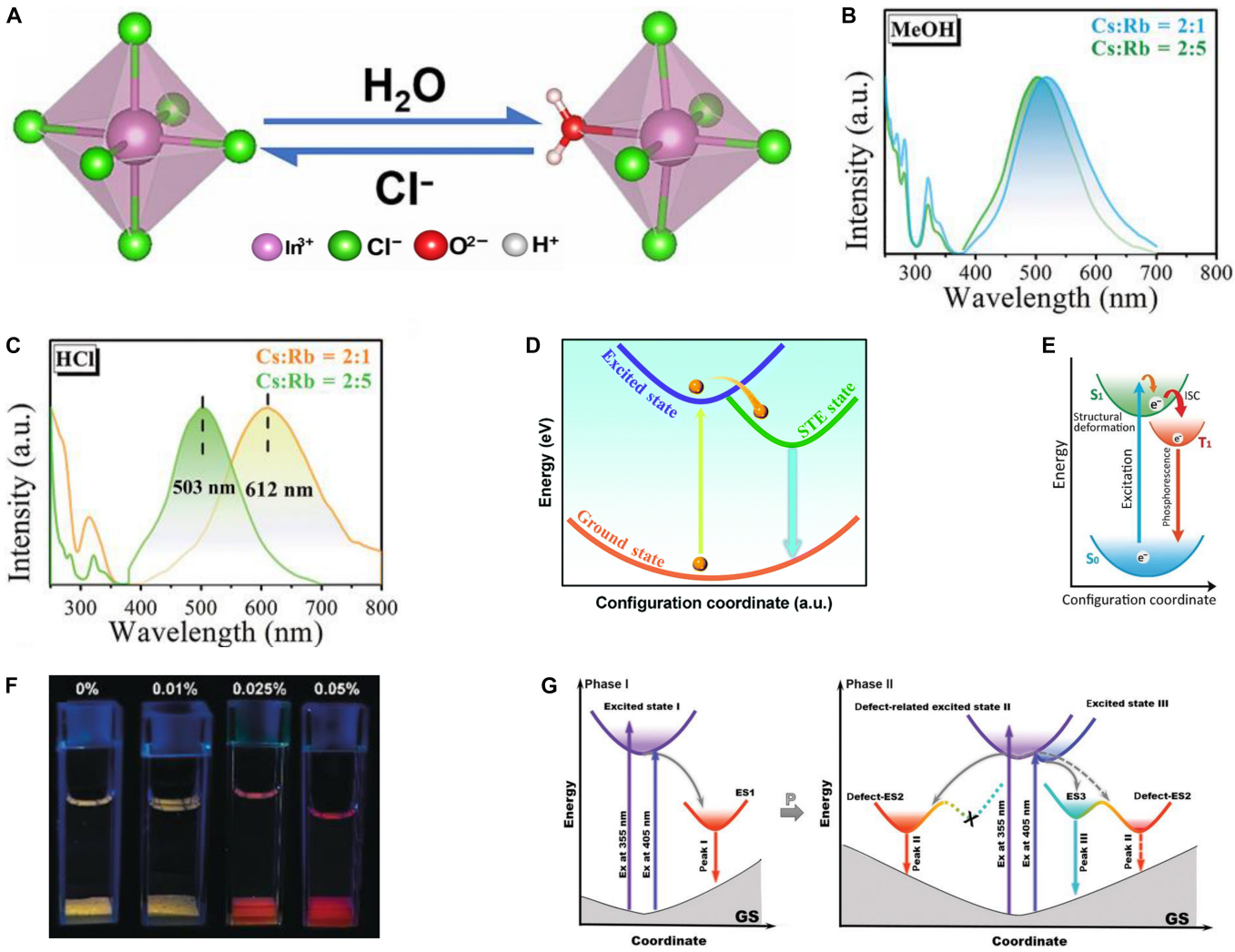


Fig. 3. (A) The transformation between a regular octahedron $[InCl_6]^{3-}$ and distorted octahedron $[InX_5OH_2]^{2-}$. Adapted with permission [87]. Copyright 2020, published by Wiley-VCH. (B) The photoluminescence (PL) and PL excitation (PLE) of pure A_3InCl_6 synthesized from methanol. MeOH, methanol. Adapted with permission [89]. Copyright 2021, published by Wiley-VCH. (C) The PL and PLE of the coexisting samples of A_3InCl_6 and $A_2InX_5{\cdot}H_2O$ were synthesized using hydrochloric acid. Adapted with permission [89]. Copyright 2021, published by Wiley-VCH. (D) Schematic of the photophysical processes in Cs_3InBr_6. Adapted with permission [71]. Copyright 2021, published by Royal Society of Chemistry. (E) Configurational coordinate diagram illustrating the origin of PL in $Cs_2InBr_5{\cdot}H_2O$. ISC, intersystem crossing. Adapted with permission [78]. Copyright 2019, published by Wiley-VCH. (F) The dehydrated mixture is contained in the tetrahydrofuran solution. The luminescence phenomenon of different water volumes (0 to 0.05%, v/v). Adapted with permission [78]. Copyright 2019, published by Wiley-VCH. (G) Schematic illustrations of the relaxation mechanisms of the self-trapped excitons (STEs) in phase I (left) and phase II (right). Ex, excitation; GS, ground state. Adapted with permission [23]. Copyright 2021, published by Wiley-VCH.

Notably, Cs_3InCl_6:Sb^{3+},Nd^{3+} exhibits both green and NIR emissions, while Cs_3InCl_6:Sb^{3+},Eu^{3+} exhibits excitation-wavelength-dependent luminescence due to the absence of ET between STEs and Eu^{3+}, enabling anticounterfeiting applications (Fig. 5D) [50]. In addition, introducing an ET pathway between Bi^{3+} and Mn^{2+} in $Cs_2InCl_5{\cdot}H_2O$:Bi^{3+},Mn^{2+} enhances its originally weak emission by 60-fold (Fig. 5E) [103]. These strategies highlight the synergistic potential of codoping and structural engineering to modulate luminescence in A_3InX_6 MHPs for multifunctional optoelectronic applications.

Apart from their application of PL and EL, A_3InX_6 MHPs have also been explored for scintillation applications. The emerging studies highlight their immense potential in this field. For instance, the L.Y. of Rb_3InCl_6:Sb^{3+} NCs exhibit 1.65 times higher than that of $Bi_4Ge_3O_{12}$ (BGO) under x-ray excitation, reaching 15,500 ph/MeV (Fig. 5F). Composite films fabricated with polysulfone and Rb_3InCl_6:Sb^{3+} achieve a spatial resolution of 18.5 lp/mm at an MTF of 0.2, showcasing promise for bioimaging applications (Fig. 5G). Radiation resistance is another critical parameter for scintillators [68]. Rb_3InCl_6:Sb^{3+} retains 85% of its initial RL intensity after 30-min exposure to a dose rate of 5.2 mGy/s and maintains its initial RL intensity even at cumulative doses of 500 Gy_{air} under a high dose rate of 0.5 Gy/s (Fig. 5H and I) [65,68]. These results underscore the outstanding radiation hardness of In^{3+}-based MHPs and their potential for x-ray imaging. However, their performance under γ-ray irradiation remains unexplored, necessitating further investigation to unlock their full capabilities in high-energy radiation detection. This pioneering work positions In^{3+}-based MHPs as promising candidates for next-generation scintillators, bridging the gap between optical excellence and functional radiation detection.

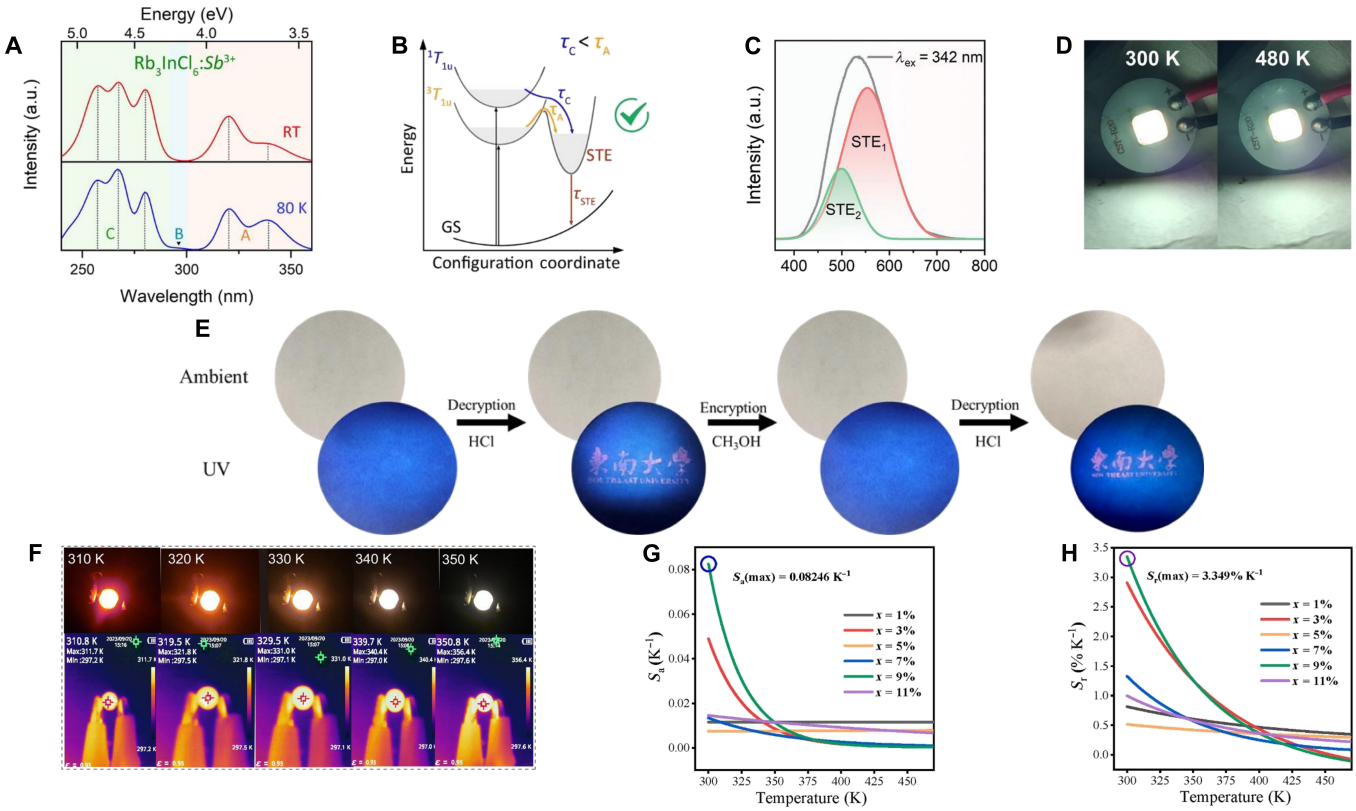


Fig. 4. (A) Photoluminescence (PL) excitation (PLE) spectra of $Rb_3InCl_6:Sb^{3+}$ collected at room temperature (RT) and 80 K. Adapted with permission [96]. Copyright 2022, published by American Chemical Society. (B) The photophysical process of $Rb_3InCl_6:Sb^{3+}$. GS, ground state. Adapted with permission [96]. Copyright 2022, published by American Chemical Society. (C) Peak-fitted PL spectra of $K_3InCl_6:Sb^{3+}$. Adapted with permission [97]. Copyright 2024, published by Wiley-VCH. (D) Photographs of the white light-emitting diode (LED) based on $Rb_3InCl_6:Sb^{3+}$ at low current (left) and high current (right). Adapted with permission [67]. Copyright 2024, published by American Chemical Society. (E) Reversible fluorescence switching between $Cs_2InCl_5{\cdot}H_2O:Te^{4+}$ and $Cs_3InCl_6:Te^{4+}$. Adapted with permission [88]. Copyright 2023, published by Academic Press Inc. (F) The LED color changes as the temperature is monitored from 300 to 350 K using a temperature gun. Adapted with permission [92]. Copyright 2025, published by Royal Society of Chemistry. (G) Corresponding absolute sensitivity (S_a) and (H) relative sensitivity (S_r) values of $Cs_2InCl_5{\cdot}H_2O:xBi^{3+}$. Adapted with permission [93]. Copyright 2024, published by Elsevier.

A_3SbX_6-type MHPs

P-block metal ion Sb^{3+} can not only act as dopant in enhancing the luminescence in A_3InX_6 MHPs but also serve as the B-site host composition to construct A_3SbX_6 MHPs. However, all-inorganic A_3SbX_6 faces the challenge of low PL efficiency, primarily due to crystal defects, which act as multiple nonradiative recombination centers [104,105]. For instance, K_3SbCl_6 NCs exhibit a broad STE emission centered at 440 nm (FWHM = 102 nm); through the optimization of the synthesis temperature, the maximum PLQY reached 22.3% (Fig. 6A) [104]. However, the presence of defects leads to poor optical properties in materials synthesized at RT, resulting in limited research on all-inorganic A_3SbX_6 compounds.

Compared to all-inorganic A_3SbX_6 MHPs, implementation of the metal complexes as the A-site to construct A_3SbX_6 organic–inorganic hybrid perovskites (OIHPs) can substantially strengthen perovskite framework robustness and lattice coherence, thereby enhancing charge carrier mobility through optimized defect configurations and radiation hardness [106–108]. For example, $[Na(DMSO)_2]_3SbBr_6$ demonstrates a broadband emission with a remarkable Stokes shift of 200 nm and a PLQY of 60%. The measured electrical–optical–electrical (EOE) frequency response yields a 7.2-MHz bandwidth, which enables an 81.6-Mbps data transmission rate using orthogonal frequency-division multiplexing (Fig. 6B and C) [109]. Similarly, [C@Cs]$_2$CsSbBr$_6$ (C = 18-crown-6) exhibits a broad orange emission (1.3 eV; FWHM = 0.35 eV) under 365-nm excitation. Its temperature-dependent PL lifetime yields a thermal sensitivity coefficient (α) of 0.04 °C^{-1}, significantly surpassing conventional thermoluminescent materials (α = 0.005 to 0.03 °C^{-1}) (Fig. 6D), highlighting its potential for high-sensitivity thermal imaging applications [110].

In addition, the incorporation of organic cations imparts structural flexibility and dynamic characteristics to the crystal lattice, providing enhanced freedom and pathways for exciton migration and recombination, thereby improving luminescence efficiency [111]. Notably, Sb^{3+}-based OIHPs achieve a record PLQY of up to 100% (Fig. 6E) [74]. Relative to their inorganic Sb^{3+}-based MHPs counterparts, Sb^{3+}-based OIHPs exhibit broader Stokes shifts. For instance, $[C_5mim][Mim]_2SbCl_6$ ($[C_5mim]^+$ = 1-pentyl-3-methylimidazolium; $[Mim]^+$ = *N*-methylimidazolium) demonstrates a Stokes shift of 335 nm, significantly larger than those of other Sb^{3+}-based OIHPs such as $[primim]_3SbCl_6$, $[PMA]_3SbBr_6$, and $[DphgH]_3SbCl_6$ ([primim] = 1-propyl-3-methylimidazolium, [PMA] = phenylmethylammonium, [Dphg] = *N*,*N*′-diphenylguanidine) [112–114]. This phenomenon arises from the disruption of supramolecular interactions within imidazolium-based groups, which triggers pronounced anionic lattice distortions [115]. Intriguingly, certain OIHPs exhibit stimulus-responsive luminescence, enabling advanced applications in information encryption. For example, $[DPA]_3SbCl_6$ (DPA =

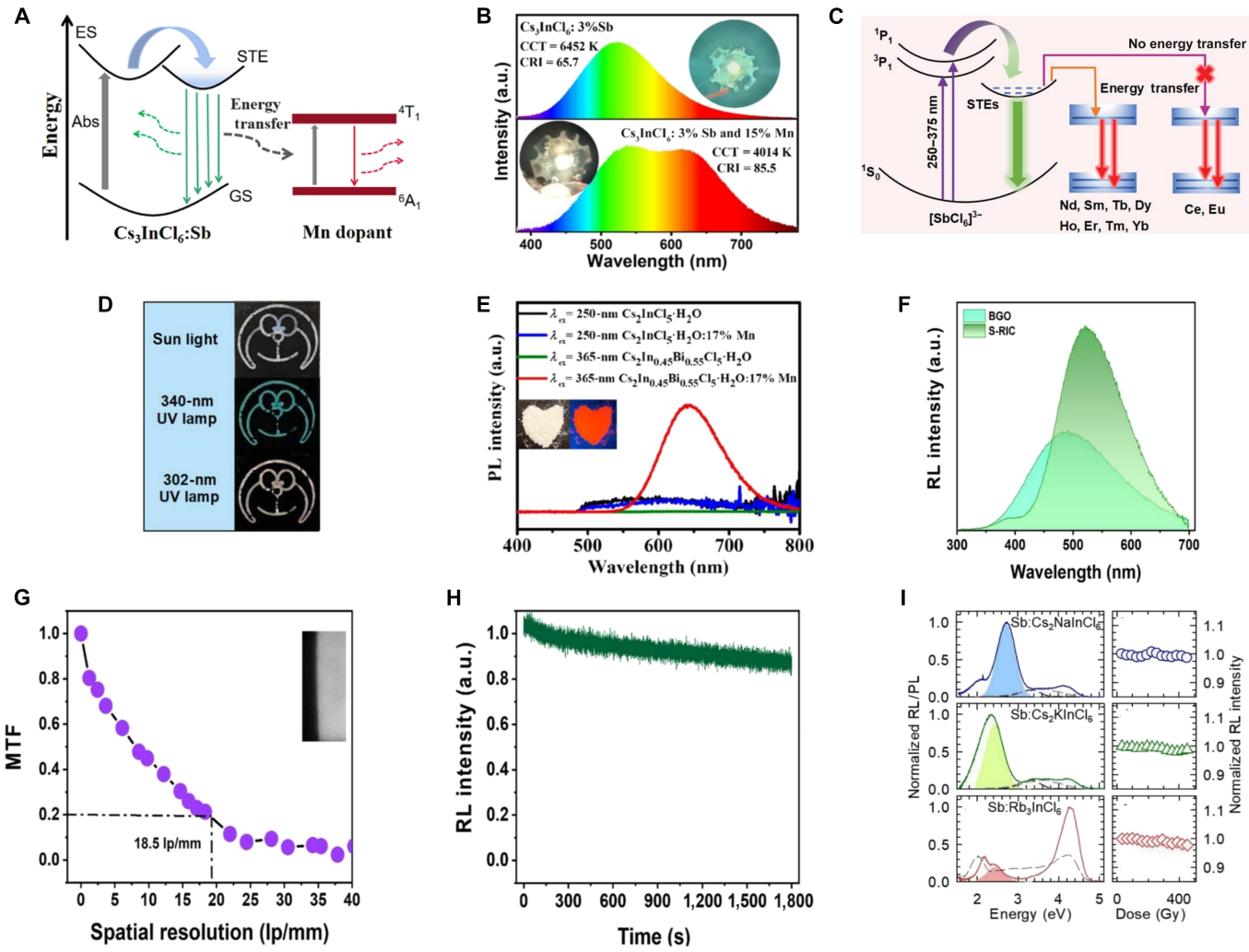


Fig. 5. (A) Proposed photoluminescence (PL) mechanism of Sb^{3+}/Mn^{2+}-codoped Cs_3InCl_6 NCs. Adapted with permission [102]. GS, ground state; ES, excited state; Abs, absorption. Copyright 2024, published by American Chemical Society. (B) Emission spectra of Cs_3InCl_6:3% Sb^{3+} and Cs_3InCl_6:3% Sb^{3+},15% Mn^{2+}-based light-emitting diodes (LEDs) under 317-nm chip excitation. Adapted with permission [102]. Copyright 2024, published by American Chemical Society. (C) Schematic diagram of Cs_3InCl_6:Sb^{3+},Ln^{3+} (Ln^{3+} = Nd^{3+}, Sm^{3+}, Tb^{3+}, Dy^{3+}, Ho^{3+}, Er^{3+}, Tm^{3+}, and Yb^{3+}). Adapted with permission [50]. Copyright 2023, published by Wiley-VCH. (D) Images of security patterns made of Cs_3InCl_6:1% Sb^{3+},50% Eu^{3+} nanocrystals (NCs). Adapted with permission [50]. Copyright 2023, published by Wiley-VCH. (E) PL spectra and patterns for the $Cs_2InCl_5·H_2O$:Bi^{3+},Mn^{2+}. Adapted with permission [103]. Copyright 2023, published by American Chemical Society. (F) Radioluminescence (RL) spectra of Rb_3InCl_6:Sb^{3+} and $Bi_4Ge_3O_{12}$ (BGO) under x-ray excitation. Adapted with permission [68]. Copyright 2025, published by Elsevier. (G) Modulation transfer function (MTF) curves of the film of Rb_3InCl_6:Sb^{3+} NC and polysulfone. Adapted with permission [68]. Copyright 2025, published by Elsevier. (H) RL intensity of Rb_3InCl_6:Sb^{3+} under continuous x-ray irradiation. Adapted with permission [68]. Copyright 2025, published by Elsevier. (I) The RL spectra of Rb_3InCl_6:Sb^{3+}, Cs_2KInCl_6:Sb^{3+}, and $Cs_2NaInCl_6$:Sb^{3+} with increasing cumulative dose up to 500 Gy. Adapted with permission [65]. Copyright 2021, published by American Chemical Society.

dipropylamine) enables a dual-mode encryption–decryption process mediated by ethanol exposure: Encrypted information remains invisible under ambient and UV light due to the inherent transparency of $SbCl_3$, while decryption is achieved by spraying with a [DPA]Cl ethanol solution to generate fluorescent $[DPA]_3SbCl_6$ under UV illumination. Subsequent methanol treatment quenches the emission for re-encryption, followed by dissolution recrystallization to restore fluorescence for secondary decryption (Fig. 6F and G) [116].

While most organic A-site cations primarily enhance luminescence efficiency by introducing structural flexibility and modulating carrier recombination without altering the intrinsic luminescence mechanism, certain organic cations, such as $Bzmim^+$ (Bzmim = 1-benzyl-3-methylimidazolium), fundamentally modify the optoelectronic behavior. When $Bzmim^+$ occupies the A-site to form $[Bzmim]_3SbCl_6$, it undergoes phase transitions analogous to those observed in In^{3+}-based MHPs [21,87], albeit through distinct pathways. In In^{3+}-based MHPs (e.g., Cs_3InCl_6), phase transitions involve the replacement of a CsCl unit by H_2O under humid conditions, accompanied by O^{2-} substituting Cl^- in the $[InCl_6]^{3-}$ octahedral framework [21]. In contrast, the phase transition in $[Bzmim]_3SbCl_6$ is driven by the extraction and reinsertion of [Bzmim]Cl within the $[Bzmim]_{n-3}SbCl_n$ structure (Fig. 7A) [117]. This structural reorganization induces tunable luminescence: The emission difference between $[Bzmim]_3SbCl_6$ (λ_{em} = 525 nm) and $[Bzmim]_2SbCl_5$ (λ_{em} = 600 nm) arises from a coordination-induced redshift in the halide–metal charge transfer within the $[SbCl_n]^{3-n}$ complexes [118]. This structural reorganization-induced color change can be applied to information encryption. For example, the word

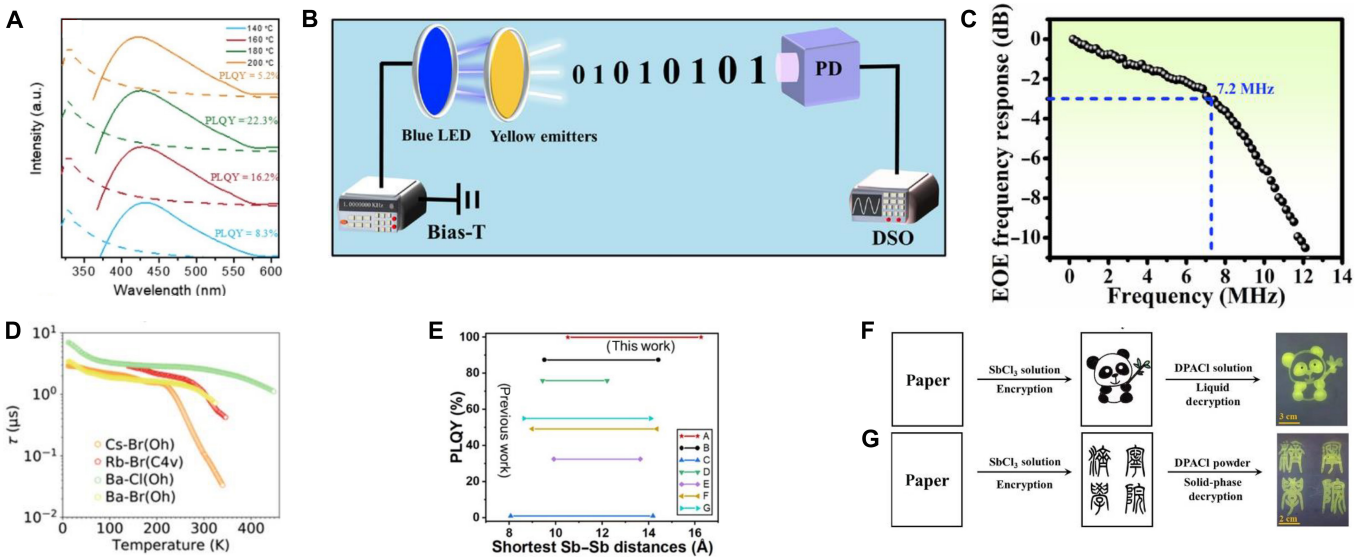


Fig. 6. (A) Absorption and photoluminescence (PL) spectra of K_3SbCl_6 nanocrystals (NCs) at different synthesized temperatures. Adapted with permission [104]. Copyright 2021, published by Elsevier. (B) Electrical–optical–electrical (EOE) frequency response of the $[Na(DMSO)_2]_3SbBr_6$-based optical converter [109]. DSO, digital storage oscilloscope; PD, photodetector. Copyright 2022, published by Wiley-VCH. (C) The EOE frequency response. Adapted with permission [109]. Copyright 2022, published by Wiley-VCH. (D) Temperature-dependent decay time for $[C@Cs]_2CsSbBr_6$ and its derivatives. Adapted with permission [110]. Copyright 2020, published by American Chemical Society. (E) Correlation between shortest Sb–Sb distances and PL quantum yield (PLQY) for 0D Sb^{3+}-based halides. (Among them, A is $(gua\text{-}DPG)_3SbCl_6$ [74], B is $[Bzmim]_3SbCl_6$ [118], C is $(PMA)_3SbBr_6$ [112] , D is $[DMPZ]_2SbCl_6{\cdot}Cl{\cdot}(H_2O)_2$ [182], E is $[Prmim]_3SbCl_6$ [113], F is $[Hmim]_3SbCl_6$ [113], and G is $H_3SbBr_6(L)_6$ [183].) Adapted with permission. Copyright 2023, published by American Chemical Society. The information encryption and decryption process for (F) panda pattern and (G) Chinese character, respectively. Adapted with permission [116]. Copyright 2022, published by Elsevier.

"disagree" written on paper was encrypted and required decryption using specific [Bzmim]Cl solution concentrations, thermal treatment, and UV observation (Fig. 7B) [117]. In addition, leveraging the low melting point and thermally responsive luminescence of $[Bzmim]_3SbCl_6$, direct laser writing on paper coated with this material enabled reversible information writing and erasure through localized melting and luminescence modulation (Fig. 7C) [118]. A_3SbX_6 MHPs also show promising application in scintillation. Abovementioned $[Bzmim]_3SbCl_6$ generates a single radiative center at 540 nm with an L.Y. of 24,600 ph/MeV (Fig. 7D). When integrated into $[Bzmim]_3SbCl_6$@PMMA film scintillator fabricated through this strategy enables noninvasive internal imaging of earphones, demonstrating a high spatial resolution of 8.3 lp/mm (Fig. 7E and F) [119]. In addition to the reported 0D A_3SbX_6 MHPs, $[SbI_6]^{3-}$ isolated octahedra tend to form higher-dimensional architectures (3D and 2D) when constructing OIHPs, while also finding applications in scintillation detection. X-ray detectors fabricated using 2D $FPEA_3SbI_6$ (FPEA = 4-fluorophenethylammonium) exhibit a LoD of 0.123 μGy/s and a spatial resolution of 1.59 lp/mm for imaging applications [120]. Similarly, 3D $[Mor]_2RbSbI_6$ (Mor = morpholinium)-based detectors achieve exceptional sensitivity (1.09×10^4 μC·Gy^{-1}·cm^{-2}) and an ultralow detection limit of 3.1 nGy/s [105]. In contrast, the 0D Gua_3SbCl_6 (Fig. 7G) demonstrates an L.Y. of 2,300 ± 500 ph/MeV under x-ray excitation (Fig. 7H). Furthermore, Sb^{3+}-based OIHPs exhibit responsiveness to higher-energy γ-rays: Gua_3SbCl_6 achieves an L.Y. of 1,800 ± 500 ph/MeV under 120-keV ^{60}Co γ-ray irradiation (Fig. 7I) [121].

A_3BiX_6-type MHPs

As another P-block cation, Bi^{3+} is also a promising B-site constituent for constructing A_3BiX_6 MHPs [122]. The greater atomic mass of Bi^{3+} relative to Sb^{3+} reduces lattice vibrational frequencies, thereby enhancing carrier mobility and improving the suitability of A_3BiX_6 for photodetector applications [123,124]. The intrinsic luminescence of Cs_3BiCl_6 single crystal at 390 nm arises from the parity-forbidden $^3T_{1u} \rightarrow {}^1A_{1g}$ transition of Bi^{3+}, while the dual-band absorption at 220 and 330 nm originates from the $^1A_{1g} \rightarrow {}^1T_{1u}$ and $^1A_{1g} \rightarrow {}^3T_{1u}$ transitions, respectively [125]. Similarly, Cs_3BiBr_6 NCs display blue emission at RT with a PLQY of merely 6.03%, which could increase to 22% upon oleic acid passivation [126]. The poor luminescence efficiency of Cs_3BiX_6 due to strong exciton–phonon coupling and severe nonradiative recombination has shifted research focus toward its potential for UV dual-band photodetection.

The fabricated photodetectors based on Cs_3BiBr_6 single crystals show an impressive detectivity of 8×10^8 Jones and a low dark current under 400-nm illumination (Fig. 8A and B) [123]. Given that Cs_3BiBr_6 and $Cs_3Bi_2Br_9$ are interconvertible, Cs_3BiBr_6 can undergo phase transformation to form $Cs_3Bi_2Br_9$ during synthesis using identical precursors [18,122]. Fang's group [127] successfully constructed a $Cs_3BiBr_6/Cs_3Bi_2Br_9$ bulk heterojunction applying with dual-band photodetection (Fig. 8C). In this regard, the self-powered ITO (ITO = indium tin oxide)/$Cs_3BiBr_6/Cs_3Bi_2Br_9$/Au photodetector achieves responsivities of 59.4 mA/W at 360 nm and 3.09 mA/W at 450 nm (Fig. 8D) [124].

To overcome the limitation of inherent challenges in photodetectors, such as narrow optical absorption range and low carrier mobility, the favorable band alignment between Cs_3BiCl_6 and GaN enables the formation of a built-in electric field at their heterojunction interface [128]. The interfacial electric field suppresses carrier recombination and separates photogenerated electron–hole pairs, significantly enhancing responsivity and detection sensitivity. The Cs_3BiCl_6/GaN heterojunction photodetector achieves exceptional performance: strong specific

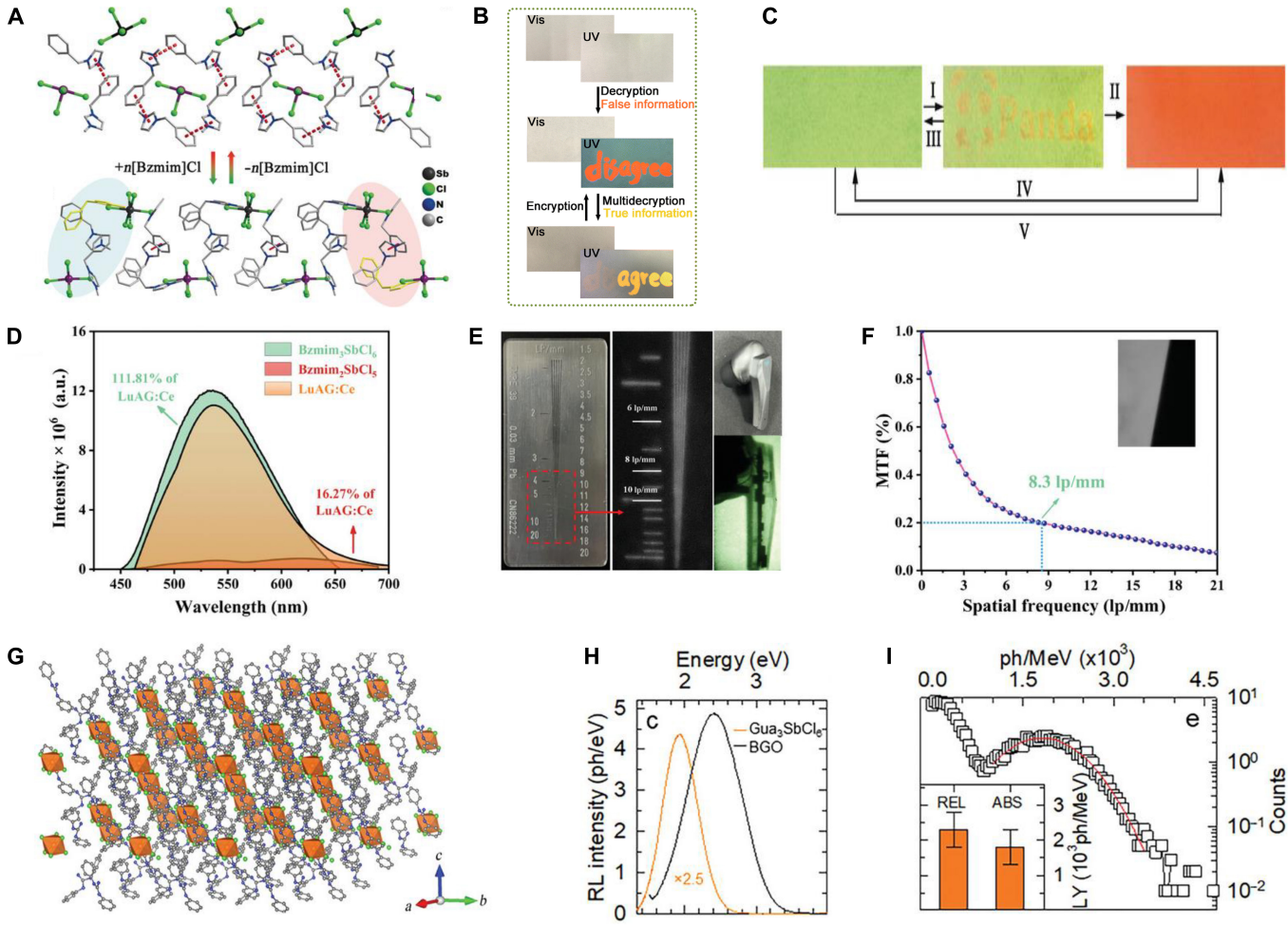


Fig. 7. (A) Structural transformation between $[Bzmim]_3SbCl_6$ and $[Bzmim]_2SbCl_5$. Adapted with permission [118]. Copyright 2019, published by Wiley-VCH. (B) Digital photographs of the paper before and after heating under 390-nm ultraviolet (UV) light, with words written using [Bzmim]Cl and $SbCl_3$ inks. Vis, visible. Adapted with permission [117]. Copyright 2025, published by Royal Society of Chemistry. (C) Schematic of the laser-based encryption/decryption process: (I) Printing the paper with a laser engraver; (II) blacking out in a moist environment; (III) aging at 353 K for initialization; (IV) heating at 353 K; and (V) keeping in moisture for 6 h [118]. Copyright 2019, published by Wiley-VCH. (D) The radioluminescence (RL) and light yield (L.Y.) of $Bzmim_3SbCl_6$. Adapted with permission [119]. Copyright 2024, published by Wiley-VCH. (E) The x-ray images of a standard resolution pattern plate and an earphone based on $[Bzmim]_3SbCl_6$@PMMA as the scintillator. Adapted with permission [119]. Copyright 2024, published by Wiley-VCH. (F) Modulation transfer function (MTF) curve of the $[Bzmim]_3SbCl_6$@PMMA scintillator film. Adapted with permission [119]. Copyright 2024, published by Wiley-VCH. (G) Configuration of Gua_3SbCl_6 supercell. Adapted with permission [121]. Copyright 2023, published by Wiley-VCH. (H) RL spectra of Gua_3SbCl_6 and $Bi_4Ge_3O_{12}$ (BGO). Adapted with permission [121]. Copyright 2023, published by Wiley-VCH. (I) L.Y. of Gua_3SbCl_6 under ^{57}Co γ-ray excitation. Adapted with permission [121]. REL, relative emission intensity; ABS, absorption. Copyright 2023, published by Wiley-VCH.

detectivity (1.23×10^{12} Jones) and ultrafast response (τ_r/τ_f = 28/190 μs). Its intrinsic UV dual-band selectivity enables applications in logic operations and encrypted optical communication systems (Fig. 8E).

On the one hand, the A_3BiX_6 MHPs show strong application into photodetection. On the other hand, the absence of PL in A_3BiCl_6 (A = Rb and Cs) at RT is attributed to the strong exciton–phonon coupling with the coupling constant reaching 693 meV, which facilitates severe nonradiative recombination [33], structural and vibrational studies indicate that the RT luminescence quenching of A_3BiX_6 is closely related to pronounced local distortion of isolated $[BiX_6]^{3-}$ octahedra and strong lattice anharmonicity [129]. To enhance the efficiency of radiative recombination, ns^2-typed Sb^{3+} was incorporated into Rb_3BiCl_6 (i.e., Rb_3BiCl_6:Sb^{3+}), resulting in a bright STE emission with a reduced coupling constant of 347 meV (Fig. 8F), the PLQY increased to 33% [33]. The strategy of structural modifications further improved the PLQY, achieving a maximum of 45% in $Rb_2CsBiCl_6$:Sb^{3+} (Table 7) [130–132]. Beyond ns^2-type dopants, transition-metal cation Mn^{2+} is also regarded as effective dopant. Due to the primarily participation of Mn d orbitals in the conduction band minimum (CBM), both $(Cs_2K)BiCl_6$:Mn^{2+} and Cs_3BiCl_6:Mn^{2+} can exhibit a narrow bandgap and an allowed $^4T_1 \rightarrow {}^6A_1$ transition [18,133]. Direct Mn^{2+} doping yields weak NIR emission, while Sb^{3+}, Cr^{3+} codoping enables efficient ET (PLQY = 11.03%). Sb^{3+}-induced quasi-2D domains further enhance PLQY to 30.68%, enabling multifunctional NIR LEDs for night vision, penetration imaging, and vein visualization [134].

Although Cs_3BiCl_6 exhibits negligible emission at RT, its PL intensity significantly increases when the temperature falls below 80 K, as shown in Fig. 8G [122,125]. This behavior suggests that radiative recombination becomes more favorable at low temperatures under UV excitation, due to the suppression of thermally activated nonradiative processes. Under high-energy radiation excitation, a large number of

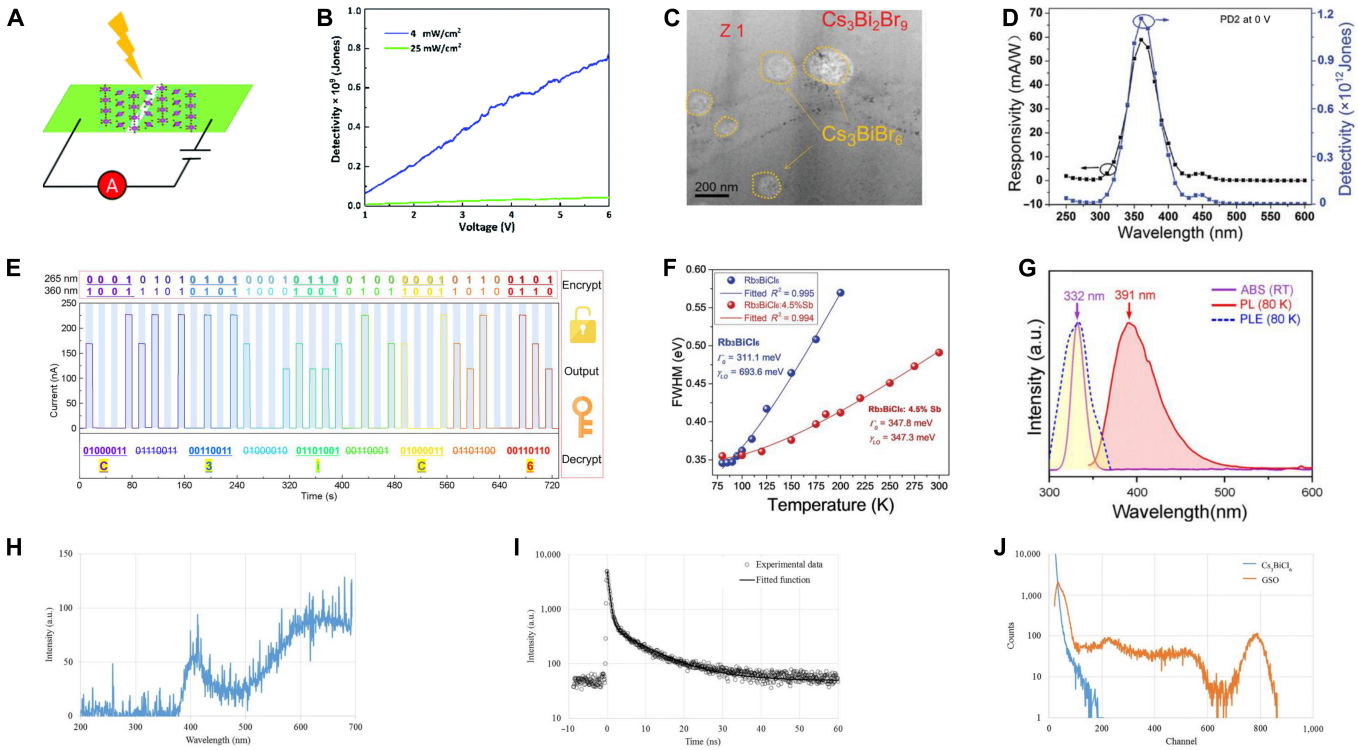


Fig. 8. (A) Schematic diagram of the photodetector based on Cs_3BiBr_6. Adapted with permission [123]. Copyright 2019, published by Royal Society of Chemistry. (B) Comparison of the detectivity at 2 different light densities. Adapted with permission [123]. Copyright 2019, published by Royal Society of Chemistry. (C) Transmission electron microscopy image for Cs_3BiBr_6 and $Cs_3Bi_2Br_9$ interface. Adapted with permission [127]. Copyright 2022, published by Wiley-VCH. (D) Responsivity and detectivity spectra of Cs_3BiBr_6/$Cs_3Bi_2Br_9$ bulk. Adapted with permission [124]. Copyright 2022, published by Wiley-VCH. (E) Schematic diagram and effective digital data for encrypted photocommunication based on Cs_3BiCl_6/GaN heterojunction. Adapted with permission [128]. Copyright 2025, published by Wiley-VCH. (F) Fitting results of temperature-dependent full width at half maximum (FWHM) for Rb_3BiCl_6 and Rb_3BiCl_6:4.5% Sb^{3+}. Adapted with permission [33]. Copyright 2021, published by Wiley-VCH. (G) Absorption, photoluminescence (PL), and PL excitation (PLE) spectra of Cs_3BiCl_6 nanocrystals (NCs). Adapted with permission [122]. Copyright 2020, published by Springer. (H) X-ray induced radioluminescence (RL) of Cs_3BiCl_6 single crystal. Adapted with permission [125]. Copyright 2016, published by Elsevier. (I) Pulsed x-ray induced decay profile of Cs_3BiCl_6 single crystal. Adapted with permission [125]. Copyright 2016, published by Elsevier. (J) Pulse-height spectra of Gd_2SiO_5:Ce^{3+} (GSO) and Cs_3BiCl_6 under ^{137}Cs γ-ray excitation. Adapted with permission [125]. Copyright 2016, published by Elsevier.

Table 7. The key PL properties of A_3BiX_6 (including PL peak, FWHM, Stokes shift, decay time and PLQY)

Compound	Sample	PL peak (nm)	FWHM (nm)	Stokes shift (nm)	Decay time (μs)	PLQY at λ_{ex}	Ref.
Cs_3BiCl_6	NC	391 (80 K)	60	59	–	–	[122]
Cs_3BiBr_6	NC	435	–	–	2.77×10^{-3} (40.19%) 12.16×10^{-3} (26.35%)	6.03% ($\lambda_{ex} = 372$ nm)	[198]
$Rb_2CsBiCl_6$:Sb^{3+}	SC	560	133	182	452×10^{-3}; 1.29	45% ($\lambda_{ex} = 378$ nm)	[130]
Rb_3BiCl_6:Sb^{3+}	SC	625	170	245	4.1	33.6% ($\lambda_{ex} = 380$ nm)	[33]
Cs_3BiCl_6:Sb^{3+}	SC	555	132	175	0.54; 1.45	15.85% ($\lambda_{ex} = 380$ nm)	[131]
Cs_3BiCl_6:Sb^{3+}	SC	885	250		72.08 (765 nm) 329.75×10^{-3} (885 nm)	30.68% ($\lambda_{ex} = 532$ nm)	[134]
$(Cs_2K)BiCl_6$:Mn^{2+}	SC	605	–	235	60	–	[133]
Cs_3BiCl_6:Mn^{2+}	NC	607	80	174	20	2.5% ($\lambda_{ex} = 430$ nm)	[18]

PL, photoluminescence; SC, single crystal; NC, nanocrystal; PLQY, PL quantum yield; FWHM, full width at half maximum.

high-energy electron–hole pairs are generated, creating dense excitation conditions that allow radiative recombination pathways to effectively compete with nonradiative processes. As a result, Cs_3BiCl_6 exhibits dual emission bands at 400 and 600 to 700 nm under x-ray excitation, accompanied by fast decay kinetics ($\tau_1 = 0.61$ ns [43%] and $\tau_2 = 9.4$ ns [57%]) (Fig. 8H

and I). Notably, an L.Y. of approximately 800 ph/MeV has been achieved under ^{137}Cs γ-ray irradiation (Fig. 8J), highlighting the potential of Cs_3BiCl_6 for radiation detection applications [125].

A_3REX_6-type MHPs with empty f orbitals

As for the A_3REX_6 MHPs, RE^{3+} with empty f orbitals (since La^{3+} has empty f orbitals and Sc^{3+} and Y^{3+} lack f orbitals, these ions are collectively treated as RE^{3+} with empty f orbitals in this work) is similar to the P-block cation as B-site composition, including the intrinsic luminescence mechanism and water-driven phase transition. The intrinsic luminescence for Cs_3ScCl_6, Cs_3YCl_6, and Cs_3LaCl_6 single crystals is ascribed to STE emission [72,135,136], albeit with relatively low efficiencies, as in the case of Cs_3YCl_6, the PLQY is merely 3.1% [72]. Relatively, their NCs could achieve better PL properties due to the surface modifications by oleic acid ligands [137,138]. Based on this strategy, the PLQY of Cs_3YCl_6 NCs achieves up to 89.3%, while its single crystal is still limited to the modest PLQY (<10%) [139]. The water-driven strategy is also effective for incorporating H_2O into the lattice, converting A_3REX_6 into $A_2REX_5{\cdot}H_2O$. The phase-transformed Cs_3ScX_6 and $Cs_2ScCl_5{\cdot}H_2O$ demonstrate excitation wavelength-dependent luminescence at RT (Fig. 9A). The femtosecond transient absorption, temperature-dependent PL, and time-resolved PL studies reveal that this tunable emission originates from 2 distinct STE states. Selective excitation to different STE states through wavelength modulation enables emission color tuning from cyan through white to yellow [140].

Although $Cs_2ScCl_5{\cdot}H_2O$ exhibits excitation wavelength-dependent PL with low efficiency, using Sb^{3+} as a ns^2-typed

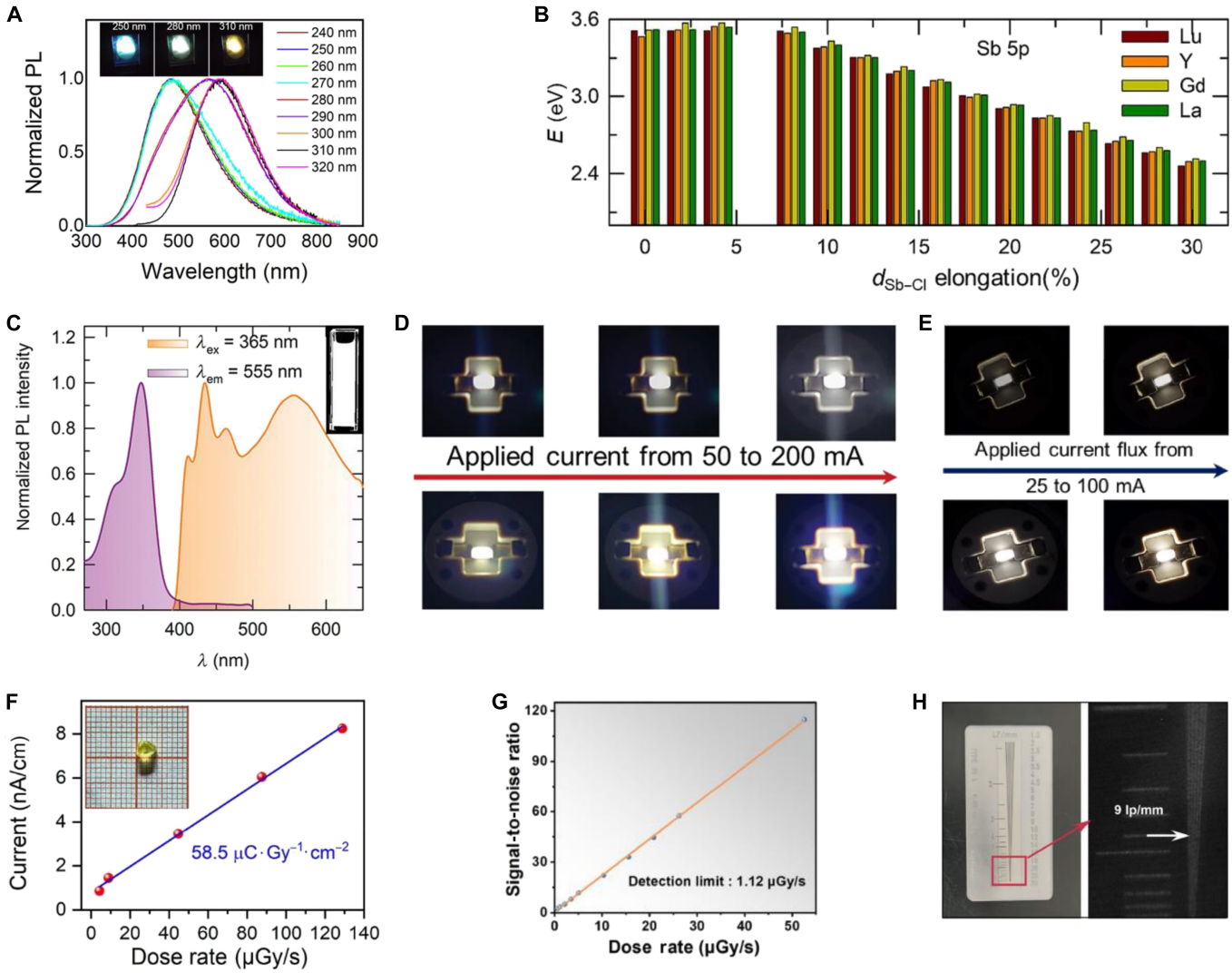


Fig. 9. (A) Photoluminescence (PL) spectra of $Cs_2ScCl_5{\cdot}H_2O$ at room temperature with different excitation wavelengths. Adapted with permission [140]. Copyright 2022, published by Wiley-VCH. (B) The frontier molecular orbital energies of the lowest electronic transitions involving the $[SbCl_6]^{3-}$ octahedron upon symmetric percentage of elongation of Sb–Cl. Adapted with permission [142]. Copyright 2024, published by Elsevier. (C) Excitation and emission spectra of $Cs_3ScCl_6{:}Sb^{3+}$ nanocrystals (NCs). Adapted with permission [143]. Copyright 2023, published by Wiley-VCH. (D) Photographic images of white light-emitting diode (LED) of $Cs_3ScCl_6{:}Sb^{3+}$ at different applied currents. Adapted with permission [143]. Copyright 2023, published by Wiley-VCH. (E) Photographic images of fabricated white LED device of $Cs_3LaCl_6{:}Sb^{3+}$ NCs at different applied current fluxes. Adapted with permission [142]. Copyright 2024, published by Elsevier. (F) Photocurrent generated by x-ray irradiation at various dose rates under 30-V bias. Adapted with permission [145]. Copyright 2023, published by American Chemical Society. (G) Linear relationship between signal-to-noise ratio value and x-ray dose rate. Adapted with permission [72]. Copyright 2025, published by Springer. (H) The photograph of the standard line-pair card under the visible light (left) and the corresponding x-ray image of the standard line-pair card (right). Adapted with permission [72]. Copyright 2025, published by Springer.

dopant enables direct ET to yellow-emitting STE states, boosting the PLQY to nearly 100% [140]. Similarly, Sb^{3+} doping in Cs_3ScCl_6 also enhances the luminescence efficiency. A comparative study of Sb^{3+}-doped A_3REX_6 MHPs revealed that structural evolution results in tunable emission (Table 8): Cs_3ScCl_6:Sb^{3+} emits cyan (500 nm) [141], Cs_3YCl_6:Sb^{3+} emits green (545 to 550 nm) [72,142], and Cs_3LaCl_6:Sb^{3+} emits yellow (570 nm) [142]. This PL tunability may originate from the local distortion of the $[SbCl_6]^{3-}$ octahedral in the host lattices (Fig. 9B), which alters the Sb–Cl bond lengths and consequently modulates the energy levels of the frontier molecular orbitals. Intriguingly, Cs_3ScCl_6:Sb^{3+} NCs exhibit white emission under 365-nm excitation (Fig. 9C), attributed to the partial transformation into carbon dots during synthesis. The resulting synergy between broad STE emission and blue emission from carbon dots enables full-spectrum coverage, i.e., white light [143]. Similarly, the white LED based on Cs_3ScCl_6:Sb^{3+} maintains stable white emission under 200 mA, achieving a high CRI (=90) and a luminous efficacy of 23 lm/W (Fig. 9D) [143]. Likewise, the white LED fabricated from Cs_3LaCl_6:Sb^{3+} reaches a CRI of 91 at 25 mA, with brightness further increased at higher currents (Fig. 9E) [142]. Ln^{3+} incorporation enables efficient STE–Ln^{3+} ET for NIR emission; Br^- substitution renders the ET efficiency of $Cs_3La_{0.5}Nd_{0.5}Br_6$ nearly unity and boosts the PLQY of $Cs_3La_{0.17}Nd_{0.83}Br_6$ NCs to 64.65% (after APTN treatment), enabling NIR LEDs with 3.49% EQE and a 488-min T_{50} lifetime [144].

Furthermore, $Rb_2ScCl_5{\cdot}H_2O$:Sb^{3+} exhibits x-ray absorption coefficients comparable to CsI and α-Se, with a radiation sensitivity of 58.5 $\mu C{\cdot}Gy^{-1}{\cdot}cm^{-2}$ (2.9 times higher than commercial α-Se) (Fig. 9F) [145]. Cs_3YCl_6:Sb^{3+} exhibits identical STE emission under x-ray (6.6 mGy/s) as UV excitation, achieving an L.Y. of 16,000 ph/MeV. At an SNR of 3, its detection limit reaches 1.12 μGy/s, far below medical diagnostic thresholds (Fig. 9G). Flexible films of Cs_3YCl_6:Sb^{3+} embedded in polydimethylsiloxane (PDMS) enable high-resolution x-ray imaging, resolving internal structures of adapters, earphones, and circuit boards at dose rate of 1.2 mGy/s, with a spatial resolution up to 9 lp/mm (Fig. 9H) [72].

Compared to ns^2-typed dopants, Ln^{3+} as dopant shows better compatibility with A_3REX_6 MHPs for enhancing PL and RL performance. Replacing Y^{3+} with La^{3+} enlarges the $[LnCl_6]^{3-}$ polyhedra, increasing electron density and inducing greater lattice distortion [142]. This effect is observed in both Ln^{3+} with empty f orbital and Ln^{3+} with f orbital, such as Gd^{3+} and Lu^{3+} [142]. The distortion caused by different Ln^{3+} alters the electronic structure of A_3REX_6, directly impacting its luminescent properties [142,143].

When Ce^{3+} is incorporated as a luminescent center in A_3REX_6 host such as Cs_3ScCl_6, Li_3YCl_6, and Cs_3LaX_6 (X = Cl, Br, and I), dual-shoulder characteristics are observed in the emission peaks of PL and RL spectra within low doping levels, accompanied by rapid decay times (Fig. 10A and B) [58,135,146]. In addition, Cs_3LaCl_6:Ce^{3+} and Cs_3LaBr_6:Ce^{3+} exhibit remarkable thermal quenching resistance, with PL and RL intensities decreasing by less than 25% from 40 to 500 K (Fig. 10C and D). This stability arises from enhanced ET from host-derived STEs to Ce^{3+} ions at elevated temperatures (Fig. 10E) [136]. A similar ET is observed in Cs_3ScCl_6:Ce^{3+} [135], underscoring the critical role of STE-to-activator energy migration in thermal stability.

Notably, Ce^{3+}-doped A_3REX_6 MHPs primarily focus on high-energy scintillation. For instance, Cs_3ScCl_6 achieves optimal scintillation properties at 0.5% Ce^{3+} doping, delivering an L.Y. of 9,200 ph/MeV under 662-keV ^{137}Cs γ-ray excitation (Fig. 10F) [135]. Similarly, Li_3YCl_6 with 1% Ce^{3+} exhibits an L.Y. of 6,185 ph/MeV under identical conditions [146]. High L.Y. and reduced E.R. are observed in Cs_3LaCl_6 and Cs_3LaBr_6 synthesized via the multiple alternating direction melt-mixing and cooling method at elevated doping concentrations. For example, Cs_3LaCl_6:10% Ce^{3+} achieves an L.Y. of 20,000 ph/MeV under 662-keV ^{137}Cs γ-ray excitation, with an E.R. of 9% at 40% Ce^{3+}. Cs_3LaBr_6:10% Ce^{3+} demonstrates even higher performance, reaching 35,000 ph/MeV and 8% E.R. at 40% Ce^{3+} doping [34]. However, crystal quality significantly impacts scintillation metrics. Bridgman-grown Cs_3LaCl_6:8% Ce^{3+} and Cs_3LaBr_6:15% Ce^{3+} show reduced L.Y. (16,000 and 32,500 ph/MeV, respectively) but improved E.R. (8.6% and 4.9%, respectively) (Fig. 10G and H). Remarkably, Bridgman-synthesized Cs_3LaI_6:0.5% Ce^{3+} achieves an exceptional L.Y. of 43,000 ph/MeV (Fig. 10I) [58].

A_3LnX_6 MHPs with f orbitals based on light Ln^{3+}

Light lanthanides (Ln^{3+} = La^{3+}, Ce^{3+}, Pr^{3+}, Nd^{3+}, Sm^{3+}, and Eu^{3+}) with f orbitals, when incorporated B-site luminescent center ions of A_3LnX_6 MHPs, exhibit fundamentally different luminescence and scintillation properties relative to A_3REX_6 MHPs lacking f orbitals. This difference originates from the unfilled $4f^n$ electron configuration of Ln^{3+} ions, which gives rise to characteristic 4f–4f or 5d–4f transitions. In particular,

Table 8. The key PL properties of A_3REX_6 (including PL peak, decay time, and PLQY)

Compound	Sample	PL peak (nm)	Decay time (μs)	PLQY at λ_{ex}	Ref.
Cs_3ScCl_6:Sb^{3+}	NC	545	3.6	32% (λ_{ex} = 345 nm)	[143]
Cs_3ScCl_6:Sb^{3+}	NC	555	–	48% (λ_{ex} = 365 nm)	[143]
Cs_3YCl_6:Sb^{3+}	Powder	550	2.37	93.5% (λ_{ex} = 345 nm)	[72]
Cs_3YCl_6:Sb^{3+}	NC	545	3.9	26% (λ_{ex} = 320 nm)	[142]
Cs_3LaCl_6:Sb^{3+}	NC	570	5.4	30% (λ_{ex} = 320 nm)	[142]
$Cs_3La_{0.17}Nd_{0.83}Br_6$	NC	1,070, 1,350	290	64.65% (λ_{ex} = 405 nm, NIR)	[144]
Cs_3LaI_6:Er^{3+}	NC	1,540	6,670	7.8% (λ_{ex} = 370 nm)	[187]

PL, photoluminescence; NC, nanocrystal; PLQY, PL quantum yield; NIR, near infrared.

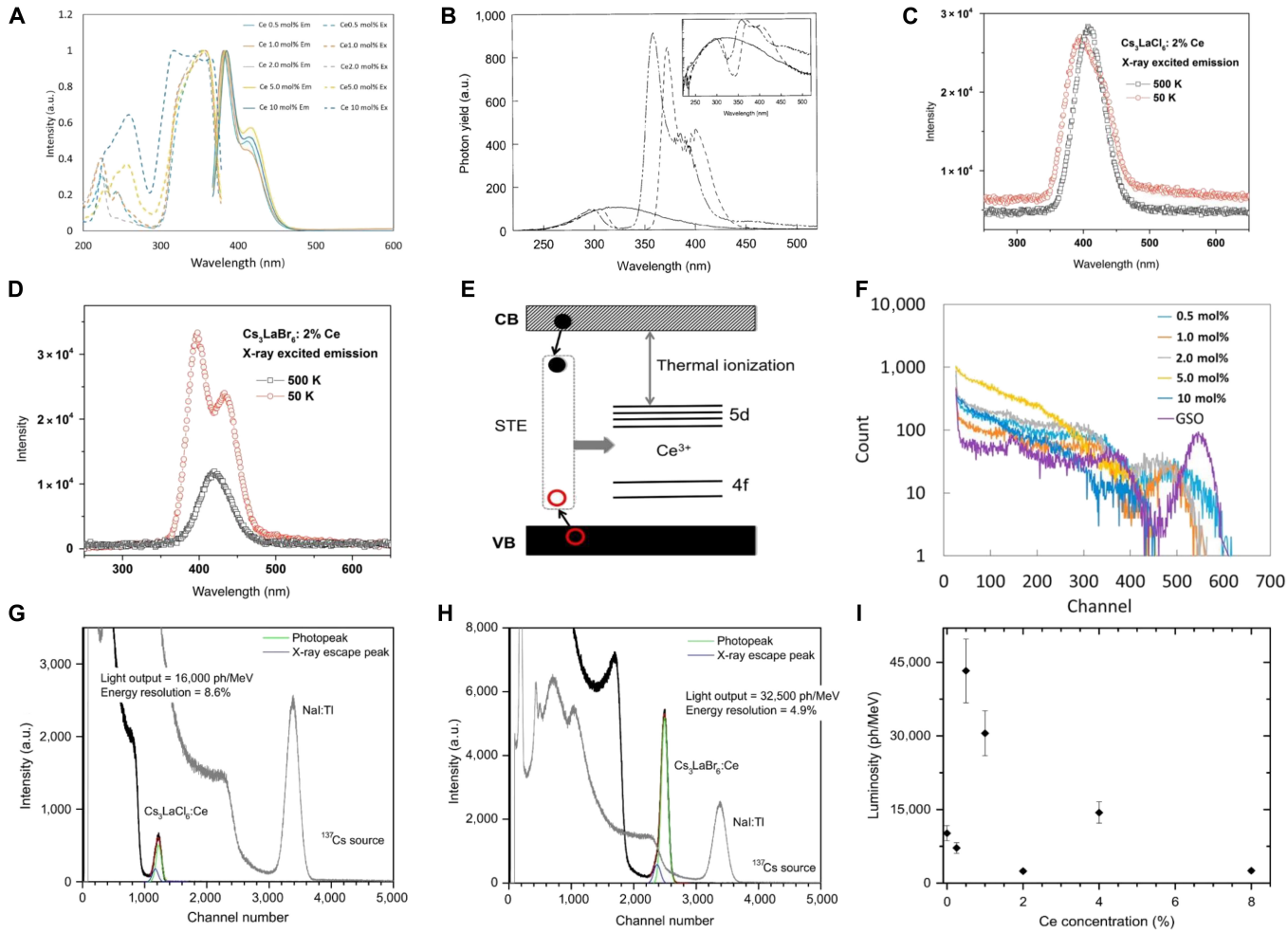


Fig. 10. (A) Photoluminescence (PL) and PL excitation (PLE) spectra of $Cs_3ScCl_6:Ce^{3+}$ crystals. Em, emission; Ex, excitation. Adapted with permission [135]. Copyright 2020, published by Elsevier. (B) X-ray excited emission spectra of pure Cs_2LiYCl_6 (solid line), $Cs_2LiYCl_6:Ce^{3+}$ (dashed line), and $Li_3YCl_6:Ce^{3+}$ (dashed–dotted line), recorded at room temperature. The inset displays the same spectra plotted with a logarithmic *Y* axis. The emission intensity of the 3 crystals was normalized at 300 nm. Adapted with permission [146]. Copyright 1999, published by Elsevier. (C) Radioluminescence (RL) spectra comparison of Cs_3LaCl_6:2% Ce at 50 and 500 K. Adapted with permission [136]. Copyright 2015, published by Elsevier. (D) RL spectra comparison of Cs_3LaBr_6:2% Ce at 50 and 500 K. Adapted with permission [136]. Copyright 2015, published by Elsevier. (E) Scheme of Ce^{3+} emission and excitation. Adapted with permission [136]. Copyright 2015, published by Elsevier. (F) Pulse-height spectra of $Gd_2SiO_5:Ce^{3+}$ (GSO) and $Cs_3ScCl_6:Ce^{3+}$ under ^{137}Cs γ-ray excitation. Adapted with permission [135]. Copyright 2020, published by Elsevier. Pulse height spectrum measured on (G) $Cs_3LaCl_6:Ce^{3+}$ and (H) $Cs_3LaBr_6:Ce^{3+}$ single crystal under ^{137}Cs excitation, respectively. A commercial NaI:Tl crystal is used as the reference. Adapted with permission [58]. Copyright 2014, published by Elsevier. (I) Pulsed x-ray measurements of luminosities for Cs_3LaI_6 containing different Ce concentrations. Adapted with permission [58]. Copyright 2014, published by Elsevier.

Eu^{3+} and Ce^{3+} serve as representative Ln^{3+} emitters (Table 9), whose bright luminescence stems from the strong shielding of the 4f orbitals by the outer $5s^25p^6$ orbitals.

As Eu^{3+} is incorporated as B-site host composition, it tends to undergo partial reduction to Eu^{2+}, resulting in the coexistence of both dual oxidation states within distinct luminescence characteristics. Specifically, Eu^{3+} contributes red emission via f–f transitions, while Eu^{2+} emits blue light through the $4f^7 \rightarrow 4f^65d^1$ transition. Exploiting this duality, Cs_3EuCl_6 NCs exhibit excitation-wavelength-dependent multicolor emission, ranging from red to deep blue [147]. A similar photochromic effect is also observed in Cs_3TbCl_6 (Fig. 11A); both Cs_3EuCl_6 and Cs_3TbCl_6 NCs have been utilized in anticounterfeiting inks, enabling dynamic and multicolor pattern encoding (Fig. 11B) [147]. To further enhance PL properties of Cs_3EuCl_6, constructing ET channels using organic ligands represents another effective strategy [148,149]. For instance, the small molecule ethyl 7-hydroxycoumarin-3-carboxylate (EHC) coordinates with undercoordinated Ln^{3+} through its carbonyl group, passivating surface defects. Furthermore, its singlet excited state exhibits strong spectral overlap with Ln^{3+}'s absorption, significantly boosting the overall ET efficiency [150]. Based on this strategy, EHC-passivated Cs_3EuCl_6 achieves PLQY of 92.4%. The LED devices based on EHC-Cs_3EuCl_6 achieved an EQE of 5.17% and an L_{max} of 370 cd/m^2 (Fig. 11C and D). Notably, the red LED based on EHC-Cs_3EuCl_6 NCs achieved a T_{50} of 440 h at an initial luminance of 100 cd/m^2 [150], outperforming most reported MHP-based LEDs. However, the T_{50} of the EHC-Cs_3EuCl_6 LED remains inferior to commercial LEDs due to defect accumulation, halide migration, interfacial degradation, and thermally activated instability under continuous operation.

The emission of A_3CeX_6 also originates from the parity-allowed 5d–4f transition, resulting in a fully permitted emission in the UV or blue spectral regions with nanosecond-scaled lifetime [73]. According to the CsBr–$CeBr_3$ phase diagram in

Table 9. The key PL properties of A_3LnX_6 (including PL peak, decay time, and PLQY)

Compound	Sample	PL peak (nm)	Decay time (ns)	PLQY at λ_{ex}	Ref.
Cs_3CeCl_6	SC	380, 410	13.61 (2.93%) 40.75 (97.07%)	99.89% (λ_{ex} = 365 nm)	[199]
Cs_3CeBr_6	Powder	392, 421	29.1	80% (λ_{ex} = 365 nm)	[185]
Cs_3CeBr_6	Powder	390, 421	28.33 (390 nm) 28.67 (421)	89.94% (λ_{ex} = 365 nm)	[15]
Cs_3CeBr_6	Powder	391, 421	28.7 (391 nm) 27.1 (425 nm)	92.5% (λ_{ex} = 350 nm)	[73]
Cs_3CeBr_6	SC	395, 425	8.06 (3.06%) 43.53 (96.94%)	92.57% (λ_{ex} = 365 nm)	[199]
Cs_3CeI_6	SC	427, 470	45.44	7.53% (λ_{ex} = 365 nm)	[199]
Cs_3CeI_6	Powder	430, 470	26.1	76.2% (λ_{ex} = 365 nm)	[13]
Rb_3CeI_6	Film	427, 468	22.3 (472 nm) 25 (468 nm)	51% (λ_{ex} = 280 nm)	[186]
Cs_3CeCl_6:Gd^{3+}	NC	376, 408	42.8	96% (λ_{ex} = 365 nm)	[155]
Cs_3EuCl_6	Powder	592, 614	4.35×10^6 (λ_{ex} = 334 nm) 4.11×10^6 (λ_{ex} = 465 nm)	92.4% (λ_{ex} = 365 nm)	[158]
Cs_3EuCl_6	NC	590, 611, 652, 700	3.99×10^6	48.78% (λ_{ex} = 280 nm)	[147]
Cs_3EuCl_6	NC	430	25.79	5.38% (λ_{ex} = 350 nm)	[147]
EHC–Cs_3EuCl_6	NC	617	3.09×10^6	92.4% (λ_{ex} = 365 nm)	[150]

PL, photoluminescence; SC, single crystal; NC, nanocrystal; PLQY, PL quantum yield.

Fig. 11E, the stable phases are limited to Cs_3CeBr_6 and $CsCe_2Br_7$ [73]. As for the PL application, Cs_3CeBr_6 featuring a single Ce^{3+} emissive center, good stability, and few defects compared with $CsCe_2Br_7$ with the dual Ce^{3+} emissive centers (Fig. 11F) [151] exhibits a high PLQY of ~90% and a fast decay time of ~28 ns. Tang et al. fabricated an LED device with Cs_3CeBr_6 as the active layer via a dual-source coevaporation method, achieving an L_{max} of 25 cd/m^2 and an EQE of 0.46% (Fig. 11G), and obtained a white LED by combining it with a yellow $Y_3Al_5O_{12}$:Ce phosphor down-converter (Fig. 11H) [73]. Compared to Cs_3CeBr_6, Cs_3CeI_6 enables spectral tuning by shifting the emission from the UV to deep-blue region (Fig. 12A), which can result in a narrower spectral emission and enhanced color purity in LEDs [13,14]. Density functional theory (DFT) calculations further reveal that Cs_3CeI_6 possesses a higher exciton binding energy (225 meV) than Cs_3CeBr_6 (135 meV) [73,152]. Furthermore, the film fabrication process was optimized; the high-quality, dense, and uniform Cs_3CeI_6 thin films were fabricated using a 5-nm CsCl seed layer and dual-source coevaporation; and the resulting deep-blue LED device (ITO/ZnO/Al_2O_3/Cs_3CeI_6/MCP/TAPC/HAT-CN/Al) achieved an L_{max} of 470 cd/m^2 and an EQE_{max} of 3.5% (Fig. 12B and C) [13]. The luminescence mechanism of Cs_3CeI_6 is driven by ET from STEs of I_2^- species to Ce^{3+}-based Frenkel excitons (CFEs) (Fig. 12D), and increasing STE-CFE spectral overlap with excess CsI could improve ET process, resulting in a deep-blue LED with high L_{max} of 1,075 cd/m^2 and an EQE_{max} of 7.9% (Fig. 12E and F) [14].

The narrowband absorption of Cs_3CeBr_6 enables solar-blind UV detection without requiring additional optical filters, making it highly suitable for UV photodetector applications [15]. In general, Cs_3CeBr_6 films prepared by spin-coating, suffer from high trap-state densities and relatively low carrier mobility, limiting their utility in UV photodetectors. Seok et al. through a postannealing optimization process reduced the trap state density in Cs_3CeBr_6 films to approximately 8×10^{12} cm^{-2}·eV^{-1} while simultaneously increasing the field-effect carrier mobility to about 10 cm^2·V^{-1}·s^{-1}. The UV photodetectors fabricated from the optimized films demonstrated a high responsivity of 2.05 A/W, a detectivity of 1.48×10^{13} Jones (Fig. 13A), and a wide linear dynamic range of 99.64 dB (Fig. 13B). The optimized Cs_3CeBr_6 films as the UV photodetector also exhibited fast response times (rise time, 93 ms; fall time, 345 ms), excellent spectral selectivity, and remarkable stability, retaining ~91% of their initial photocurrent even after 60 d of storage without encapsulation [15]. Similar to Cs_3CeBr_6, Cs_3CeCl_6 features effectively UV absorption and convert it into electrical signals, making its potential for UV photodetectors. While Cl^- substitution of Br^- improves intrinsic thermal stability, the strong polarity of the Ce–Cl bond renders the material prone to oxidation and hydrolysis reactions [153,154]. To address this, Gd^{3+} is introduced into the crystal lattice of Cs_3CeCl_6. On the one hand, the incorporation of Gd^{3+} enhances material stability and improves film compactness, thereby boosting charge transport efficiency. On the other hand, the partial substitution of Ce^{3+} sites by Gd^{3+} increases the interionic distance between Ce^{3+}, suppressing concentration quenching effects, reducing radiative reabsorption, and elevating the PLQY to 96%, which enhances detector sensitivity. Ultimately, the UV photodetector fabricated based on Gd-doped Cs_3CeCl_6:Gd^{3+} thin films demonstrates high detectivity ($7.938 \times$

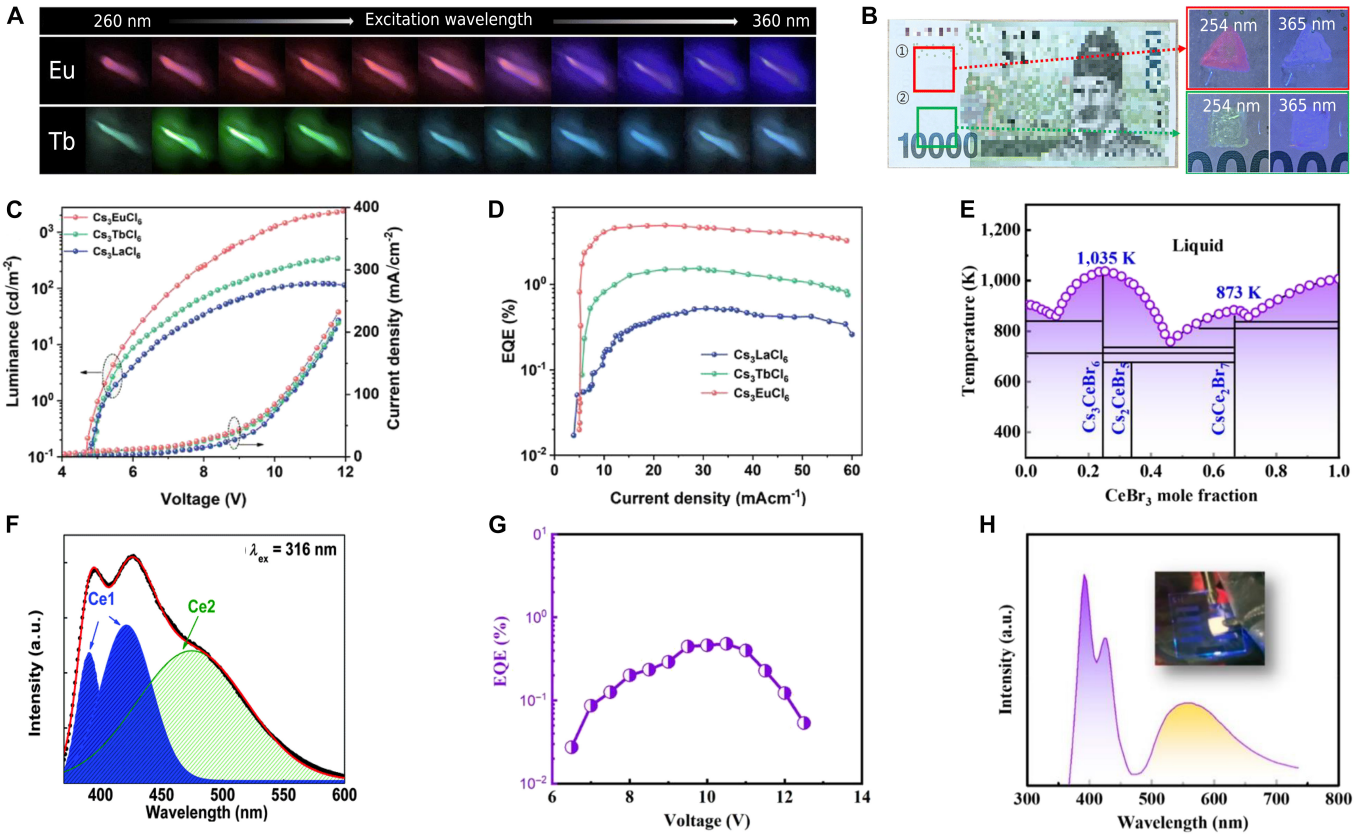


Fig. 11. (A) Photoluminescence (PL) Photographs of Cs_3EuCl_6 and Cs_3TbCl_6 nanocrystal (NC) films under excitation wavelengths from 260 to 360 nm with a 10-nm interval. Adapted with permission [147]. Copyright 2023, published by Royal Society of Chemistry. (B) Photographs of anticounterfeiting marks formed by transfer printing under ambient, 254-nm, and 365-nm ultraviolet (UV) lights. Adapted with permission [147]. Copyright 2023, published by Royal Society of Chemistry. (C) Current density–voltage and luminance–voltage curves. Adapted with permission [150]. Copyright 2024, published by Wiley-VCH. (D) external quantum efficiency (EQE)–current density curves of Cs_3LaCl_6, Cs_3EuCl_6, and Cs_3TbCl_6 light-emitting diode (LEDs). Adapted with permission [150]. Copyright 2024, published by Wiley-VCH. (E) The phase diagrams of $CeBr_3$–CsBr binary system. Adapted with permission [73]. Copyright 2021, published by Royal Society of Chemistry. (F) PL spectra of $CsCe_2Br_7$ single crystals at 38 K. Adapted with permission [151]. Copyright 2015, published by American Chemical Society. (G) The EQE–voltage curve of Cs_3CeBr_6 LED. Adapted with permission [73]. Copyright 2021, published by American Chemical Society. (H) Spectrum of the white LED under forwarding voltage. The inset plot shows the photograph of the white LED device. Adapted with permission [73]. Copyright 2021, published by American Chemical Society.

10^{11} Jones), high responsivity (0.195 A/W) and the dark current densities at 0- and −0.1-V bias voltages are as low as 4.4×10^{-10} and 1.9×10^{-7} A/cm^2, respectively (Fig. 13C and D) [155].

Owing to the excellent x-ray response of Ce^{3+} and Eu^{3+}, A_3CeX_6 and A_3EuX_6 have been explored for x-ray imaging applications [156]. The Cs_3CeCl_6 film achieved a spatial resolution of 11 lp/mm [157], while the Cs_3EuCl_6@PDMS composite film realized a spatial resolution of 9 lp/mm [158]. In addition, $(MTP)_3EuCl_6$ (MTP = methyl(triphenyl)-phosphonium) glass exhibited a spatial resolution of 14.3 lp/mm together with recoverable radiation stability (Fig. 13E) [159].

Beyond its applications in photodetectors, electroluminescent LEDs, and x-ray imaging, the utility of A_3CeX_6 extends to γ-ray scintillation. Under ^{137}Cs γ-ray irradiation, Cs_3CeCl_6 demonstrates an L.Y. of 19,000 ph/MeV and an E.R. of 8.4% [17]. Slow cooling to reduce light-scattering defect concentrations enabled the growth of a large single crystal (Φ10 mm × 30 mm, Fig. 13F), thereby enhancing the L.Y. to 21,000 ph/MeV and lowering the E.R. to 7.6% (Fig. 13G) [160]. However, challenges such as internal stress, insufficient release of crystallization latent heat, and by-product formation persist in the Bridgman method. In contrast, mechanical grinding emerges as an eco-friendly alternative, enhancing luminescent performance and thermal stability while minimizing by-products and chemical waste. Mechanically ground Cs_3CeCl_6, Cs_3TbCl_6, and Cs_3EuCl_6 powders exhibit x-ray-induced quantum tunneling effects, where high-energy ionizing radiation facilitates electron tunneling between trap states and the conduction band [161]. The hydrated phase $Cs_3CeCl_6{\cdot}3H_2O$ was also synthesized, which preserves the excellent scintillation performance of Cs_3CeCl_6 while benefiting enhanced properties due to water incorporation. Under x-ray irradiation, it achieves a high L.Y. of 31,900 ph/MeV, surpassing commercial LuAG:Ce. It exhibits a LoD as low as 108 nGy/s and a spatial resolution of 12 lp/mm, making it suitable for high-resolution imaging applications [162]. As similar as nanosecond-scaled decay time with Cs_3CeCl_6, Cs_3PrCl_6 exhibits the $4f^15d^1 \rightarrow 4f^2$ transition with fast scintillating decay time (11.7 ns [53%] and 72 ns [47%]) (Fig. 13H) and L.Y. of 5,900 ph/MeV under ^{137}Cs γ-ray excitation (Fig. 13I) [163]. As expected, Cs_3CeCl_6 and Cs_3PrCl_6 are promising scintillators as radiation detectors in time-of-flight positron emission tomography.

A_3LnX_6 MHPs with f orbitals based on heavy Ln^{3+}

Although some medium-heavy Ln^{3+} possess electrons in their f orbitals, A_3LnX_6 MHPs still exhibit both intrinsic luminescence

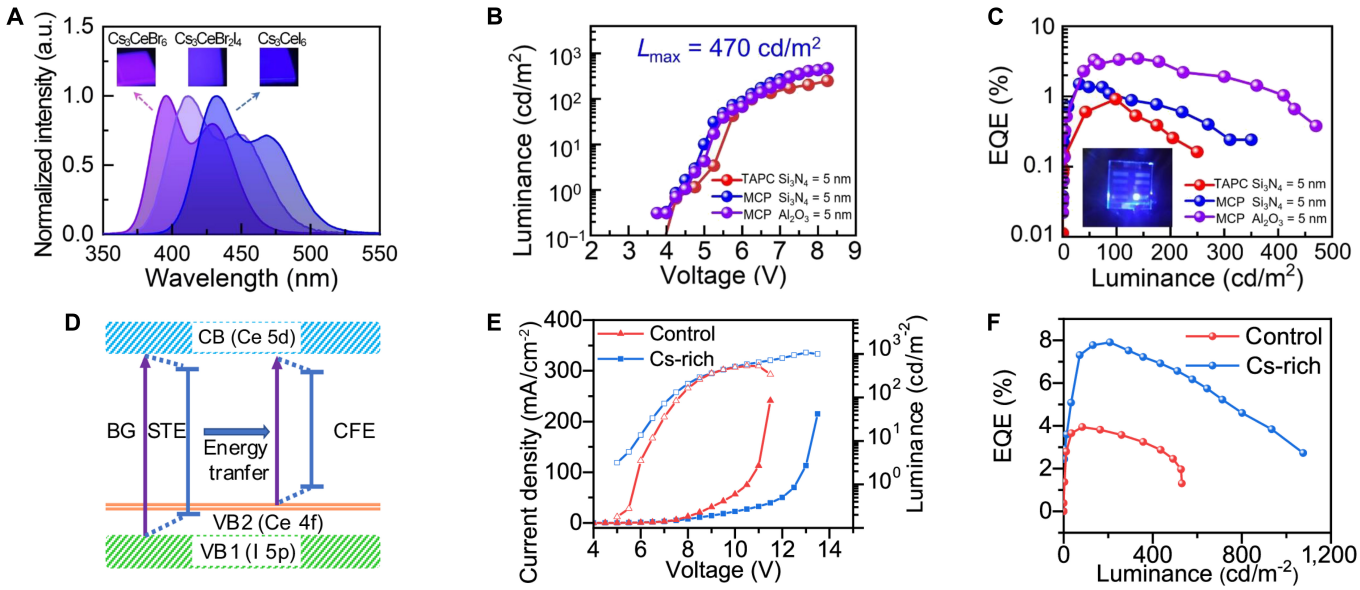


Fig. 12. (A) Photoluminescence (PL) spectra of Cs_3CeBr_6, $Cs_3CeBr_2I_4$, and Cs_3CeI_6, with the inset showing the corresponding photographs under ultraviolet (UV) light radiation. Adapted with permission [13]. Copyright 2022, published by American Association for the Advancement of Science. (B) Voltage–luminance curves of Cs_3CeI_6 light-emitting diode (LEDs). Adapted with permission [13]. Copyright 2022, published by American Association for the Advancement of Science. (C) External quantum efficiency (EQE)–luminance curves of Cs_3CeI_6 LEDs. Adapted with permission [13]. Copyright 2022, published by American Association for the Advancement of Science. (D) Schematic diagram of Cs_3CeI_6 energy band structure and 2 types of excitons. Adapted with permission [14]. Copyright 2024, published by Springer Nature. (E) EQE–luminance curve of Cs_3CeI_6 control and Cs-rich devices. Adapted with permission [14]. Copyright 2024, published by Springer Nature. (F) Current density–voltage–luminance curve of Cs_3CeI_6 control and Cs-rich devices. Adapted with permission [14]. Copyright 2024, published by Springer Nature.

and characteristic f–f or d–f transition. In general, Gd^{3+}, Tm^{3+}, and Yb^{3+} are utilized as B-site host composition, the PLQY of Cs_3GdCl_6 NCs, Cs_3TmCl_6 NCs, and Cs_3YbCl_6 NCs after oleic acid passivation is 30.3%, 22.8%, and 59.8%, respectively, attributed to intrinsic STE emission [27,139]. Herein, the white LED based on Cs_3TmCl_6 shows a CRI of 87.0, a CCT of 5,283 K (Fig. 14A), and a T_{50} of 336 h (Fig. 14B), surpassing the T_{50} reported in prior studies [27].

In A_3LnX_6, the incorporation of ns^2-typed Sb^{3+} dopant induces local Jahn–Teller distortions owing to the low-symmetry coordination environment, thereby enhancing STE emission [164]. The extent of distortion depends on the specific B-site host composition. For example, Cs_3GdCl_6:Sb^{3+}, Cs_3YbCl_6:Sb^{3+}, and Cs_3LuCl_6:Sb^{3+} emits at ~545 nm [22,142], 533 nm [165], and 525 nm [166], respectively, and their PLQY could increase to 96.3%, 66.9%, and 99% (Table 10) [22,165,166]. The white LED based on Cs_3GdCl_6:Sb^{3+} exhibits a high CRI of 96.5 (Fig. 14C). Furthermore, excellent thermal quenching resistance enable the long-term operation of white LED (Fig. 14D) [22]. Meanwhile, the white LED based on Cs_3LuCl_6:Sb^{3+} exhibits excellent color quality, with a high CRI of 94 and a CCT of 5,565 K, and also shows strong resistance to thermal quenching [166]. Interestingly, Cs_3YbCl_6:Sb^{3+} allowed a reversible transformation to $Cs_2YbCl_5{\cdot}H_2O$:Sb^{3+}, which is analogous to transformation from Cs_3InCl_6:Sb^{3+} to $Cs_2InCl_5{\cdot}H_2O$:Sb^{3+} [87,165]. The water-driven strategy would be triggered rapidly after exposure to methanol (within 15 s), accompanying with an emission color change from yellow to green (Fig. 14E) [165]. This stimulus-responsive luminescence switching reveals the potential of information encryption as the former turns green, while the latter remains yellow [165]. Moreover, Cs_3LuCl_6:Sb^{3+} delivers 7,300 ph/MeV and a LoD of 0.4 μGy/s, with flexible films achieving a spatial resolution of 11.5 lp/mm [167]. A $Cs_2NaLuCl_6$:Sb^{3+}/Cs_3LuCl_6:Sb^{3+} heterojunction enhances RL to 2.4× BGO and lowers the detection limit to 140 nGy/s and a spatial resolution of 14 lp/mm, while Mn^{2+} incorporation enables trichromatic emission for color x-ray imaging [69]

Beyond the intrinsic luminescence, Ln^{3+} as B-site host and dopant enables the tunable emission with ET process, based on the characteristic f–f or d–f transitions (Fig. 15A) [19,168,169]. Under x-ray excitation, 0.5-in Cs_3GdCl_6:Ce^{3+} and Cs_3GdBr_6:Ce^{3+} exhibit the L.Y. of 40,000 and 48,000 ph/MeV, respectively (Fig. 14F). When excited by ^{137}Cs γ-ray, their L.Y. reaches 24,500 and 47,000 ph/MeV, with E.R. of 4.5% and 4.0%, respectively (Fig. 14G and H). Relatively, Cs_3GdBr_6:Ce^{3+} delivers the highest L.Y. and lowest E.R. reported among A_3BX_6 MHPs under ^{137}Cs γ-ray excitation [32]. Cs_3TbCl_6:Sb^{3+} NCs achieved an L.Y. of 20,300 ph/MeV, a reduced detection limit of 212 nGy/s (Fig. 15B), and an improved spatial resolution of 9.6 lp/mm (Fig. 15C). They further enabled high-contrast imaging of circuit features across a wide range of irradiation doses [16].

Although ET process toward Ln^{3+} to Ln^{3+} is environmentally insensitive, it mainly involves quadrupole–quadrupole [170], $Cs_3Tb_{0.5}Ce_{0.5}Cl_6$ establishes an efficient ET pathway of $Ce^{3+} \rightarrow Tb^{3+}$ channel (Fig. 15D), suppressing nonradiative recombination and achieving a PLQY of up to 86%. The white LED based on $Cs_3Tb_{0.5}Ce_{0.5}Cl_6$ exhibited a CRI of ~78 and a light efficiency of ~118 lm/W at 25 mA (Fig. 15E) [171]. In addition to Ce^{3+}-sensitized dopant, A_3TbF_6:Eu^{3+} (A = Cs and Rb) demonstrates stimulus-responsive luminescence based on humidity-induced phase transitions. Initially, weak orbital coupling between Eu^{3+} and Tb^{3+} results in low ET efficiency, with dominant green emission from Tb^{3+}. Upon exposure to a humid environment, the material undergoes a phase transition to A_2TbF_5:Eu^{3+}, where shortening interionic distance and triggering efficient energy coupling between Tb^{3+} and Eu^{3+} activate the ET process and characteristic Eu^{3+} red emission (Fig. 15F) [168,169].

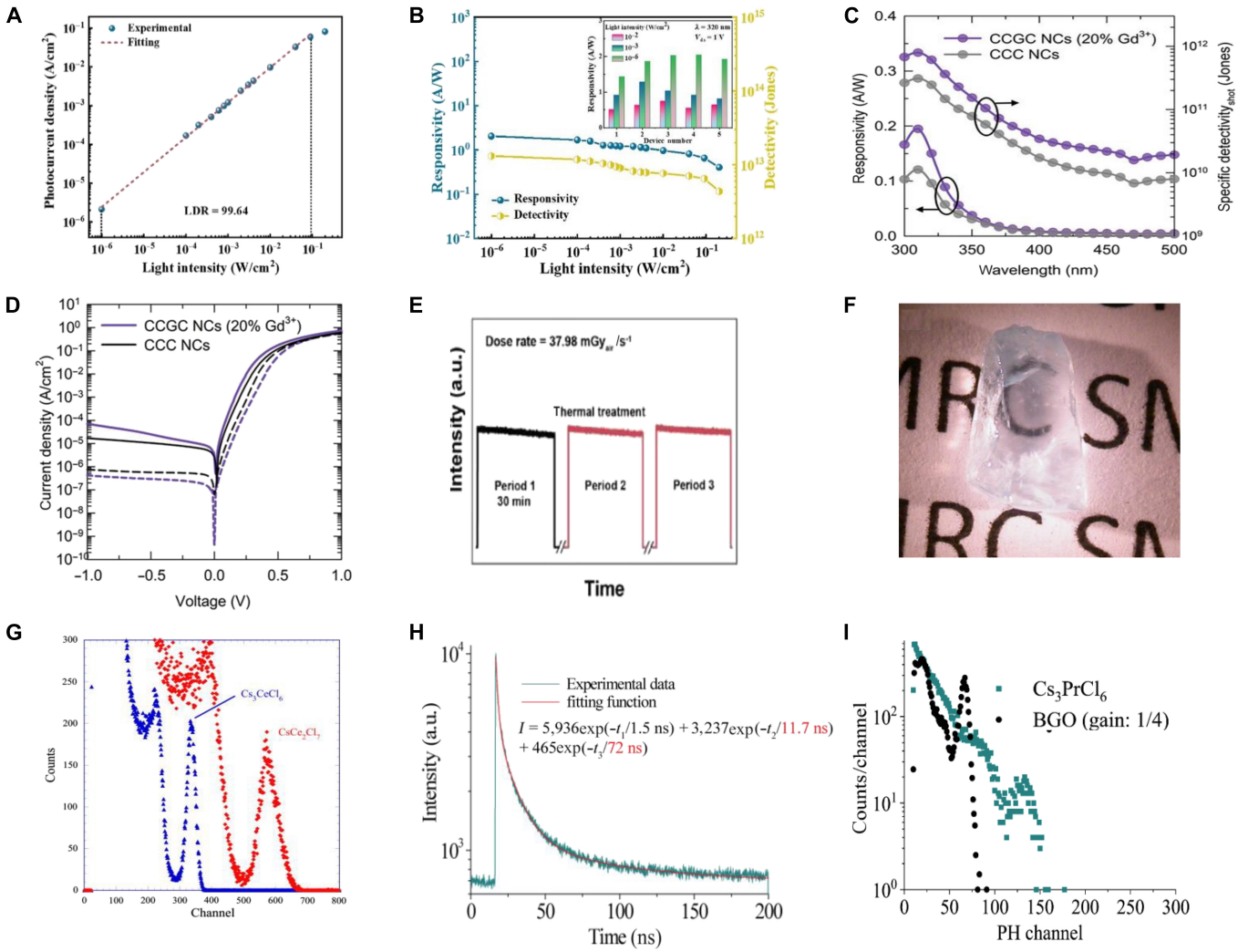


Fig. 13. (A) The logarithmic curve of light-intensity-dependent photocurrent density and corresponding power law fit curve under 320-nm light illumination. LDR, linear dynamic range. Adapted with permission [15]. Copyright 2024, published by Elsevier. (B) Responsivity and detectivity of the optimum photodetector versus the light intensity. Adapted with permission [15]. Copyright 2024, published by Elsevier. (C) Spectral responsivity and specific detectivity of 0% and 20% Gd^{3+}-alloyed CCGC photodetector. Adapted with permission [155]. Copyright 2024, published by Wiley-VCH. (D) *J*–*V* curves of 0% and 20% Gd^{3+}-alloyed CCGC photodetector in illumination (310 nm) in solid line and dark conditions in dashed line. Adapted with permission [155]. Copyright 2024, published by Wiley-VCH. (E) Radioluminescence intensity of the $(MTP)_3EuCl_6$ glass after high-dose irradiation, followed by heating at 150 °C for 1 h to restore scintillation performance. Adapted with permission [159]. Copyright 2025, published by Wiley-VCH. (F) Image of a polished slice of Cs_3CeCl_6 showing good transparency needed for efficient light emission. Adapted with permission [160]. Copyright 2013, published by Institute of Electrical and Electronics Engineers. (G) Pulse-height spectra of Cs_3CeCl_6 single crystals under excitation from 662-keV photons from a ^{137}Cs source. Adapted with permission [160]. Copyright 2013, published by Institute of Electrical and Electronics Engineers. (H) Pulsed x-ray-excited scintillation decay time profile of Cs_3PrCl_6. Adapted with permission [163]. Copyright 2022, published by M Y U Scientific Publishing Division. (I) ^{137}Cs γ-ray induced scintillation pulse height spectra of the Cs_3PrCl_6 and a reference $Bi_4Ge_3O_{12}$ (BGO) crystal. Adapted with permission [163]. PH, pulse height. Copyright 2022, published by M Y U Scientific Publishing Division.

Screen-printed patterns utilizing differently doped Cs_3TbF_6 crystals have been developed for information encryption, where concealed multicolor graphics become visible only under specific stimulus conditions (Fig. 15G) [169]. Furthermore, beyond their kinetically tunable hydrochromic luminescence properties, Rb_3TbF_6:Eu^{3+} crystals also exhibit excitation-wavelength-dependent luminescence phenomena, attributed to the unique light absorption of Eu^{3+} at 393 nm. Leveraging this phenomenon, 4 distinct sample sets can generate varying arrays of color combinations depending on the excitation/stimulus conditions. These combinations can serve as identification codes for encryption (Fig. 15H) [168].

As one of the high-efficiency scintillator, A_3TbCl_6 (A = Cs and Rb) exhibits similar excited-state relaxation pathways under both low- and high-energy excitations [161]. The scintillation properties of A_3TbCl_6 are dependent on its structural form (e.g., polycrystalline, microcrystalline, or glass), which, in turn, is dictated by the synthesis route. The performance divergence between polycrystal and microcrystal forms is largely dictated by variations in grain size, orientation, grain boundary density, and film compactness. Benefiting from large grain sizes, Cs_3TbCl_6 and Rb_3TbCl_6 polycrystals achieve impressive L.Y. of 56,800 and 88,800 ph/MeV, respectively, with LoD of 149.65 and 115.38 nGy/s (Fig. 16A) under x-ray excitation. The spatial resolution of Cs_3TbCl_6 and Rb_3TbCl_6 polycrystals films reach 3.3 and 3.9 lp/mm, respectively (Fig. 16B) [31]. Although the reduced grain size of RT recrystallized Cs_3TbCl_6 microcrystals led to a lower L.Y. of 51,800 ph/MeV, this refinement in microstructure enabled the fabrication of a denser, more uniform film. This resulted in a significantly improved spatial resolution

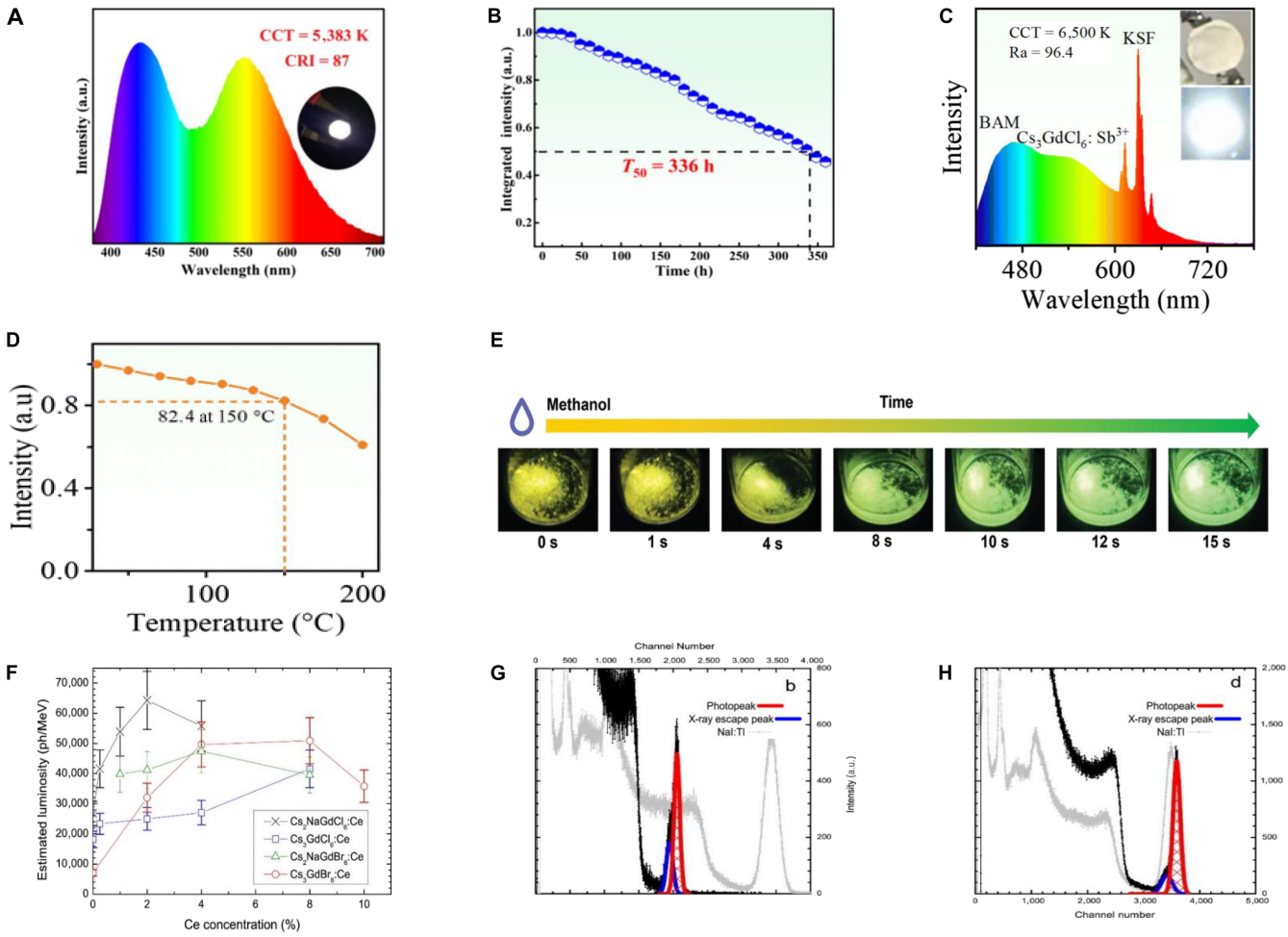


Fig. 14. (A) Photoluminescence (PL) spectrum of the fabricated white light-emitting diode (LED) prepared by Cs_3TmCl_6. Adapted with permission [27]. Copyright 2024, published by American Chemical Society. (B) Long-term running test showing the T_{50} of the white LED. Adapted with permission [27]. Copyright 2024, published by American Chemical Society. (C) Emission spectrum of the white LED device fabricated by blending the yellowish-emitting Cs_3GdCl_6:1.0% Sb^{3+} powder with the commercial $BaMgAl_{10}O_{17}:Eu^{2+}$ and $K_2SiF_6:Mn^{4+}$ on a 365-nm chip. Adapted with permission [22]. Copyright 2024, published by Royal Society of Chemistry. (D) Integrated PL intensities of the $Cs_3GdCl_6:Sb^{3+}$ MCs as a function of temperature. Adapted with permission [22]. Copyright 2024, published by Royal Society of Chemistry. (E) The in situ dynamic emission color transformation of $Cs_2YbCl_5·H_2O:Sb^{3+}$ to $Cs_3YbCl_6:Sb^{3+}$ by methanol. Adapted with permission [165]. Copyright 2024, published by Wiley-VCH. (F) Estimated luminosity of polycrystalline samples ($Cs_2NaGdCl_6:Ce^{3+}$, $Cs_3GdCl_6:Ce^{3+}$, $Cs_2NaGdBr_6:Ce^{3+}$, and $Cs_3GdBr_6:Ce^{3+}$) under x-ray irradiation versus Ce concentration. Adapted with permission [32]. Copyright 2014, published by Elsevier. (G and H) γ-Ray pulse height spectra of $Cs_3GdCl_6:Ce^{3+}$ and $Cs_3GdBr_6:Ce^{3+}$, respectively. Adapted with permission [32]. Copyright 2014, published by Elsevier.

of 12 lp/mm and a lower LoD of 63 nGy/s (Fig. 16C and D) [83]. In addition, the glass scintillator prepared by substituting Cs^+ with organic groups (e.g., $Bzmim^+$), although resulting in a decrease in L.Y., the high transmittance of the glass has achieved a high spatial resolution of 25 lp/mm (Fig. 16E and F) [172]. In general, polycrystals typically achieve high L.Y.s owing to their large grain size; microcrystals facilitate the fabrication of dense films, leading to a low detection limit; and highly transparent glasses offer high spatial resolution. Introducing emissive fluorophores to construct ET channels with Ln^{3+} enhances radiative performance, as exemplified by $(BuTPP)_3TbCl_6$ (BuTPP = butyltriphenylphosphonium) glass achieving 8,100 ph/MeV of L.Y., 0.93 μGy/s of LoD, and 26.8 lp/mm of spatial resolution [173].

Machine Learning for A_3BX_6 MHPs with Enhanced Radiative Transitions

Exploring the broad compositional landscape of A_3BX_6 perovskites remains challenging using conventional approaches, this is mainly reflected in long experimental cycles, high material costs, and limited reproducibility, motivating the introduction of machine learning (ML) as an efficient tool for high-throughput prediction and guided synthesis. Im et al. [174] demonstrated this potential by constructing a 1,703-composition Cs-B-X library and using crystal graph convolutional neural networks to learn structural features, ultimately identifying 40 thermodynamically stable compounds (Fig. 17A). Among them, 27 have been experimentally verified, while several other experimentally confirmed that stable compounds were not captured by the ML predictions.

Such structural stability mapping is particularly relevant for scintillators, as the accessible compositional phase space constrains the formation of thermodynamically stable hosts and helps preselect candidates with favorable electronic and optical properties, such as bandgap width. Building on this foundation, ML can act as a "virtual experimentalist" by learning quantitative correlations between host structures and photophysical properties, enabling the rapid evaluation of thousands of candidate materials prior to synthesis (Fig. 17B) [175].

Table 10. The key PL properties of A_3LnX_6 (including PL peak, FWHM, Stokes shift, decay time and PLQY)

Compound	Sample	PL peak (nm)	FWHM (nm)	Stokes shift (nm)	Decay time	PLQY at λ_{ex}	Ref.
Cs_3TbCl_6	Powder	547	–	–	6.8 ms	90.8% (λ_{ex} = 280 nm)	[83]
Cs_3DyI_6	NC	488, 574, 660, 1,540	92	118	–	–	[187]
Cs_3TmCl_6	NC	440	88	70	1.5 ns (76.6%) 7.1 ns (23.4%)	22.8% (λ_{ex} = 370 nm)	[27]
Cs_3YbCl_6	NC	429	–	–	1–2 ns (93%) 8–9 ns (7%)	89.3% (λ_{ex} = 355 nm)	[139]
$Cs_3GdCl_6:Sb^{3+}$	NC	550	–	–	4.1 μs	28% (λ_{ex} = 320 nm)	[142]
$Cs_3GdCl_6:Sb^{3+}$	Powder	540	120	–	2.96 μs	96.3% (λ_{ex} = 330 nm)	[22]
$Cs_3TbCl_6:Sb^{3+}$	NC	450, 489, 548, 621, 700	8.6	225	7.6 ms	48.18% (λ_{ex} = 280 nm)	[16]
$Cs_3Tb_{0.1}Ce_{0.9}Cl_6$	NC	470, 405, 546	–	–	33.04 ns (405 nm)	86% (λ_{ex} = 290 nm)	[171]
$Cs_3DyI_6:Er^{3+}$	NC	488, 574, 660, 1,540	–	–	9.7 ns	87.4% (λ_{ex} = 370 nm)	[187]
$Cs_3YbCl_6:Sb^{3+}$	SC	533	120	206	1.66 μs	66.9% (λ_{ex} = 365 nm)	[165]
$Cs_3LuCl_6:Sb^{3+}$	NC	525	–	–	2.8 μs	13% (λ_{ex} = 320 nm)	[142]
$Cs_3LuCl_6:Sb^{3+}$	NC	531	104	191	1.96 μs	92% (λ_{ex} = 340 nm)	[167]
$Cs_3LuCl_6:Sb^{3+}$	Powder	380, 420	–	30, 70	33.76 ns (380 nm) 34.11 ns (420 nm)	82.02% (λ_{ex} = 350 nm)	[188]
$Cs_3LuCl_6:Ce^{3+}$	Powder	382	57	42	26.6 ns	6% (λ_{ex} = 335 nm)	[189]
$Cs_3LuCl_6:Tb^{3+}$	Powder	549	12	275	–	62% (λ_{ex} = 335 nm)	[189]
$Cs_3LuCl_6:Ce^{3+}$, Sm^{3+}	Powder	379	26	39	18.7 ns	5% (λ_{ex} = 335 nm)	[189]

PL, photoluminescence; SC, single crystal; NC, nanocrystal; PLQY, PL quantum yield; FWHM, full width at half maximum.

For scintillators, the fundamental L.Y. can be approximated as the product of 3 constituent processes: absorption, ET, and luminescence Eq. (13) [176]:

$$\text{L. Y.} = \frac{E_\gamma}{\beta E_g} \cdot \eta_2 \cdot \eta_3 \tag{13}$$

where E_g is the bandgap of scintillators, E_γ is the energy of the incident radiation, and η_2 and η_3 are the efficiencies of ET and intracenter luminescence, respectively. Herein, the E_g can be efficiently computed from electronic structure calculations, serving as a physically meaningful descriptor for ML-based prediction of L.Y. (Fig. 17C).

Beyond E_g, the overall L.Y. also depends on the carrier recombination efficiency, which is governed by the interplay between the thermalization length and the Onsager radius (R_{Ons}). R_{Ons} represents the distance at which the Coulomb potential between an electron and hole equals the thermal energy and can be expressed as Eq. (14) [177]:

$$R_{Ons} = \frac{e^2}{4\pi\varepsilon_0\varepsilon_r k_B T} \tag{14}$$

where e is the elementary charge, k_B is the Boltzmann constant, ε_0 is the permittivity of free space, T is the absolute temperature, and ε_r is the relative dielectric constant of the host (including both ionic and electronic contributions). Thermalized carriers separated by a distance r recombine with probability $1 - \exp(-R_{Ons}/r)$ or escape with probability $\exp(-R_{Ons}/r)$. Therefore, R_{Ons} and ε_r directly influence electron–hole recombination and serve as key descriptors for ML prediction of L.Y. at RT.

Together, Pilania et al. [176] investigated a set of 25 Eu^{2+}- and Ce^{3+}-doped scintillators by computing bandgaps, densities, and both ionic and electronic contributions to the dielectric constant using DFT. ML models based on Kernel Ridge Regression and AdaBoost were then trained to predict L.Y. and scintillation performance. Their results show that both a smaller E_g and a lower ionic contribution to ε_r tend to achieve higher L.Y. (Fig. 17D and E) [176].

Although ML methods have shown great potential in predicting the properties of perovskite materials, their practical application still faces several limitations. On the one hand, compared with datasets in bioinformatics or genomic prediction that often contain tens of thousands of entries, the datasets currently available for perovskite structure and property prediction remain relatively small, and the descriptors used to characterize luminescence performance are still limited. On the other hand, light emission is fundamentally governed by excited-state carrier dynamics and electron–phonon coupling, which cannot be fully captured by ground-state DFT descriptors. Consequently, predicting luminescence properties solely

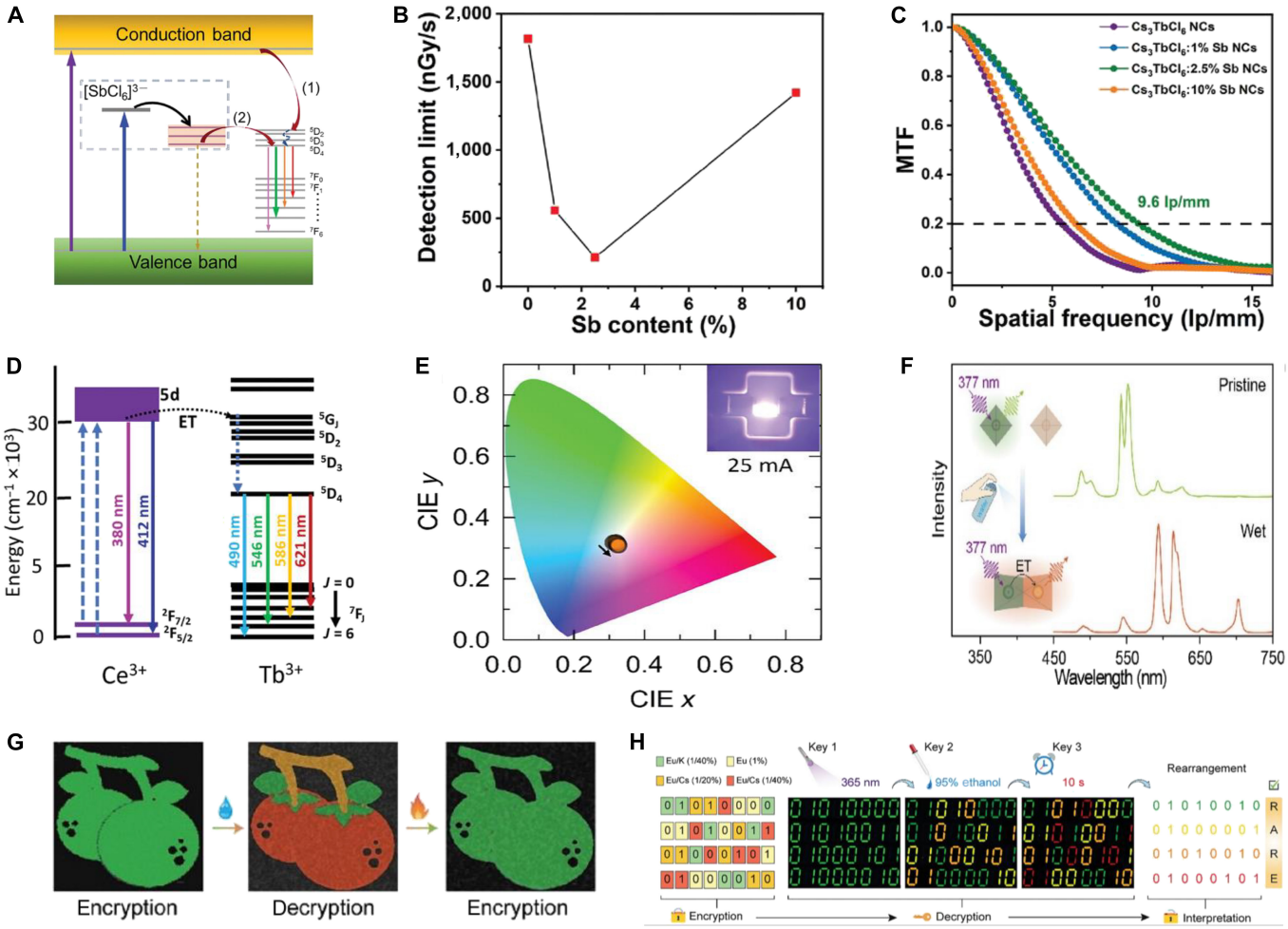


Fig. 15. (A) The charge–carrier dynamics model and photophysical processes of Cs_3TbCl_6:Sb^{3+} nanocrystals (NCs). (1) Transfer process assisted by Cl^--Tb^{3+} charge transition in $[TbCl_6]^{3-}$; (2) thermally boosting energy transfer (ET) assisted by $[SbCl_6]^{3-}$-induced self-trapped exciton (STE) state. Adapted with permission [16]. Copyright 2024, published by Wiley-VCH. (B) The variation of detection limit of Cs_3TbCl_6:Sb^{3+} NCs as a function of Sb/Tb ratio. Adapted with permission [16]. Copyright 2024, published by Wiley-VCH. (C) Modulation transfer function (MTF) of x-ray images from undoped and Sb^{3+}-doped Cs_3TbCl_6 NCs. Adapted with permission [16]. Copyright 2024, published by Wiley-VCH. (D) Ce^{3+} to Tb^{3+} ET process in $Cs_3Tb_xCe_{1-x}Cl_6$ alloy NCs. Adapted with permission [171]. Copyright 2024, published by Wiley-VCH. (E) Commission Internationale de l'Éclairage (CIE) coordinate of white light-emitting diode (LED) based on $Cs_3Tb_{0.5}Ce_{0.5}Cl_6$. Adapted with permission [142]. Copyright 2024, published by Wiley-VCH. (F) Emission spectra of Cs_3TbF_6:Eu^{3+} crystals before and after water treatment. Adapted with permission [169]. Copyright 2022, published by American Chemical Society. (G) Luminescence photographs of the orange pattern under 365-nm ultraviolet (UV) lamp excitation in a wetting–drying cycle. Adapted with permission [169]. Copyright 2022, published by American Chemical Society. (H) The encryption of ACSII binary codes and decryption process. Adapted with permission [168]. Copyright 2024, published by Wiley-VCH.

based on ground-state DFT parameters has intrinsic limitations. Notably, recent studies have shown that methods such as time-dependent DFT, GW–Bethe–Salpeter equation method, and surface hopping can more effectively describe the excited-state properties of materials [178–180].

Conclusion and Prospects

A_3BX_6 MHPs feature tunable electronic structures, highly tolerant crystal lattices, and functional charge carriers generated under optical or electrical excitation, which endow them with broad application prospects in optoelectronic and scintillation applications. This review summarizes recent progress in A_3BX_6 MHPs (A_3SbX_6, A_3InX_6, A_3BiX_6, A_3REX_6, and A_3LnX_6) with a focus on B-site dopant engineering and its influence on radiative transition mechanisms. B-site cation engineering effectively modulates the electronic structures and luminescence pathways in these materials. Specifically, ns^2-typed dopant induce STE emission, while transition-metal and RE dopants activate characteristic d–d, d–f, and f–f transitions, enabling tunable PL and EL. In addition to conventional light emission applications, A_3BX_6 MHPs also exhibit excellent performance in x-ray and γ-ray detection, owing to their strong high-energy photon absorption, low self-absorption, and broad spectral response.

Despite their tunable luminescence and enhanced scintillation performance, the practical development of A_3BX_6 MHPs continues to face substantial challenges and opportunities, including but not limited to the following:

1. The high CRI of A_3BX_6 MHPs is advantageous for white-light LED applications; however, the inherently broad emission spectra limit the achievable color purity for narrowband or monochromatic LEDs. In addition, the relatively low PLQY in the NIR spectral region may constrain their performance in bioimaging, NIR sensing, and other NIR photonic applications.
2. Although the EQE of deep-blue A_3BX_6 LEDs reaches 7.9%, which is relatively high for this challenging spectral

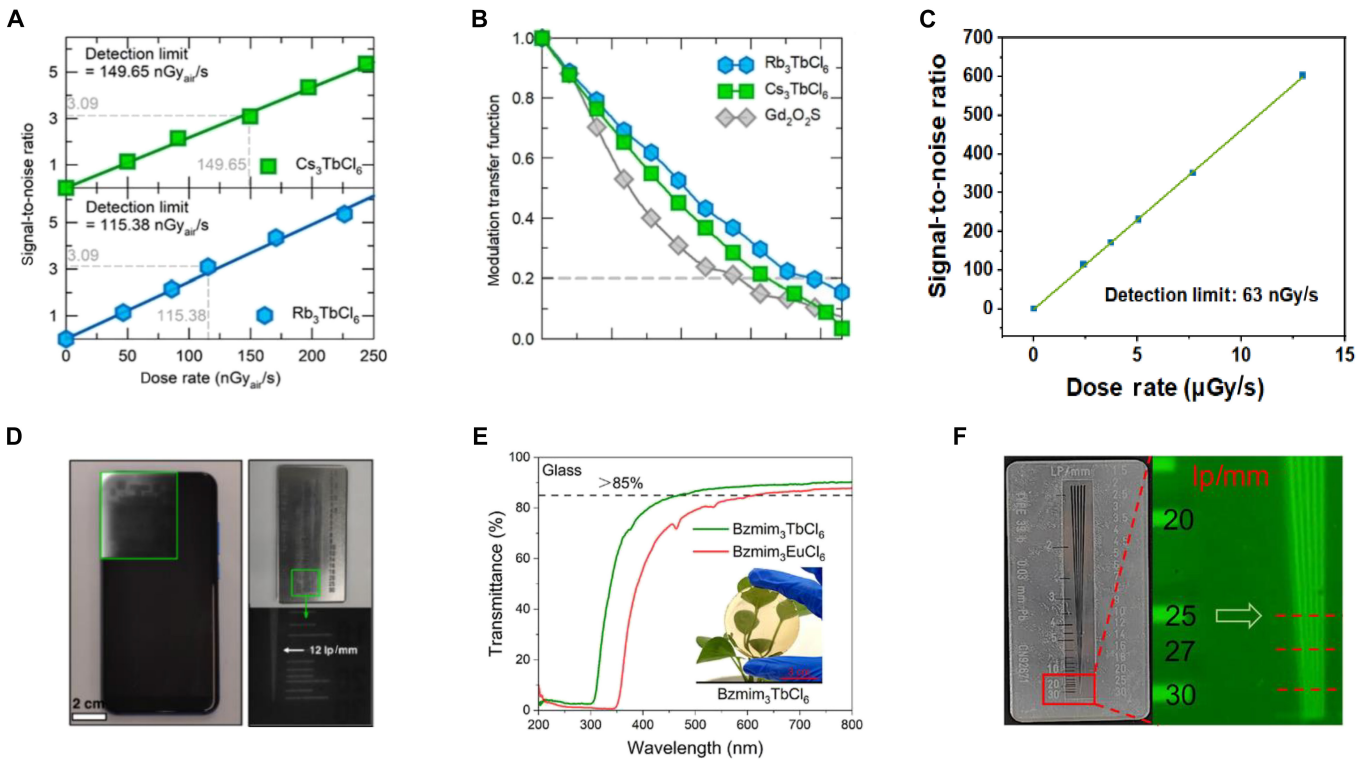


Fig. 16. (A) The linear response between radioluminescence (RL) intensity and x-ray dose rate of Cs_3TbCl_6 and Rb_3TbCl_6 under low-dose-rate excitation. Their detection limits can be defined, as the signal-to-noise ratio (SNR) is 3. Adapted with permission [31]. Copyright 2022, published by American Chemical Society. (B) Spatial resolution measurement of Cs_3TbCl_6, Rb_3TbCl_6, and Gd_2O_2S scintillator films. Adapted with permission [31]. Copyright 2022, published by American Chemical Society. (C) The linear relationship between SNR value of Cs_3TbCl_6 and x-ray dose rate. Adapted with permission [83]. Copyright 2025, published by Springer. (D) The photograph of a smartphone (left) the standard line-pair card under the visible light (top) and the corresponding x-ray image of the standard line-pair card (bottom). Adapted with permission [83]. Copyright 2025, published by Springer. (E) Transmission spectra of $Bzmim_3LnCl_6$ glass. Adapted with permission [172]. Copyright 2025, published by Wiley-VCH. (F) Spatial resolution of the $Bzmim_3TbCl_6$ glass scintillation demonstrated using a line pair card. Adapted with permission [172]. Copyright 2025, published by Wiley-VCH.

region, the EQE of green and red LEDs remains below the reported records, indicating that further optimization of charge carrier injection, recombination efficiency, and material stability is required.

3. In the field of x-ray scintillators, RE A_3BX_6 MHPs are promising candidates for high-resolution x-ray imaging due to their high L.Y. (maximum L.Y. = 88,800 ph/MeV), low detection limit (minimum LoD = 63 nGy/s), and high spatial resolution (highest spatial frequency = 18.5 lp/mm). However, current studies predominantly report NCs or submillimeter-sized single crystals, which critically influences edge emission, photon escape, suboptimal light coupling, and reduced optical transmittance, thereby limiting the overall scintillation performance. To address this, further advances in crystal growth techniques and scalable strategies for producing centimeter-scale single crystals are essential to obtain the superior scintillation properties.
4. In the field of γ-ray scintillators, RE A_3BX_6 MHPs have demonstrated considerable promise owing to their high L.Y. (maximum L.Y. = 47,000 ph/MeV) and low E.R. (minimum E.R. = 4.0%). However, these values remain inferior to those of state-of-the-art scintillators such as $LaBr_3$:Ce, which exhibits an L.Y. of 74,196 ph/MeV and an E.R. of ~3% at 662 keV [181]. In general, the high scintillation performance of A_3BX_6 MHPs has been mainly achieved by Ce^{3+} doping. However, the characteristic energy levels of Ce^{3+} limit further optimization of L.Y. and decay-time, hindering time-critical applications such as time-of-flight position emission tomography. Future studies should explore multicomponent doping or codoping strategies to require fast response and high photon output.
5. Compared to $CsPbX_3$ perovskites, A_3BX_6 MHPs are intrinsically lead-free and exhibit good thermal and radiation stability due to their vacancy-ordered framework and strong B–X bonding. However, environmental factors may still affect their long-term performance. Under high-humidity conditions, certain compositions may undergo hydration-induced phase transitions, which introduce structural defects and degrade luminescence performance. To enhance moisture resistance, strategies such as encapsulation, surface passivation, halide substitution, and lattice rigidification via cation engineering can be used to suppress ion migration and structural rearrangement. Under prolonged irradiation, A_3BX_6 MHPs generally demonstrate high radiation hardness. For example, $Rb_3InCl_6:Sb^{3+}$ exhibits nearly unchanged RL intensity under a cumulative dose of 561.6 Gy, while $Cs_2NaLuCl_6/Cs_3LuCl_6:Sb^{3+}$ maintains stable RL output up to 1,000 Gy. Nevertheless, sustained irradiation may still induce defect accumulation and halide vacancy formation, thereby increasing nonradiative recombination pathways. Further improvement in radiation tolerance requires minimizing initial defect densities, enhancing

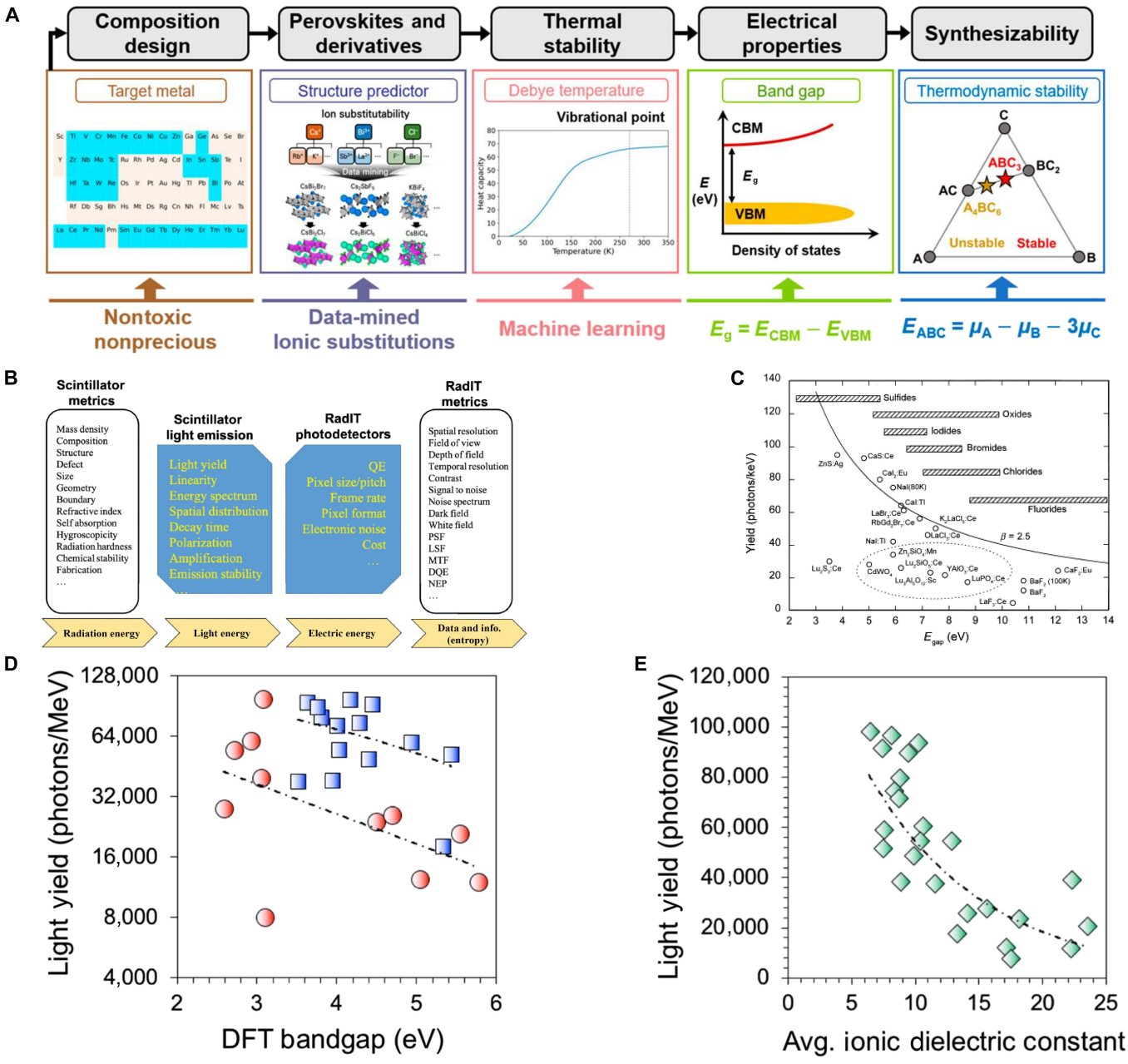


Fig. 17. (A) Workflow of computational exploration for inorganic halide perovskite derivatives. Adapted with permission [174]. Copyright 2022, published by American Chemical Society. (B) Radiographic imaging and tomography (RadIT) metrics and scintillator metrics are correlated through the energy and data (information) flows. Adapted with permission [175]. PSF, point spread function; LSF, line spread function; DQE, detective quantum efficiency; NEP, noise equivalent power. Copyright 2023, published by Institute of Electrical and Electronics Engineers Inc. (C) Empirical trend between light yield and material's bandgap for a range of scintillator compounds. Adapted with permission [184]. Copyright 2002, published by Elsevier. (D) Trends of experimentally reported light yield (L.Y.) with density functional theory (DFT)-computed bandgaps and (E) averaged ionic part of the dielectric constants. Adapted with permission [176]. Copyright 2019, published by Springer.

crystal quality, and strengthening structural stability through cation engineering.

Overall, the above strategies demonstrate that B-site cation engineering is central to achieving enhanced luminescence and scintillation in A_3BX_6 MHPs, providing a foundation for further optimization of synthesis methods, dopant–host compatibility, and interface modification. The incorporation of ns^2, transition-metal, and RE dopants enables diverse radiative pathways, supporting applications ranging from PL and EL to high-energy radiation detection. Despite the substantial progress achieved, challenges remain in large-scale single-crystal growth, long-term stability, and standardized device evaluation. Future advances may be accelerated by artificial-intelligence-assisted materials discovery, improved crystal engineering, and deeper understanding of carrier dynamics, paving the way for the practical implementation of A_3BX_6 MHPs in next-generation optoelectronic and radiation detection technologies.

Acknowledgments

Funding: This work was financially supported by National Natural Science Foundation of China (NSFC) (nos. 12505355, 52220105010, and M-0755), Lundbeck Foundation (R521-2025-1587), RSC

Researcher Collaborations Grant (C25-1261222948), Postdoctoral Program funded by China Scholarships Council during a visit of "Hang Yin" to Lund University (no. 202408330350), and the Youth Innovation Team Plan of Shandong Province (grant no. 2024KJH154). J.C. acknowledges support from the Novo Nordisk Foundation (NNF22OC0073582).

Author contributions: X.Z. summarized the literature and prepared the original draft. H.Y. contributed to conceptualization, methodology, and revision of the manuscript. Q.W., D.C., and D.X. classified the literature and provided supervision. T.P. and J.C. contributed to manuscript editing and review. H.Y. and L.Q. conceived the project.

Competing interests: The authors declare that they have no competing interests.

Supplementary Materials

Fig. S1

References

1. Ou X, Chen X, Xu X, Xie L, Chen X, Hong Z, Bai H, Liu X, Chen Q, Li L, et al. Recent development in x-ray imaging technology: Future and challenges. *Research*. 2021;2021:Article 9892152.
2. Lian H, Zhang W, Zou R, Gu S, Kuang R, Zhu Y, Zhang X, Ma C-G, Wang J, Li Y. Aqueous-based inorganic colloidal halide perovskites customizing liquid scintillators. *Adv Mater*. 2023;35(51):2304743.
3. Zhou Y, Chen J, Bakr OM, Mohammed OF. Metal halide perovskites for x-ray imaging scintillators and detectors. *ACS Energy Lett*. 2021;6(2):739–768.
4. Feng SC, Hu XM, Shen Y, Li YQ, Tang JX, Lee ST. Phase regulation of layered perovskites toward high-performance light-emitting diodes. *Adv Funct Mater*. 2025;35(21):2310220.
5. Xu Q, Wang J, Shao W, Ouyang X, Wang X, Zhang X, Guo Y, Ouyang X. A solution-processed zero-dimensional all-inorganic perovskite scintillator for high resolution gamma-ray spectroscopy detection. *Nanoscale*. 2020;12(17):9727–9732.
6. Tourougui S, Alla M, El-assib H, Rouchdi M, Fares B. Next-generation lead-free halide perovskites: $CsInX_3$ (X = Br, cl) for high-efficiency solar cells. *Computat Conden Matter*. 2026;46:Article e01193.
7. Borges-Martínez M, Saavedra-Torres M, Schott E, Zarate X. Computational design and properties elucidation of new $(FAPbI_3)_{1-x-y}(MAPbBr_3)_y(CsPbBr_3)_x$ photoactive systems for their application in perovskite solar cells. *Mater Today Commun*. 2023;34:Article 105324.
8. Chen Q, Wu J, Ou X, Huang B, Almutlaq J, Zhumekenov AA, Guan X, Han S, Liang L, Yi Z. All-inorganic perovskite nanocrystal scintillators. *Nature*. 2018;561(7721):88–93.
9. He Y, Matei L, Jung HJ, McCall KM, Chen M, Stoumpos CC, Liu Z, Peters JA, Chung DY, Wessels BW. High spectral resolution of gamma-rays at room temperature by perovskite $CsPbBr_3$ single crystals. *Nat Commun*. 2018;9(1):1609.
10. Pu G, Wang R, Tang Y, Song J, Wang J. Cation doping engineering of metal halide perovskite for high-energy x-ray exploration. *Mater Chem Front*. 2025;9(13):1945–1197.
11. Xiao Z, Song Z, Yan Y. From lead halide perovskites to lead-free metal halide perovskites and perovskite derivatives. *Adv Mater*. 2019;31(47):1803792.
12. Buñuel MA, Lozano L, Chaminade JP, Moine B, Jacquier B. Optical properties of Tb^{3+}-doped Rb_2KInF_6 elpasolite. *Opt Mater*. 1999;13(2):211–223.
13. Guo Q, Wang L, Yang L, Duan J, Du H, Ji G, Liu N, Zhao X, Chen C, Xu L. Spectra stable deep-blue light-emitting diodes based on cryolite-like cerium(III) halides with nanosecond df emission. *Sci Adv*. 2022;8(50): Article eabq2148.
14. Yang L, Du H, Li J, Luo Y, Lin X, Pang J, Liu Y, Gao L, He S, Kang J-W. Efficient deep-blue electroluminescence from Ce-based metal halide. *Nat Commun*. 2024;15(1):6240.
15. Panchanan S, Dastgeer G, Dutta S, Hu M, Lee S-U, Im J, Seok SI. Cerium-based halide perovskite derivatives: A promising alternative for lead-free narrowband UV photodetection. *Matter*. 2024;7(11):3949–3969.
16. Zhou W, Yu Y, Han P, Li C, Wu T, Ding Z, Liu R, Zhang R, Luo C, Li H. Sb-doped Cs_3TbCl_6 nanocrystals for highly efficient narrow-band green emission and x-ray imaging. *Adv Mater*. 2024;36(2):2302140.
17. Zhuravleva M, Yang K, Melcher C. Crystal growth and scintillation properties of Cs_3CeCl_6 and $CsCe_2Cl_7$. *J Cryst Growth*. 2011;318(1):809–812.
18. Yan J, Zhang S, Wei Q, Cao S, Zhao J, Zou B, Zeng R. Stoichiometry-controlled phase engineering of cesium bismuth halides and reversible structure switch. *Adv Opt Mater*. 2022;10(5):2101406.
19. Han JH, Samanta T, Cho HB, Jang SW, Viswanath N, Kim YR, Seo JM, Im WB. Intense hydrochromic photon upconversion from lead-free 0D metal halides for water detection and information encryption. *Adv Mater*. 2023;35(40):2302442.
20. Yang M, Ge W, Teranishi T. Unveiling the antithermal quenching behavior in 0D inorganic metal halide $Cs_2InCl_5(H_2O)$ mediated by upconversion emission. *Inorg Chem*. 2024;63(51):24400–24409.
21. Gong Z, Zheng W, Huang P, Cheng X, Zhang W, Zhang M, Han S, Chen X. Highly efficient Sb^{3+} emitters in 0D cesium indium chloride nanocrystals with switchable photoluminescence through water-triggered structural transformation. *Nano Today*. 2022;44:Article 101460.
22. Liang X, Zhang W, Shi Y, Zhang W, Yang H, Huang P, Li L, Zhang Q, Zheng W, Chen X. Sb^{3+}–doped 0D Cs_3GdCl_6 microcrystals with a near-unity photoluminescence quantum yield and high thermal quenching resistance for light-emitting application. *J Mater Chem C*. 2024;12(15):5538–5548.
23. Li Q, Xu B, Chen Z, Han J, Tan L, Luo Z, Shen P, Quan Z. Excitation-dependent emission color tuning of 0D $Cs_2InBr_5{\cdot}H_2O$ at high pressure. *Adv Funct Mater*. 2021;31(38):2104923.
24. Li J, Sheng Y, Tong G, Zhu H, Tao X, Wu C, Chang Y, Tang Z, Yang J, Zhang S. Anti-solvent synthesis of three-color indium-based halide perovskite microplate/microcrystal phosphors for high color rendering WLEDs. *Adv Opt Mater*. 2023;11(16):2300100.
25. Wang Y, Wen X, Shi H, Mihóková E, Kucerkova R, Babin V, Zhu J, Xiao J, Nikl M, OuYang X, et al. Giant scintillation yield enhancement in zero-dimensional halides by exciton confinement manipulation. *Research*. 2026;**9**:Article 1230.
26. Song J, Li J, Li X, Xu L, Dong Y, Zeng H. Quantum dot light-emitting diodes based on inorganic perovskite cesium lead halides ($CsPbX_3$). *Adv Mater*. 2015;27(44): 7162–7167.

27. Wang M, Chen X, Zhang F, Ma Z, Ji X, Cheng S, Pan G, Wu D, Li X-J, Zhang Y, et al. Colloidal synthesis of blue-emitting Cs_3TmCl_6 nanocrystals via localized Excitonic recombination for down-conversion white light-emitting diodes. *ACS Nano*. 2024;18(44):30421–30432.
28. Zhang B, Wu X, Zhou S, Liang G, Hu Q. Self-trapped exciton emission in inorganic copper(I) metal halides. *Front Optoelectron*. 2021;14(4):459–472.
29. Wang T, Zeng G, Yang YM, Yang Z, Wang T, Li H, Han L, Yu X, Xu X, Ouyang X. Advances in metal halide perovskite scintillators for x-ray detection. *Nano-Micro Lett*. 2025;17(1):275.
30. Ma W, Su Y, Zhang Q, Deng C, Pasquali L, Zhu W, Tian Y, Ran P, Chen Z, Yang G. Thermally activated delayed fluorescence (TADF) organic molecules for efficient x-ray scintillation and imaging. *Nat Mater*. 2022;21(2):210–216.
31. Han JH, Samanta T, Park YM, Kim HJ, Manikanta Viswanath NS, Kim HW, Cha BK, Cho SB, Im WB. Highly stable zero-dimensional lead-free metal halides for x-ray imaging. *ACS Energy Lett*. 2022;8(1):545–552.
32. Samulon E, Gundiah G, Gascón M, Khodyuk I, Derenzo S, Bizarri G, Bourret-Courchesne E. Luminescence and scintillation properties of Ce^{3+}-activated $Cs_2NaGdCl_6$, Cs_3GdCl_6, $Cs_2NaGdBr_6$ and Cs_3GdBr_6. *J Lumin*. 2014;153:64–72.
33. Zhou L, Liao JF, Qin Y, Wang XD, Wei JH, Li M, Kuang DB, He R. Activation of self-trapped emission in stable bismuth-halide perovskite by suppressing strong exciton–phonon coupling. *Adv Funct Mater*. 2021;31(31):2102654.
34. Wei H, Zhuravleva M, Tyagi M, Melcher CL. Scintillation properties of Cs_3LaCl_6:Ce^{3+} and Cs_3LaBr_6:Ce^{3+}. *IEEE Trans Nucl Sci*. 2013;61(1):390–396.
35. Liu M, Duan C-K, Tanner PA, Ma C-G, Yin M. Rationalizing the photoluminescence of Bi^{3+} and Sb^{3+} in double perovskite halide crystals. *J Phys Chem C*. 2021;125(48):26670–26678.
36. Nie J, Zhou B, Fang S, Wang Y, Wang Y, Tian B, Hu H, Zhong H, Li H, Shi Y. Chemical doping of lead-free metal-halide-perovskite related materials for efficient white-light photoluminescence. *Mater Today Phys*. 2023;31: Article 100992.
37. Ming J, Chen Y, Miao H, Fan Y, Wang S, Chen Z, Guo Z, Guo Z, Qi L, Wang X, et al. High-brightness transition metal-sensitized lanthanide near-infrared luminescent nanoparticles. *Nat Photonics*. 2024;18(12):1254–1262.
38. Ming J, Xie Z, Wu J, Zhang F. Synthesis of transition metal-sensitized lanthanide near-infrared luminescent nanoparticles. *Nat Protoc*. 2025;21(4):1544–1573.
39. Kong Q, Yang B, Chen J, Zhang R, Liu S, Zheng D, Zhang H, Liu Q, Wang Y, Han K. Phase engineering of cesium manganese bromides nanocrystals with color-tunable emission. *Angew Chem Int Ed Engl*. 2021;60(36):19653–19659.
40. Morad V, Cherniukh I, Pöttschacher L, Shynkarenko Y, Yakunin S, Kovalenko MV. Manganese(II) in tetrahedral halide environment: Factors governing bright green luminescence. *Chem Mater*. 2019;31(24):10161–10169.
41. Feng X, Zhang L, Feng X, You J, Pi J, Zeng H, Chu D, Xue C, Zhao K, Jia S. Ion migration suppression via doping multivalent cations in perovskite for high thermal stability x-ray detectors. *ACS Energy Lett*. 2025;10(2): 685–695.
42. Yin H, Song B, Tong Y, Zhan Y, Wei Q, Cai P, Liu Z, Li J, Chen J, Liu J. Ultrafast scintillator based on zirconium-doped cesium zinc chloride single crystals and their charge carrier dynamics. *Laser Photonics Rev*. 2024;18(12):2400394.
43. Lu M, Zhang X, Bai X, Wu H, Shen X, Zhang Y, Zhang W, Zheng W, Song H, Yu WW. Spontaneous silver doping and surface passivation of $CsPbI_3$ perovskite active layer enable light-emitting devices with an external quantum efficiency of 11.2%. *ACS Energy Lett*. 2018;3(7):1571–1577.
44. Ji F, Huang Y, Wang F, Kobera L, Xie F, Klarbring J, Abbrent S, Brus J, Yin C, Simak SI. Near-infrared light-responsive Cu-doped $Cs_2AgBiBr_6$. *Adv Funct Mater*. 2020;30(51):2005521.
45. Jiang C, Liu Q, Li L, Li K, Feng Y, Fu Y, Li Y, Qian X, Wei B, Du P. Tailoring of visible-NIR-II luminescence in Pt^{4+}/Er^{3+}-codoped Cs_2ZrCl_6 double perovskite phosphors via energy transfer engineering for diversified applications. *Laser Photonics Rev*. 2025;19(13):2401940.
46. Serna-Gallén P, Beltrán-Mir H, Cordoncillo E, West AR, Balda R, Fernández J. Site-selective symmetries of Eu^{3+}-doped $BaTiO_3$ ceramics: A structural elucidation by optical spectroscopy. *J Mater Chem C*. 2019;7(44):13976–13985.
47. Zhang X, Wang Y, Wu X, Wang F, Ou Q, Zhang S. A comprehensive review on mechanisms and applications of rare-earth based perovskite nanocrystals. *Chin J Chem*. 2024;42(9):1032–1056.
48. Liu Y, Rong X, Li M, Molokeev MS, Zhao J, Xia Z. Incorporating rare-earth terbium(III) ions into $Cs_2AgInCl_6$: Bi nanocrystals toward tunable photoluminescence. *Angew Chem Int Ed*. 2020;59(28):11634–11640.
49. Li G, Tian Y, Zhao Y, Lin J. Recent progress in luminescence tuning of Ce^{3+} and Eu^{2+}-activated phosphors for pc-WLEDs. *Chem Soc Rev*. 2015;44(23):8688–8713.
50. Li H, Zhang M, Li Y, Fu X, Feng J, Zhang H. Efficient multi-luminescence covering the visible to near-infrared range in antimony and lanthanide co-doped indium-based zero-dimensional perovskites nanocrystals. *Adv Opt Mater*. 2023;11(17):2300429.
51. Stefanski M, Bondzior B, Basinski A, Ptak M, Lou B, Ma C-G. Synthesis and characterization of a $CsPbCl_3$ perovskite doped with Nd^{3+}: Structural, optical, and energy transfer properties. *Inorg Chem Front*. 2024;11(9):2626–2633.
52. Zhou B, Muhammad Y, Ding D, Liu Z, Hu H, Wang Y, Zhong H, Shi Y, Li H. Dexter energy transfer in zero-dimensional inorganic metal halides for obtaining near-unity PLQY via Sb^{3+}/Mn^{2+} codoping. *J Phys Chem C*. 2024;128(1):571–579.
53. Olaya-Castro A, Scholes GD. Energy transfer from Förster–Dexter theory to quantum coherent light-harvesting. *Int Rev Phys Chem*. 2011;30(1):49–77.
54. Vyazovkin S, Burnham AK, Favergeon L, Koga N, Moukhina E, Pérez-Maqueda LA, Sbirrazzuoli N. ICTAC kinetics committee recommendations for analysis of multi-step kinetics. *Thermochim Acta*. 2020;689: Article 178597.
55. Bünzli J-CG, Eliseeva SV. Basics of lanthanide photophysics. In: Hänninen P, Härmä H, editors. *Lanthanide luminescence: Photophysical, analytical and biological aspects*. Berlin (Heidelberg): Springer; 2011. p. 1–45.
56. Dorenbos P. Thermal quenching of lanthanide luminescence via charge transfer states in inorganic materials. *J Mater Chem C*. 2023;11(24):8129–8145.
57. Saidaminov MI, Mohammed OF, Bakr OM. Low-dimensional-networked metal halide perovskites: The next big thing. *ACS Energy Lett*. 2017;2(4):889–896.

58. Gundiah G, Brennan K, Yan Z, Samulon EC, Wu G, Bizarri GA, Derenzo SE, Bourret-Courchesne ED. Structure and scintillation properties of Ce^{3+}-activated $Cs_2NaLaCl_6$, Cs_3LaCl_6, $Cs_2NaLaBr_6$, Cs_3LaBr_6, Cs_2NaLaI_6 and Cs_3LaI_6. *J Lumin*. 2014;149:374–384.
59. Zhang C, Feng X, Song Q, Zhou C, Peng L, Chen J, Liu X, Chen H, Lin J, Chen X. Blue-violet emission with near-unity photoluminescence quantum yield from Cu(I)-doped Rb_3InCl_6 single crystals. *J Phys Chem Lett*. 2021;12(33): 7928–7934.
60. Kachhap S, Singh S, Singh AK, Singh SK. Lanthanide-doped inorganic halide perovskites ($CsPbX_3$): Novel properties and emerging applications. *J Mater Chem C*. 2022;10(10): 3647–3676.
61. Locardi F, Cirignano M, Baranov D, Dang Z, Prato M, Drago F, Ferretti M, Pinchetti V, Fanciulli M, Brovelli S, et al. Colloidal synthesis of double perovskite $Cs_2AgInCl_6$ and Mn-doped $Cs_2AgInCl_6$ nanocrystals. *J Am Chem Soc*. 2018;140(40):12989–12995.
62. Senden T, van Dijk-Moes RJA, Meijerink A. Quenching of the red Mn^{4+} luminescence in Mn^{4+}-doped fluoride LED phosphors. *Light Sci Appl*. 2018;7(1):8.
63. Sharma AA, Pradhan PP, Prasad KAKD, Rakshita M, Pembarthi R, Haranath D. Multimodal luminescence and energy transfer mechanism in a narrowband UVB emitting phosphor system towards futuristic phototherapeutic devices. *Mater Adv*. 2025;6(22):8400–8413.
64. Venkatramu V, Babu P, Martín IR, Lavín V, Muñoz-Santiuste JE, Tröster T, Sievers W, Wortmann G, Jayasankar CK. Role of the local structure and the energy trap centers in the quenching of luminescence of the Tb^{3+} ions in fluoroborate glasses: A high pressure study. *J Chem Phys*. 2010;132(11):Article 114505.
65. Zhu D, Zaffalon ML, Zito J, Cova F, Meinardi F, De Trizio L, Infante I, Brovelli S, Manna L. Sb-doped metal halide nanocrystals: A 0D versus 3D comparison. *ACS Energy Lett*. 2021;6(6):2283–2292.
66. Fu P, Hu S, Tang J, Xiao Z. Material exploration via designing spatial arrangement of octahedral units: A case study of lead halide perovskites. *Front Optoelectron*. 2021;14(2):252–259.
67. Zhang B, Ru Y, Zhou J, Jia J, Song H, Liu Z, Zhang L, Liu X, Zhong G-M, Yong X, et al. A robust anti-thermal-quenching phosphor based on zero-dimensional metal halide Rb_3InCl_6:xSb^{3+}. *J Am Chem Soc*. 2024;146(11):7658–7667.
68. Karluk AA, Nematulloev S, Thomas S, Hasanov BE, Yorov K, Naphade R, Gutiérrez-Arzaluz L, Mohammad B, Abulikemu M, Mahmood J, et al. Scalable synthesis of Sb-doped Rb_3InCl_6 nanocrystals for high-resolution x-ray imaging screen. *Cell Rep Phys Sci*. 2025;6(2):Article 102427.
69. Yang Z, Cui J, Sun Y, Yao J, Yang S, Song J. Na-alloy tailored 3D/0D metal halide heterostructures enabling efficient charge transfer for color-integrated white scintillators. *Nat Commun*. 2025;16(1):6909.
70. Saidaminov MI, Almutlaq J, Sarmah S, Dursun I, Zhumekenov AA, Begum R, Pan J, Cho N, Mohammed OF, Bakr OM. Pure Cs_4PbBr_6: Highly luminescent zero-dimensional perovskite solids. *ACS Energy Lett*. 2016;1(4):840–845.
71. Zhang F, Ji X, Liang W, Li Y, Ma Z, Wang M, Wang Y, Wu D, Chen X, Yang D. Room-temperature synthesis of blue-emissive zero-dimensional cesium indium halide quantum dots for temperature-stable down-conversion white light-emitting diodes with a half-lifetime of 186 h. *Mater Horiz*. 2021;8(12):3432–3442.
72. Li H, Tian L, Yang Q, Wang N, Fu X, Zhou L, Feng J, Zhang H. Sb^{3+} doped Cs_3YCl_6 metal halides with highly efficient broad-band green emission for light-emitting diode and x-ray imaging. *SCIENCE CHINA Chem*. 2025;68(6):2459–2466.
73. Wang L, Guo Q, Duan J, Xie W, Ji G, Li S, Chen C, Li J, Yang L, Tan Z. Exploration of nontoxic Cs_3CeBr_6 for violet light-emitting diodes. *ACS Energy Lett*. 2021;6(12):4245–4254.
74. Hou C, Liu X, Wan C, Li B, Lu T, Ge C, Song Y, Wang A, Kang Y, Dong Q. Designing guanidine-based antimony halides luminescence perovskite crystals toward near-unity quantum yield. *Chem Mater*. 2023;35(24):10635–10644.
75. Yu L, Wang Y, Xing X, Xu Z, Shang M. Enhancing the thermal stability of the NIR emitting $A_2InCl_5{\cdot}H_2O$:Cr^{3+} phosphor based on A site regulation. *J Mater Chem C*. 2024;12(33):13021–13028.
76. Cao Y, Wang N, Tian H, Guo J, Wei Y, Chen H, Miao Y, Zou W, Pan K, He Y. Perovskite light-emitting diodes based on spontaneously formed submicrometre-scale structures. *Nature*. 2018;562(7726):249–253.
77. Singh K, Singh H, Sharma G, Gerward L, Khanna A, Kumar R, Nathuram R, Sahota HS. Gamma-ray shielding properties of CaO–SrO–$B2O_3$ glasses. *Radiat Phys Chem*. 2005;72(2-3):225–228.
78. Attix FH (Ed). *Introduction to radiological physics and radiation dosimetry*. Hoboken (NJ): John Wiley & Sons; 2008.
79. Knoll GF (Ed). *Radiation detection and measurement*. Hoboken (NJ): John Wiley & Sons; 2010.
80. Yuge Zhang GM, Wang P, Bao Z, Ouyang X, Liu L, Ouyang X. Light yield measurement technology and optimization methods of x-ray imaging scintillator. *Chin J Lumin*. 2025;46(4):630–641.
81. Miller SR, Gaysinskiy V, Shestakova I, Nagarkar VV. Recent advances in columnar CsI(Tl) scintillator screens. In: *Penetrating radiation systems and applications VII*. Bellingham (WA): SPIE; 2005. vol. 5923. p. 99–108.
82. Krupčík J, Májek P, Gorovenko R, Blaško J, Kubinec R, Sandra P. Considerations on the determination of the limit of detection and the limit of quantification in one-dimensional and comprehensive two-dimensional gas chromatography. *J Chromatogr A*. 2015;1396:117–130.
83. Li H, Li K, Li Z, Fu X, Yang Q, Wang N, Wang X, Feng J, Song S, Zhang H. Lanthanide-based metal halides prepared at room temperature by recrystallization method for x-ray imaging. *Light Sci Appl*. 2025;14(1):195.
84. Kasap S, Frey JB, Belev G, Tousignant O, Mani H, Greenspan J, Laperriere L, Bubon O, Reznik A, DeCrescenzo G, et al. Amorphous and polycrystalline photoconductors for direct conversion flat panel x-ray image sensors. *Sensors*. 2011;11(5):5112–5157.
85. Hafızoğlu N. Efficiency and energy resolution of gamma spectrometry system with HPGe detector depending on variable source-to-detector distances. *Eur Phys J Plus*. 2024;139(2):134.
86. Zhou L, Liao J-F, Huang Z-G, Wei J-H, Wang X-D, Li W-G, Chen H-Y, Kuang D-B, Su C-Y. A highly red-emissive lead-free indium-based perovskite single crystal for sensitive water detection. *Angew Chem Int Ed Engl*. 2019;58(16): 5277–5281.
87. Han P, Luo C, Yang S, Yang Y, Deng W, Han K. All-inorganic l0ead-free 0D perovskites by a doping strategy to achieve a

PLQY boost from <2 % to 90 %. *Angew Chem Int Ed Engl*. 2020;59(31):12709–12713.
88. Li X, Wang Z, Sun H, Bai F, Xu S, Wang C. Solvent stimuli-responsive off-on fluorescence induced by synergistic effect of doping and phase transformation for Te^{4+} doped indium halide perovskite: Giving printable and colorless ink for information encryption and decryption. *J Colloid Interface Sci*. 2023;633:808–816.
89. Huang J, Chang T, Zeng R, Yan J, Wei Q, Zhou W, Cao S, Zou B. Controlled structural transformation in Sb-doped indium halides A_3InCl_6 and $A_2InCl_5{\cdot}H_2O$ yields reversible green-to-yellow emission switch. *Adv Opt Mater*. 2021;9(13):2002267.
90. Zhang F, Yang D, Shi Z, Qin C, Cui M, Ma Z, Wang L, Wang M, Ji X, Chen X, et al. Stable zero-dimensional cesium indium bromide hollow nanocrystals emitting blue light from self-trapped excitons. *Nano Today*. 2021;38:Article 101153.
91. Meng W, Wang X, Xiao Z, Wang J, Mitzi DB, Yan Y. Parity-forbidden transitions and their impact on the optical absorption properties of lead-free metal halide perovskites and double perovskites. *J Phys Chem Lett*. 2017;8(13):2999–3007.
92. Song H, Yuan J, Mu D, Han L, Xu X, Zhang P. Te^{4+} doped zero-dimensional perovskites for dual-mode thermometry in electronic devices. *J Mater Chem C*. 2025;13(7):3465–3474.
93. Chen S, Li X, Zhang J, Pan D, Kong Y. Cation-substitution-induced high spectral tunability and thermosensitivity in double halide perovskite $Cs_2InCl_5{\cdot}H_2O$. *Opt Mater*. 2024;156:Article 115974.
94. Zhou B, Fang F, Liu Z, Zhong H, Zhou K, Hu H, Min J, Zheng F, Fang S, Nie J, et al. Self-trapped Exciton emission in highly polar 0D hybrid ammonium/hydronium-based perovskites triggered by antimony doping. *J Am Chem Soc*. 2024;146(22):15198–15208.
95. Liu Z, Zhou B, Fang S, Nie J, Zhong H, Hu H, Li H, Shi Y. Modulation of the excitation states in all-inorganic halide perovskites via Sb^{3+} and Bi^{3+} codoping. *J Phys Chem Lett*. 2023;14(4):1022–1028.
96. Zhou B, Liu Z, Fang S, Nie J, Zhong H, Hu H, Li H, Shi Y. Emission mechanism of self-trapped excitons in Sb^{3+}-doped all-inorganic metal-halide perovskites. *J Phys Chem Lett*. 2022;13(39):9140–9147.
97. Zhang G, Dang P, Lian H, Li K, Tian L, Yang W, Cheng Z, Lin J. Assembling two self-trapped exciton emissions in 0D metal halides with near-unity quantum yield and zero thermal-quenching photoluminescence. *Laser Photonics Rev*. 2024;18(1):2300599.
98. Hu B, Dong G, Li X, Zhang J, Chen C, Zhou J, Kong D, Wu W. $Rb_2InCl_5{\cdot}H_2O$ doped with Te^{4+} for fluorescence thermometry and coordinated water-related structural phase transformation. *Opt Lett*. 2024;49(21):6205–6208.
99. Wei J-H, Luo J-B, Liao J-F, Ou W-T, Kuang D-B. Te^{4+}-doped $Cs_2InCl_5{\cdot}H_2O$ single crystals for remote optical thermometry. *Sci China-Mater*. 2022;65(3):764–772.
100. Chen D, Wu C, Li H, Zhou L, Chen P, Pang Q, Zhang X, Zhang JZ. Near-infrared emission, energy transfer, and mechanisms of Mn^{2+} and Cr^{3+} Codoped lead-free Cs 2 AgInCl 6 double perovskites. *J Mater Chem C*. 2023;11(37):12649–12657.
101. Liu Z, Qin X, Liu X. Luminescence enrichment in perovskite-lanthanide composites: Complexity and complementarity. In: *Handbook on the physics and chemistry of rare earths*. Amsterdam (Netherlands): Elsevier; 2022. vol. 61. p. 1–29.
102. Sheng Y, Chen P, Gao Y, He Y, Li J, Muhammad, Xie X, Cheng C, Yang JT, Chang YJ, et al. Tuneable efficient white emission of Sb^{3+}/Mn^{2+} co-doped lead-free perovskites for single-component white light-emitting diodes. *ACS Appl Mater Interfaces*. 2024;16(15):19175–19183.
103. Jing L, Cen Q, Pang Q, Zhang JZ. Enhancing photoluminescence and stability of Mn-doped $Cs_2InCl_5{\cdot}H_2O$ microcrystals with introduced Bi^{3+} ion. *J Phys Chem C*. 2023;127(5):2448–2455.
104. Shao H, Wu X, Zhu J, Xu W, Xu L, Dong B, Hu J, Dong B, Bai X, Cui H, et al. Mn^{2+} ions doped lead-free zero-dimensional K_3SbCl_6 perovskite nanocrystals towards white light emitting diodes. *Chem Eng J*. 2021;413:Article 127415.
105. Fan Q, Xu H, Zhu Z-K, Zhao Z, Rong H, Zhu P, Guo W, Tang L, Zhang J, Luo J, et al. 3D lead-free double perovskite via anchoring A-site cation for ultralow dose and stable x-ray detection. *Adv Funct Mater*. 2025;35(37):2505546.
106. Mabate TP, Maqunga NP, Ntshibongo S, Maumela M, Bingwa N. Metal oxides and their roles in heterogeneous catalysis: Special emphasis on synthesis protocols, intrinsic properties, and their influence in transfer hydrogenation reactions. *SN Appl Sci*. 2023;5(7):196.
107. Sahoo K, Kumar S, Mohapatra A, Dubey NK, Naik R, Goswami C, Bhaumik S. Highly stable and luminescent formamidinium-based perovskite nanocrystal probe for temperature and mercury sensors and in vitro imaging in live cells. *J Mater Chem C*. 2024;12(42):17315–17327.
108. Li M, Wang S, Wood A, Yeager JD, Stepanoff SP, Adler JC, Shi Z, Wang J, Li Z, Wolfe DE. Defect repairing in lead bromide perovskite single crystals with biasing and bromine for x-ray photon-counting detectors. *Nat Mater*. 2025;24(12):1993–2000.
109. Mo Q, Yu J, Chen C, Cai W, Zhao S, Li H, Zang Z. Highly efficient and ultra-broadband yellow emission of lead-free antimony halide toward white light-emitting diodes and visible light communication. *Laser Photonics Rev*. 2022;16(10):2100600.
110. Morad V, Yakunin S, Kovalenko MV. Supramolecular approach for fine-tuning of the bright luminescence from zero-dimensional antimony(III) halides. *ACS Materi Lett*. 2020;2(7):845–852.
111. Song Y, Li L, Bi W, Hao M, Kang Y, Wang A, Wang Z, Li H, Li X, Fang Y, et al. Atomistic surface passivation of $CH_3NH_3PbI_3$ perovskite single crystals for highly sensitive coplanar-structure x-ray detectors. *Research*. 2020;2020:Article 5958243.
112. Chen D, Dai F, Hao S, Zhou G, Liu Q, Wolverton C, Zhao J, Xia Z. Crystal structure and luminescence properties of lead-free metal halides $(C_6H_5CH_2NH_3)_3MBr_6$ (M = Bi and Sb). *J Mater Chem C*. 2020;8(22):7322–7329.
113. Zhizhuan Zhang JJ, Gong L, Kezhao D, Huang X. Two new antimony (III) chloride hybrids composed of mononuclear $SbCl_6$. $^{3-}$ unit and ionic liquid cations with different length of alkyl chain. *Chinese Journal of Structural Chemistry*. 2021.
114. Mirochnik AG, Petrochenkova N, Storozhuk TV, Lifar LI. Synthesis, structure, and luminescent properties of antimony(III) complexes with *N*,*N*-diphenylguanidine. *Russ J Coord Chem*. 2001;27:783–785.
115. Peng Y-C, Zhang Z-Z, Lin Y-P, Jin J-C, Zhuang T-H, Gong L-K, Wang Z-P, Du K-Z, Huang X-Y. A deep-red-emission antimony(III) chloride with dual-cations: Extremely large stokes shift due to high $SbCl_6$ distortion. *Chem Commun*. 2021;57(100):13784–13787.

116. Zhao J-Q, Shi H-S, Zeng L-R, Ge H, Hou Y-H, Wu X-M, Yue C-Y, Lei X-W. Highly emissive zero-dimensional antimony halide for anti-counterfeiting and confidential information encryption-decryption. *Chem Eng J*. 2022;431:Article 134336.
117. Wang Z, Huang X. Stepwise structural transformation in hybrid antimony chloride for time-resolved and multi-stage informational encryption and anti-counterfeiting. *Inorg Chem Front*. 2025;12(12):3997–4006.
118. Wang Z, Zhang Z, Tao L, Shen N, Hu B, Gong L, Li J, Chen X, Huang X. Hybrid chloroantimonates(III): Thermally induced triple-mode reversible luminescent switching and laser-printable rewritable luminescent paper. *Angew Chem Int Ed Engl*. 2019;58(29):9974–9978.
119. Wang Y, Wang Y, Zhan X, Shi H, Zhu W, Chen B, Liu S, Xu X, Zhao Q. Off-stoichiometry synthesis of 0D metal halide polycrystals for high-performance x-ray imaging. *Adv Opt Mater*. 2024;12(27):2401092.
120. Li H, He Y, Li W, Lu T, Tan M, Wei W, Yang B, Wei H. Perovskite dimensional evolution through cations engineering to tailor the detection limit in hard x-ray response. *Small*. 2022;18(42):2203884.
121. Zaffalon ML, Wu Y, Cova F, Gironi L, Li X, Pinchetti V, Liu Y, Imran M, Cemmi A, Di Sarcina I, et al. Zero-dimensional Gua_3SbCl_6 crystals as intrinsically reabsorption-free scintillators for radiation detection. *Adv Funct Mater*. 2023;33(48):2305564.
122. Yang H, Cai T, Liu E, Hills-Kimball K, Gao J, Chen O. Synthesis and transformation of zero-dimensional Cs_3BiX_6 (X = cl, Br) perovskite-analogue nanocrystals. *Nano Res*. 2020;13(1):282–291.
123. Tang Y, Liang M, Chang B, Sun H, Zheng K, Pullerits T, Chi Q. Lead-free double halide perovskite Cs_3BiBr_6 with well-defined crystal structure and high thermal stability for optoelectronics. *J Mater Chem C*. 2019;7(11):3369–3374.
124. Cao F, Yan T, Li Z, Wu L, Fang X. Dual-band perovskite bulk heterojunction self-powered photodetector for encrypted communication and imaging. *Adv Opt Mater*. 2022;10(18):2200786.
125. Shimizu M, Koshimizu M, Fujimoto Y, Yanagida T, Ono S, Asai K. Luminescence and scintillation properties of Cs_3BiCl_6 crystals. *Opt Mater*. 2016;61:115–118.
126. Tang Y, Gomez L, van der Laan M, Timmerman D, Sebastian V, Huang C-C, Gregorkiewicz T, Schall P. Room temperature synthesis and characterization of novel lead-free double perovskite nanocrystals with a stable and broadband emission. *J Mater Chem C*. 2021;9(1):158–163.
127. Cao F, Li Z, Liu X, Shi Z, Fang X. Air induced formation of $Cs_3Bi_2Br_9/Cs_3BiBr_6$ bulk heterojunction and its dual-band photodetection abilities for light communication. *Adv Funct Mater*. 2022;32(46):2206151.
128. Ma J, Zhang F, Xing Y, Jiang H, Tian Y, Ji H, Chen X, Wu D, Zeng L, Li X, et al. Self-powered UV dual-band photodetector based on Cs_3BiCl_6/GaN heterojunction for logical operation and encrypted photo-communication. *Adv Sci*. 2025;12(28):2503498.
129. Wang G, Jin Z, Chen Y, Chen F, Chen Q. Solvent modulated different stacking of cobalt chelates and their molecular magnetic behaviors. *J Mol Struct*. 2025;1336:Article 142047.
130. Jia Z, Gong P, Zhao J, Chen M, Wang Y, Wang Z, Dong Y, Xia M. Antimony-doped enhanced photoluminescence quantum yield in zero-dimensional lead-free metal halide $Rb_2CsBiCl_6$ crystals. *Inorg Chem Front*. 2022;9(23):6299–6304.
131. Chen R, Wang S, Lin F, Zheng Y, Zhang W, Wang J, Guo F. Stable broadband bright green emission of self-trapped excitons triggered by Sb^{3+} doping in zero-dimensional Cs_3BiCl_6. *Eur J Inorg Chem*. 2024;27(1):Article e202300366.
132. Jia Z, Gong P, Chen M, Wang Z, Li X, Song Y, Zhang S, Zhang N, Xia M. Antimony doping enabled photoluminescence quantum yield enhancement in 0D inorganic bismuth halide crystals. *Inorg Chem*. 2023;62(48):19690–19697.
133. Wu J, Zhang S, Yan J, Zou B, Zeng R. A new zero-dimensional $(CsK_2)BiCl_6$ metal halide: Boosting emission via B-site Mn-doping. *Crystals*. 2022;12(11):1681.
134. Guo T, Ning X, Deng Z, Lin J, Zhou D, Wen M, Wang Q, Wen Y, Qiu J. Sb^{3+}-doping induced quasi-2D single crystal growth from 0D Cs_3BiCl_6: Modulation of site-specific Cr^{3+} near-infrared emission. *Adv Opt Mater*. 2026;14(6):Article e02778.
135. Takahashi K, Arai M, Koshimizu M, Fujimoto Y, Yanagida T, Asai K. Luminescence and scintillation characteristics of Cs_3ScCl_6:Ce crystals. *Ceram Int*. 2020;46(16):26346–26349.
136. Wei H, Zhuravleva M, Meng F, Melcher CL. Temperature dependence spectroscopic study of Ce-doped Cs_3LaCl_6 and Cs_3LaBr_6 scintillators. *J Lumin*. 2015;160:64–70.
137. Kim D, Yun T, An S, Lee C-L. How to improve the structural stabilities of halide perovskite quantum dots: Review of various strategies to enhance the structural stabilities of halide perovskite quantum dots. *Nano Convergence*. 2024;11(1):4.
138. Zhang L, Sun C, He T, Jiang Y, Wei J, Huang Y, Yuan M. High-performance quasi-2D perovskite light-emitting diodes: From materials to devices. *Light Sci Appl*. 2021;10(1):61.
139. Lee M, Lee DHD, Hong SV, Woo HY, Chae J-Y, Lee DW, Han MJ, Paik T. Highly luminescent and multifunctional zero-dimensional cesium lanthanide chloride (Cs_3LnCl_6) colloidal nanocrystals. *Adv Opt Mater*. 2022;10(9):2102727.
140. Zhang R, Xu X, Mao X, Wang Z, Wang P, Yang Y, Chen J, Lu R, Deng W, Han K. Excitation-dependent emission in all-inorganic lead-free $Cs_2ScCl_5{\cdot}H_2O$ perovskite crystals. *Laser Photonics Rev*. 2022;16(5):2100689.
141. Huang Y, Pan Y, Peng C, Ding Y, Lian H, Li L, Lin J. Orange/cyan emissive sensors of Sb^{3+} for probing water via reversible phase transformation in rare-earth-based perovskite crystals. *Inorg Chem Front*. 2023;10(3):991–1000.
142. Samanta T, Viswanath NSM, Kim HW, Jang SW, Han JH, Cho SB, Im WB. Demystifying role of local distortion in emission colors tuning of lead-free zero-dimensional metal halide nanocrystals. *Chem Eng J*. 2024;484:Article 149697.
143. Samanta T, Viswanath NSM, Jang SW, Min JW, Cho HB, Han JH, Im WB. Thermally stable self-trapped assisted single-component white light from lead-free zero-dimensional metal halide nanocrystals. *Adv Opt Mater*. 2023;11(9):2202744.
144. Xie W, Wang T, Xu H, Liang H, Shen H, Xue H, Wang X, Xu F, Zhang J, Sun L, et al. A record efficiency of 1070 nm near-infrared light-emitting diodes based on $Cs_3La_{1-x}Nd_xX_6$ perovskite nanocrystals. *Adv Funct Mater*. 2026;Article e31915.
145. Mao X, Wang Z, Zhang F, Yin H, Xu X, Chen J, Chen Z, Luo J, Han K, Zhang R. All-inorganic zero-dimensional Sb^{3+}-doped $Rb_2ScCl_5(H_2O)$ perovskite single crystals: Efficient self-trapped exciton emission and x-ray detection. *J Phys Chem Lett*. 2023;14(6):1521–1527.
146. Combes CM, Dorenbos P, van Eijk CWE, Krämer KW, Güdel HU. Optical and scintillation properties of pure and

Ce^{3+}-doped Cs_2LiYCl_6 and Li_3YCl_6:Ce^{3+} crystals. *J Lumin*. 1999;82(4):299–305.
147. Lee M, Chung H, Hong SV, Woo HY, Chae J-Y, Yoon TY, Diroll BT, Paik T. Dynamically tunable multicolor emissions from zero-dimensional Cs_3LnCl_6 (ln: Europium and terbium) nanocrystals with wide color gamut. *Nanoscale*. 2023;15(4):1513–1521.
148. Yin H, Zhou X, Song B, Wang R, Li B, Sun J, Wei Q, Cai P, Chen Z, Yang F, et al. The scintillating dynamics of self-trapped exciton endowed/unendowed by thermally activated delayed fluorescence. *Laser Photonics Rev*. 2025;19(6):2401508.
149. Liang X, Xia H-L, Xiang J, Wang F, Ma J, Zhou X, Wang H, Liu X-Y, Zhu Q, Lin H, et al. Facile tailoring of metal-organic frameworks for Förster resonance energy transfer-driven enhancement in perovskite photovoltaics. *Adv Sci*. 2024;11(18):2307476.
150. Sun L, Dong B, Sun J, Wang Y, Wang Y, Hu S, Zhou B, Bai X, Xu L, Zhou D. Efficient and stable multicolor emissions of the coumarin-modified Cs_3LnCl_6 Lead-free perovskite nanocrystals and LED application. *Adv Mater*. 2024;36(18):2310065.
151. Wu Y, Shi H, Chakoumakos BC, Zhuravleva M, Du M-H, Melcher CL. Crystal structure, electronic structure, temperature-dependent optical and scintillation properties of $CsCe_2Br_7$. *J Mater Chem C*. 2015;3(43):11366–11376.
152. Xie W, Hu F, Gong S, Peng L. Study the optical properties of Cs_3CeI_6: First-principles calculations. *AIP Adv*. 2024;14(1):Article 015062.
153. Butman MF, Motalov VB, Kudin LS, Rycerz L, Gaune-Escard M. Thermodynamic characterization of the congruently melting Cs_3CeCl_6 compound. *J Chem Eng Data*. 2008;53(10):2346–2350.
154. Madarász J, Leskelä T, Pokol G, Niinistö L. Thermally induced changes in the oxidation state of cerium(IV). *J Therm Anal*. 1997;49(3):1347–1355.
155. Min JW, Samanta T, Lee AY, Jung YK, Viswanath NSM, Kim YR, Cho HB, Moon JY, Jang SH, Kim JH. Highly emissive lanthanide-based 0D metal halide nanocrystals for efficient ultraviolet photodetector. *Small*. 2024;20(43):2402951.
156. Bai X, Liao J, Lou B, Zhang Y, Zhao H, Zi Y, Li Y, Tang W, Mandl GA, Huang A, et al. Reversible photochromism and multicolor luminescence modulation for x-ray detection and secure information encryption. *Adv Funct Mater*. 2026;36(4):Article e06583.
157. Xie H, Zheng C, Lei Y, Peng G, Wu Y, Li Z, Wang Q, Jin Z. Single-source evaporated pixelated Cs_3CeBr_6 crystals based scintillator film for high spatial resolution x-ray imaging. *Adv Funct Mater*. 2026;Article e29234.
158. Chai Z, Wang Z, Ke D, Zeng M, Li G, Yang L, Peng X, Li X, Li Y. Thermally robust 0D Cs_3EuCl_6 microcrystals for x-ray imaging. *Small*. 2025;21(38):Article e05594.
159. Zhao C, Wang Y, Bao S, Zang Y, Liu X, Huang W. High-performance hybrid organic-inorganic lanthanide halide glass scintillators enabled by dehydration for efficient x-ray imaging. *Adv Mater*. 2025;37(21):2500925.
160. Lindsey AC, Zhuravleva M, Melcher CL. Growth of $CsCe_2Cl_7$ and Cs_3CeCl_6 utilizing the Bridgman method. In: *2013 IEEE nuclear science symposium and medical imaging conference (2013 NSS/MIC)*. Piscataway (NJ): IEEE; 2013. p. 1–5.
161. Samanta T, Han JH, Lee HU, Cha BK, Park YM, Viswanath NSM, Cho HB, Kim HW, Cho SB, Im WB. Large-scale mechanochemical synthesis of cesium lanthanide chloride for radioluminescence. *Inorg Chem*. 2024;63(35):16483–16490.
162. Sun H, Yang X, Li P, Bai Y, Meng Q, Zhao H, Wang Q, Wen Z, Huang L, Huang D, et al. Solution synthesis and light-emitting applications of one-dimensional lead-free cerium(III) metal halides. *Nano Lett*. 2024;24(33):10355–10361.
163. Fujimoto Y, Nakauchi D, Yanagida T, Koshimizu M, Asai K. New intrinsic fast scintillator: Cesium praseodymium chloride. *Sens Mater*. 2022;34(2):629–636.
164. Oomen EWJL, Smit WMA, Blasse G. Jahn-Teller effect in the Sb^{3+} emission in zircon-structured phosphates. *Chem Phys Lett*. 1984;112(6):547–550.
165. Guo X-X, Chen J-H, Luo J-B, Wei J-H, Zhang Z-Z, He Z-L, Peng Q-P, Kuang D-B. All-inorganic $Cs_2YbCl_5·H_2O$ perovskite with luminescence response to methanol for anti-counterfeiting. *Adv Opt Mater*. 2024;12(22):2400681.
166. Ma W, Xu D, Zhao L, Xuan T, Wang X, Xie R-J, Wang X. Sb^{3+}-activated 0D Cs_3LuCl_6: A cyan–green phosphor with near-unity quantum yield for ultrahigh-CRI full-spectrum white LEDs. *Adv Opt Mater*. 2025;13(36):Article e03160.
167. Gao R, Xiang J, Ding X, Chen C, Chang J, Chen R, Yang Z, Guo C. Sb-doped Cs_3LuCl_6 nanocrystals for efficient x-ray imaging. *Chin Opt Lett*. 2026;24(2):Article 021601.
168. Chen J, Guo Y, Chen B, Zheng W, Zhang X, Wei X, Cao Y, Suo H, Wang F. Kinetics-tunable hydrochromic luminescence switching in Rb_3TbF_6:Eu^{3+} perovskite. *Adv Opt Mater*. 2024;12(18):2400147.
169. Chen J, Guo Y, Chen B, Zheng W, Wang F. Ultrafast and multicolor luminescence switching in a lanthanide-based hydrochromic perovskite. *J Am Chem Soc*. 2022;144(48):22295–22301.
170. Xiong H, Dong J, Yang J, Liu Y, Song H, Gan S. Facile hydrothermal synthesis and multicolor-tunable luminescence of YPO 4: Ln^{3+}(Ln= Eu, Tb). *RSC Adv*. 2016;6(100):98208–98215.
171. Samanta T, Yadav AN, Han JH, Kim M, Jang SW, Viswanath NSM, Im WB. Cerium-sensitized highly emissive 0D cesium cerium terbium chloride alloy nanocrystals for white light emission. *Adv Opt Mater*. 2024;12(23):2400909.
172. Wang T-C, He Z-L, Luo J-B, Peng Q-P, Wei J-H, Chen K-L, Chen J-H, Guo X-X, Kuang D-B. Organic–inorganic hybrid rare earth halide glasses for tunable multicolor x-ray scintillation. *Angew Chem Int Ed Engl*. 2025;64(23): Article e202504658.
173. Lian L, Xiong D, Fan Y, Liang T, Ai M, Zhang J, Jia M, Liu Y, Ma Z, Chen X, et al. Water-assisted rapid evaporation synthesis of transparent and multicolor luminescent lanthanide-based metal halide glasses for high-resolution x-ray imaging. *Adv Funct Mater*. 2025;Article e23727.
174. Kim HW, Han JH, Ko H, Samanta T, Lee DG, Jeon DW, Kim W, Chung Y-C, Im WB, Cho SB. High-throughput screening on halide perovskite derivatives and rational design of Cs_3LuCl_6. *ACS Energy Lett*. 2023;8(8): 3621–3630.
175. Wang Z, Dujardin C, Freeman MS, Gehring AE, Hunter JF, Lecoq P, Liu W, Melcher CL, Morris CL, Nikl M, et al. Needs, trends, and advances in scintillators for radiographic imaging and tomography. *IEEE Trans Nucl Sci*. 2023;70(7):1244–1280.
176. Pilania G, Liu X-Y, Wang Z. Data-enabled structure–property mappings for lanthanide-activated inorganic scintillators. *J Mater Sci*. 2019;54(11):8361–8380.

177. Belsky A, Ivanovskikh K, A. Vasil'ev, M.-F. Joubert, C. Dujardin. Estimation of the electron thermalization length in ionic materials. *J Phys Chem Lett*. 2013;4(20):3534–3538.
178. Luo J, Wang X, Li S, Liu J, Guo Y, Niu G, Yao L, Fu Y, Gao L, Dong Q, et al. Efficient and stable emission of warm-white light from lead-free halide double perovskites. *Nature*. 2018;563(7732):541–545.
179. Marques MA, Gross EK. Time-dependent density functional theory. *Annu Rev Phys Chem*. 2004;55:427–455.
180. Tully JC. Molecular dynamics with electronic transitions. *J Chem Phys*. 1990;93(2):1061–1071.
181. Feng P-Y, Sun X-L, An Z-H, Deng Y, Wang C-E, Jiang H, Li J-J, Zhang D-L, Li X-Q, Xiong S-L, et al. The energy response of $LaBr_3$(Ce), $LaBr_3$(Ce,Sr), and NaI(Tl) crystals for GECAM. *Nucl Sci Tech*. 2024;35(2):23.
182. Zhao J-Q, Han M-F, Zhao X-J, Ma Y-Y, Jing C-Q, Pan H-M, Li D-Y, Yue C-Y, Lei X-W. Structural dimensionality modulation toward enhanced photoluminescence efficiencies of hybrid lead-free antimony halides. *Adv Opt Mater*. 2021;9(19):2100556.
183. Lin F, Wang H, Liu W, Li J. Zero-dimensional ionic antimony halide inorganic–organic hybrid with strong greenish yellow emission. *J Mater Chem C*. 2020;8(22):7300–7303.
184. Dorenbos P. Light output and energy resolution of Ce^{3+}-doped scintillators. *Nucl Instrum Methods Phys Res A*. 2002;486(1):208–213.
185. Dutta S, Yoo JH, Kwon SB, Dastgeer G, Yoon DH. Harnessing dual violet emission in cerium-based perovskite derivatives for solution-processed next-generation lighting. *ACS Appl Opt Mater*. 2025;3(5):1070–1077.
186. Du H, Yang L, Pang J, Shen Z, Li J, Dong X, Luo Y, Luo J, Tang J. Vacuum-deposited Rb_3CeI_6 for deep-blue-light-emitting diodes. *Opt Lett*. 2023;48(11):2777–2780.
187. Wang T, Zhou D, Wang R, Wang Y, Li W, Liang J, Song H. Breaking efficiency barrier: Dual-channel energy transfer enables record 1540 nm NIR LEDs from Er^{3+}-doped Cs_3DyI_6 nanocrystals. *Adv Mater*. 2026;38(1):Article e12712.
188. Li X, Cui H, Zhong Y, Zhou X, Xu S, Liu S, Wang C. Lead-free Ce-doped perovskite scintillators with high figure of merit. *J Energy Chem*. 2024;99:74–82.
189. Yang Z, Cui J, Gu L, Gao R, Wang T, Song J. Leveraging structural rigidity for thermal robust scintillation in rare-earth halide perovskites. *Adv Powder Mater*. 2026;5(2):Article 100371.
190. Hawrami R, Ariesanti E, Farsoni A, Szydel D, Sabet H. Growth and evaluation of improved CsI:Tl and NaI:Tl scintillators. *Crystals*. 2022;12(11):1517.
191. Taranyuk V, Gektin A, Kisil I, Kolesnikov A. NaI(Tl) and CsI(Tl) scintillation crystal growth by skull method. *J Cryst Growth*. 2011;318(1):820–822.
192. Drozdowski W, Dorenbos P, Bos AJJ, Owens A, Quarati FGA. Gamma ray induced radiation damage in ∅1in×1in $LaBr_3$:5%Ce. *Radiat Meas*. 2008;43(2):497–501.
193. Shah KS, Glodo J, Klugerman M, Moses WW, Derenzo SE, Weber MJ. $LaBr_3$:Ce scintillators for gamma-ray spectroscopy. *IEEE Trans Nucl Sci*. 2003;50(6):2410–2413.
194. Yoshikawa A, Shoji Y, Yokota Y, Kurosawa S, Hayasaka S, Chani VI, Ito T, Kamada K, Ohashi Y, Kochurikhin V. Growth of 2 inch Eu-doped SrI_2 single crystals for scintillator applications. *J Cryst Growth*. 2016;452:73–80.
195. Alekhin MS, Khodyuk IV, de Haas JTM, Dorenbos P. Nonproportional response and energy resolution of pure SrI_2 and SrI_2:5%Eu scintillators. *IEEE Trans Nucl Sci* 2012;59(3):665–670
196. Lecoq P. Development of new scintillators for medical applications. *Nucl Instrum Methods Phys Res, Sect A*. 2016;809:130–139.
197. Xu K, Hu P, Zhang Q, He Q, Liu Q, Wang Y, Huang F, Leng J, Lin X, Shi Y, et al. Effect of annealing on lattice engineering and luminescence in LYSO:Ce scintillators. *CrystEngComm*. 2026.
198. Lee D, Kim M, Woo H-Y, Chae J, Lee D, Jeon S, Oh SJ, Paik T. Heating-up synthesis of cesium bismuth bromide perovskite nanocrystals with tailored composition, morphology, and optical properties. *RSC Adv*. 2020;10(12):7126–7133.
199. Shi L, Li J, Liu Z, Chen P, Jiang Y. Achieving near-unity photoluminescence quantum yield in lead-free cerium(III) halides Cs_3CeX_6 (X = Cl, Br, I) for multifunctional applications. *Adv Opt Mater*. 2026;14(2):Article e01624.